1 OF 2

LEVEL Ⅱ

①

OBSERVATION AND ANALYSIS OF
LiMg AND LiCa EXCIMERS

DISSERTATION

AFIT/DS/PH/80-3   DAVID K. NEUMANN
CAPT   USAF

AFIT/DS/PH/80-3

OBSERVATION AND ANALYSIS

OF LiCa AND LiMg EXCIMERS

DISSERTATION

Presented to the Faculty of the School of Engineering
of the Air Force Institute of Technology
Air University
in Partial Fulfillment of the
Requirements for the Degree of
Doctor of Philosophy

by

David K. Neumann, B.S., M.S.
Capt   USAF
Aug 1981

Approved for public release: distribution unlimited

OBSERVATION AND ANALYSIS

OF LiCa AND LiMg EXCIMERS

by
David K. Neumann, B.S., M.S.
Capt   USAF

Approved:

Donn G. Shankland	9 Nov 1981
Chairman	
David J Benard	4 Aug 81
Allen M. Hunter, II	30 Nov 1981
John Jones Jr.	9 Dec. 1981
Ernest C. Racka	4 Dec 1981
Wm. F. Bailey	9 Dec. 1981

Accepted:

JSPrzeminiecki   9 Dec. 1981

Dean, School of Engineering

Preface

This report summarizes twelve months of experimental effort devoted to the analysis of diatomic molecules consisting of one Column I atom (alkali metals) and one Column II atom (alkaline earth). This study was an integral part of the research efforts of the New Laser Concepts Branch of the Air Force Weapons Laboratory, Kirtland AFB, New Mexico. The Air Force Weapons Laboratory has been interested in these molecules as the optically active medium for potential laser candidates. This research resulted in the first observation and analysis of the LiMg and LiCa molecules.

Several different types of experiments were performed during the course of this work. These included laser induced chemiluminescence experiments for observing the molecules and characterizing their potential energy curves and fluorescence time delay and efficiency measurements for determining reaction rates. Through this experimentation and the study of the associated theory, I have been able to increase my understanding and appreciation of chemical physics research while making an original contribution to science.

I would like to thank my advisor Dr. D. J. Benard of the Air Force Weapons Laboratory for his guidance through the course of this project. I would like to express my appreciation to Dr. S. J. Davis for his advice and the use of his equipment during these efforts and Dr. H. Michels of United Technology Research Center for his timely

Contents

List of Figures

List of Tables

Abstract

Emission from LiCa and LiMg excimers was obtained for the first time upon pumping mixtures of Li and Ca vapors and Li and Mg vapors with an Ar^+ laser. The emission spectra were analyzed spectroscopically and found to be in good agreement with a synthetic spectrum derived from ab initio calculations of the LiMg and LiCa potential energy curves.
A kinetic model was developed to explain the LiMg formation process. The kinetics of production of LiMg* were analyzed by time delay measurements and efficiency measurements of the fluorescence intensity. The LiMg* emission results from the following reactions:

$$Li_2(X) + h\upsilon \ (488 \ nm) \rightarrow Li_2(B)$$

$$Li_2(B) + Mg \rightarrow LiMg* + Li$$

$$LiMg* \rightarrow LiMg + h\upsilon \ (960 \ nm)$$
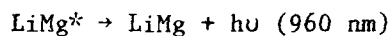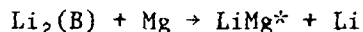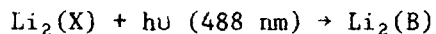
The LiMg formation rate constant for the above reaction was determined to be $2.9 \times 10^{-10} \ cm^3/sec$. Several other rate constants were measured for the Li/Mg system which resulted in an overall specification of the kinetic model.

Chapter I - Introduction

A. Excimers

This thesis reports the first study of the kinetic and spectro-
scopic properties of gas phase LiMg and LiCa diatomic molecules.
These species, composed of an alkali metal(Group IA) atom and an
alkaline earth(Group IIA) atom, are part of a larger class of diatomic
molecules known as excimers. Excimers are characterized by an un-
stable or repulsive molecular ground state as shown in Figure 1.
Thus, an excimer molecule only exists as a stable species in bound
excited states.

The noble gas halides are a class of diatomic molecules observed
to have these characteristics.[1-4] The repulsive nature of the ground
electronic state in these species is a direct result of the closed
shell structure of the noble gas atoms. Excitation of the noble gas
atoms results in an open electronic structure with unpaired electrons.
Consequently, ionic and covalent interactions of the excited noble gas
atoms with halogen atoms can result in bound molecular states.

Other excimer species include the noble gas dimers, noble gas
alkalis and the alkaline earth dimers.[5-7] In the latter case, the
alkaline earth atoms act as psuedo noble gas species since their
ground electronic states consist of a core and two paired s electrons.
Similar considerations apply to molecules such as LiMg which are
composed of an alkali metal and alkaline earth atom. The contribution
to bonding due to ionic interactions is small because the ionic states
are far removed in energy. There is little potential for covalent
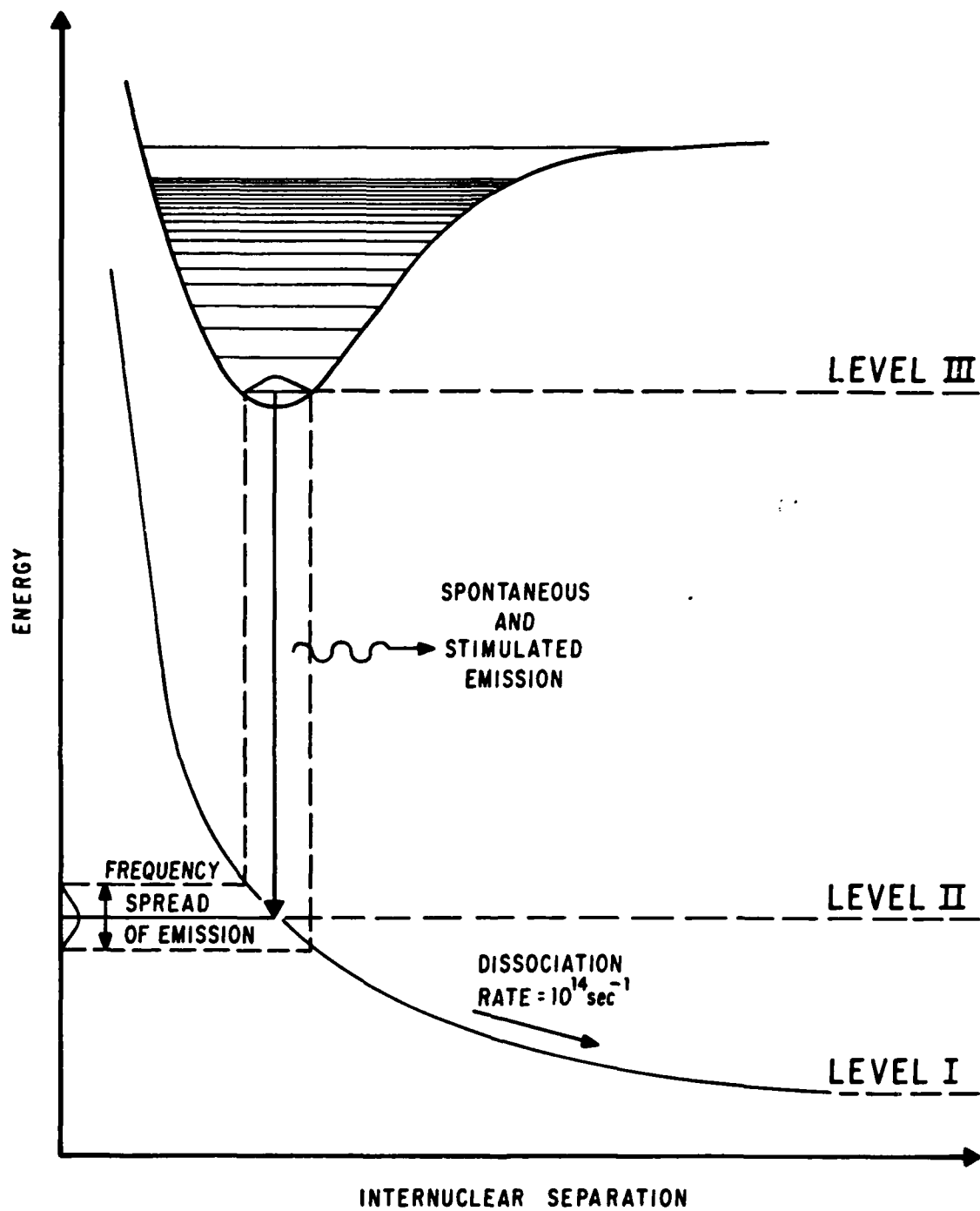
Figure 1 - Potential Energy Curve of Excimer Molecule

bonding due to the closed shell structure of the alkaline earth atom. Therefore, it is expected that LiMg and LiCa in particular will have the repulsive ground states that are characteristic of excimers.

The characteristic emission spectra of excimer molecules are strongly affected by the dissociative nature of the ground state. The bound states of diatomic molecules are characterized by discrete vibrational and rotational energy levels resulting from the quantized motion of the nuclei. In an excimer, transitions from bound excited states terminate in a continuum of energy levels characteristic of the repulsive ground state. Consequently, the emission spectrum of an excimer is continuous as is shown in Figure 1.

Detecting the existence of an excimer requires the use of specialized techniques because of the repulsive ground state. Standard experimental techniques such as absorption or direct optical excitation will work only under conditions where a large portion of the ground state atoms are thermally associated. For most metal vapor excimers this requires very high densities which are experimentally difficult to obtain due to the reactivity of the alkali metals. Additionally in high density regimes, collisional phenomena such as chemical reaction, electronic quenching and energy transfer which compete with the radiative processes may inhibit observation of the excimer. In the experiments conducted for this thesis a laser was used to optically excite an alkali metal dimer molecule maintained at low densities. Following reaction of the excited dimers with alkaline earth atoms radiative decay of the excimer was observed. This process is termed laser induced chemiluminescence.

3

A plot of the reaction symmetries for a generic alkali/ alkaline earth system is shown in Fig. 2. Analysis suggests that laser induced chemiluminescence experiments could produce observable excimer emission since the formation of the excimers via the reaction of excited alkali dimers with alkaline earth atoms is both symmetry allowed and exothermic. Reaction of the alkaline earth atom with the ground state dimers is an endothermic process. However, excitation of the dimer substantially reduces its binding energy and provides the overall energy necessary to make the excimer production reaction energetically feasible. This demonstrates that different states of the same chemical species can have grossly different reactive properties. Thus, each state must be treated as a separate entity in a kinetic analysis. Consequently, the kinetics of even this relatively simple system can become quite complex. The diagram shows that the excimers can also be produced via an alternate mechanism involving the reaction of ground state alkali dimers with metastable alkaline earth atoms. This process, however, will not be examined in this thesis.

The success of a laser induced chemiluminescence experiment not only depends upon the existence of a proper kinetic channel for the excimer formation but also upon the relative rates of the competing processes that consume the excited alkali dimer molecules. These include rapid radiative decay and collisional energy transfer to excited atomic states. Additionally, competition between the radiative decay of the excimer molecule and chemical reactions of the excimer with alkali metal atoms can substantially limit the yield of excimer photons obtained. Consequently, it is necessary to perform the laser induced chemiluminescence experiments in a density regime

4

ENERGY

$A_2(X^1\Sigma) + B(^3P)$

$^1\pi$ $A_2(B^1\pi) + B(^1S)$

$A(^2S) + AB^*(^2\Sigma)$ $^3\pi$

$A(^2S) + AB^*(^2\pi)$

$^1\Sigma$

$^3\pi$ $A_2(A^1\Sigma) + B(^1S)$

$^3\Sigma$ $A_2(a^3\pi) + B(^1S)$

$A(^2S) + AB(^2\Sigma)$

$^1\Sigma$

$A_2(X^3\Sigma) + B(^1S)$

$^3\Sigma$

$^1\Sigma$ $A_2(X^1\Sigma) + B(^1S)$

INTERNUCLEAR DISTANCE
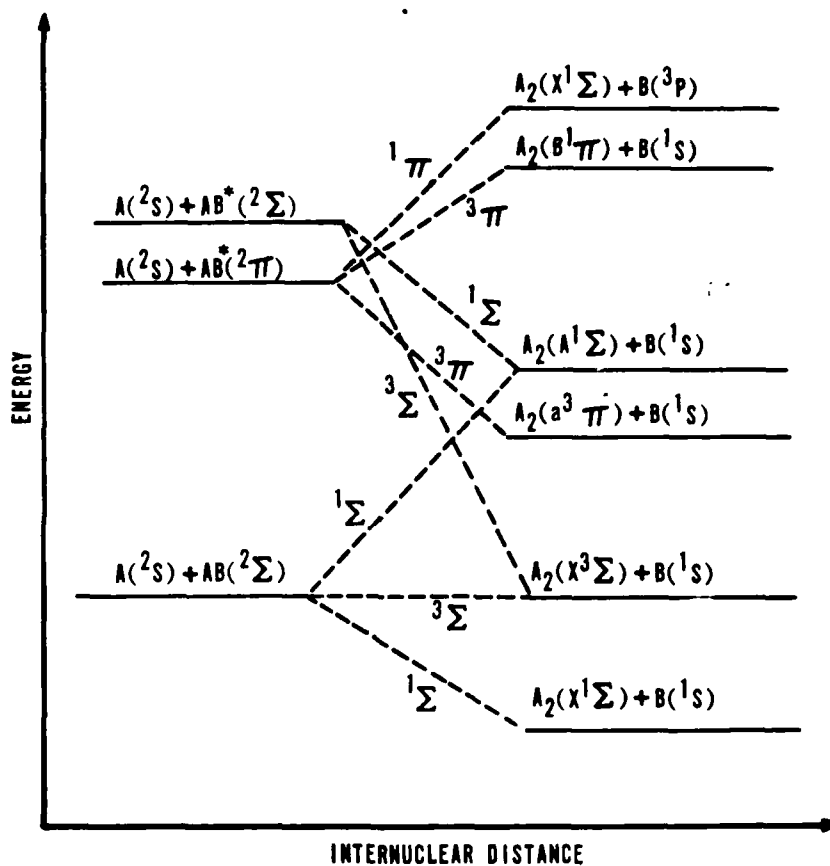
Figure 2   Reaction Symmetries for Group IA/IIA Systems

5

that is favorable to both the chemical formation and radiative decay of the excimers. This requires the coincidence of a high concentration of alkaline earth atoms and low concentration of alkali metal atoms. These requirements tend to be contradictory since the vapor pressure curves for the alkali metals and alkaline earths follow one another. A compromise must be made to achieve optimal excimer emission. Fortunately, Mg and Ca are more volatile than Li so that a reasonable environment for LiMg or LiCa laser induced chemiluminescence can be obtained in a simple heat pipe.

B. Historical Background

The first observation of an alkali metal/alkaline earth diatomic molecule occurred long before the concept of an excimer had been postulated. In 1898, Liveing and Dewar observed diffuse absorption bands in high pressure cells containing Na or K and Mg.[8] In 1925, Barat performed essentially the same experiments in which he reconfirmed the observations of NaMg and KMg and additionally observed RbMg and CsMg.[9] These efforts demonstrated the existence of gas phase diatomic species composed of alkali metal and alkaline earth atoms, but provided no information on their molecular structure. Following this work, there were no efforts concerning IA/IIA diatomics until 1976.

In the mid 1970's, research efforts investigating gas phase chemiluminescent reactions were conducted, with the ultimate goal being the development of a short wavelength chemical laser. Research in this area by Benard and Slafer resulted in the discovery of a chemical chain reaction that efficiently produced alkaline earth atoms in a metastable electronically excited state.[10] Additional

experiments were performed to determine if the energy stored in the alkaline earth atoms could successfully be transferred to a lasing species. During this work, Mg metastables were reacted with K_2 dimers in a low pressure flow tube. Chemiluminescence was observed which was attributed to the KMg excimer.[11] Subsequent experiments involving optical excitation of K_2 in a static cell containing low pressures of K and Mg again resulted in observation of KMg emission.[12] Later, in unpublished work at the Air Force Weapons Laboratory, the excimer NaMg was observed in an analogous manner. A variation of this experiment in which K was added to the Na and Mg demonstrated enhanced NaMg emission. Using a tunable dye laser NaMg emission intensity versus laser wavelength was recorded. The intensity profile matched the predicted absorption profile for the $NaK(X^1\Sigma \rightarrow C^1\Pi)$ transition. The result established that the excimer emission resulted from chemilumi- nescence in which optically excited $NaK(C^1\Pi)$ was the reactive pre- cursor. Therefore, the emitting species was not directly pumped by the laser. This experiment originated the phenomena of laser induced chemiluminescence.

These experiments demonstrated that alkali metal/alkaline earth excimers could be observed in emission at low pressure. However, the results of these experiments were qualitative in nature. The emitting species and precursor had been identified, but no detailed investiga- tion of the spectroscopy or kinetics had been conducted.

C. Applications

The IA/IIA excimers observed by Benard were considered as chem- ically pumped excimer laser candidates. The potential for such a laser was limited in the case of NaMg and KMg by the coincidence of

the excimer emisssion bands and their respective alkali dimer(Na_2 and K_2) absorption bands. Two additional factors prevented an evaluation of their laser potential: kinetics data was not available to assess the excimer formation or loss rates, and the scalability of a source of metastable alkaline earth atoms had not been demonstrated. If a new alkali metal/alkaline earth excimer could be discovered, which did not have the dimer absorption problem, and if the formation and loss rates could be measured, then this species could be considered for possible use in a laser system. At the very least, it might have potential as an optically excited excimer laser.

D.   Research Objectives

The research objectives for this thesis were:

(a) to investigate a new alkali metal/alkaline earth excimer using the technique of laser induced chemiluminescence

(b) to characterize the molecular properties of the observed emitter using available experimental and theoretical information

(c) to determine the kinetic processes and rates important in the production and decay of the excimer.

E.   Accomplishments

Initially, various alkali metal, alkaline earth combinations were evaluated using the laser induced chemiluminescence technique. The combinations of Li and Mg and Li and Ca resulted in the observation of new emissions in the 900-1100 nm region which were attributed to the respective excimers, LiMg and LiCa. The emission spectra of the molecules were recorded, analyzed and compared to the results of ab initio calculations completed by H. Michels at the United Technology Research

Center. Using the results of the emission experiments and theoretical considerations, a kinetic model for the LiMg system was postulated. Experiments were then conducted to investigate the kinetics of the LiMg system. Modulation was imposed on the kinetic system by electro-optically chopping the laser excitation source. Time delays between modulated signals from various emitters were measured and related to kinetic rates. Additionally, the efficiency of light production was measured. The results of these experiments were then used to quantitatively determine kinetic rates for the postulated model.

A total of ten reaction rate constants and three radiative lifetimes were calculated, measured or had upper bounds established as a result of the kinetics work. The kinetics work together with the analysis of emission from two new excimers constituted the thesis work.

A. Introduction

This thesis reports the first observation of the diatomic species LiMg and LiCa. Although absorptions in several alkali-Mg diatomics were seen before no alkali-Ca diatomic had ever been observed. The work presented in this chapter represents the first attempt to characterize LiMg and LiCa excimers. Experimental evidence of the existence of these species is provided. A qualitative analysis of the electronic structure of LiMg and LiCa is presented. The results of molecular ab initio calculations including the potential energy curves and predicted emission spectra for LiMg and LiCa are explained and related to the experimental work. The theoretical calculations are the unpublished work of Dr H. Michels of UTRC.

B. Theory

1. Molecular State Characterization

The characteristics of the ground state and first few excited states of LiMg and LiCa can be qualitatively predicted from knowledge of the electronic structure of the separated atoms. A ground state Li atom (^{2}S) has a single s electron in its outer valence shell while the ground state alkaline earth atoms (^{1}S) have two paired s electrons. The first excited state of the Li atom (^{2}P) results from the promotion of the s electron to a p orbital (p_x, p_y, p_z). The first excited state of the alkaline earth atoms (^{3}P) also results from promotion of an s electron to a p orbital. The Li(^{2}P) state is connected to the ground state by a highly allowed electric dipole transition. The Ca(^{3}P) and Mg(^{3}P) states lie higher in energy than the Li(^{2}P) state and transitions to their respective ground states are

10

spin forbidden. An energy level diagram for Li, Ca, and Mg is shown in Figure 3a. The molecular states correlating to these separated atom limits have been derived from symmetry principles[13-16] and are shown for LiMg in Figure 3b. Since the energy ordering of the separated atom limits are the same for both LiMg and LiCa, the following discussion applies to LiCa as well.

$$
\begin{array}{ll}
& \underline{Mg(^3P)} \\
20 \\
& \underline{Ca(^3P)} \quad \underline{Li(^2P)} \\
\text{Energy} \quad 10 \\
(1/cm \times 10^3) \\
0 \quad\quad Ca(^1S) \quad Li(^2S) \quad Mg(^1S)
\end{array}
$$
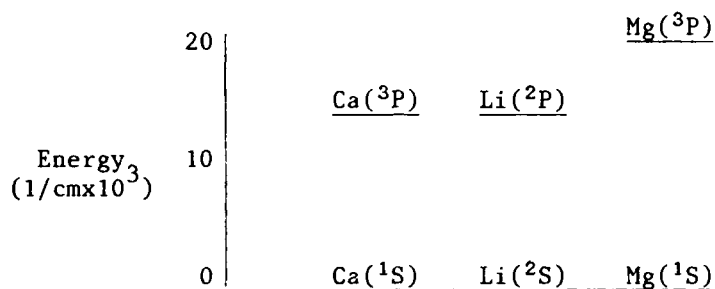
Figure 3a - Li, Ca, and Mg Atomic Energy Levels

Atomic States	Molecular States

$$
\begin{array}{ll}
& F^4\Sigma \\
& E^4\Pi \\
Li(^2S)+Mg(^3P) & \\
& D^2\Sigma \\
& C^2\Pi \\
Li(^2P)+Mg(^1S) & B^2\Sigma \\
& A^2\Pi \\
Li(^2S)+Mg(^1S) & X^2\Sigma
\end{array}
$$
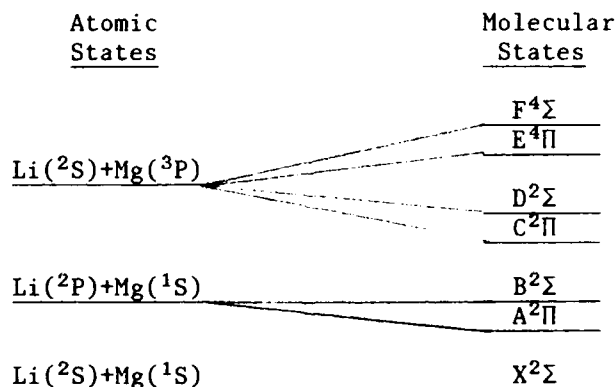
Figure 3b - LiMg Correlation Diagram

LiMg has a single $^2\Sigma$ ground electronic state correlating to the Li(^2S) and Mg(^1S) separated atom limits. The first manifold of excited states are of $^2\Sigma$ and $^2\Pi$ symmetry and correlate to ground state

11

$Mg(^1S)$ and excited $Li(^2P)$ atoms. A manifold of four electronic states of symmetry $^4\Sigma$, $^4\Pi$, $^2\Sigma$ and $^2\Pi$ correlate to excited $Mg(^3P)$ and ground state $Li(^2S)$ atoms.

Some aspects of the molecular bonding in these electronic states can be predicted from consideration of the atomic configurations and the resulting interatomic forces. The $^2\Sigma$ ground state is expected to be predominantly dissociative in character due to short range repulsive valence forces. These forces which consist of both coulombic(charge) and exchange(Pauli Principle) contributions, result from the interaction of the outer s electron of the Li atom with the paired s electrons of the Mg atom. At longer internuclear distances, it is expected that the repulsive forces will be dominated by weak attractive dispersion forces resulting in a small potential minimum. Dispersion forces result from interactions of induced multipole moments of the atoms and usually are dominated by the induced dipole-induced dipole interaction which is more commonly called the Van der Waals force.[17] Since the induced dipole moment is directly proportional to the polarizability of the atoms, it is expected that the larger polarizability of Ca[18] will result in a more strongly bound ground state for LiCa than for LiMg.

As in the case of LiHe and NaHe[19,42] the bonding in the first set of excited states can be directly related to the three possible orientations(p_z or p_x, p_y) of the excited Li p orbital. With the electron in a p_z orbital, aligned to the internuclear axis of the diatomic molecule and interacting with the paired outer s electrons of the alkaline earth atom, the repulsive forces should be even stronger than for the ground state LiCa and LiMg interactions. The resulting $^2\Sigma$

state should be strongly repulsive. The $^2\Pi$ state should be bound due to attractive dispersion forces (ion-induced dipole) between the unscreened Li+ core resulting from the p_x or p_y configuration of the outer electron and the Mg outer s electrons.

The set of excited $^2\Sigma$ and $^2\Pi$ states correlating to Mg(^3P) and Li(^2S) should be strongly bound due to attractive valence forces resulting from interactions of the unpaired Mg electrons with the single Li s electron. As discussed for the previous set of $^2\Sigma$ and $^2\Pi$ states, the $^2\Pi$ state should be more strongly bound due to the additional attractive ion-induced dipole dispersion forces.

The quartet states in this manifold should be strongly repulsive due to large repulsive exchange forces resulting from the interaction of spin aligned electrons.

The bonding exhibited by the excited electronic states of LiMg and LiCa is not only affected by forces resulting from the atom-atom interactions, but by the perturbation of one state by another of like symmetry. The upper set of LiMg and LiCa $^2\Pi$ and $^2\Sigma$ states are expected to be strongly bound while the lower set is primarily repulsive. This normally would result in crossings of the potential energy curves. However, the potential energy curves of states of the same symmetry cannot cross in the adiabatic limit but tend to repel one another.[20,21] The net effect for LiMg and LiCa should be strongly bound lower $^2\Pi$ and $^2\Sigma$ states and repulsive upper $^2\Pi$ and $^2\Sigma$. The effect of the interaction should be more pronounced in LiCa because of the closer resonance of the Li(^2P) and Ca(^3P) states which should result in stronger mixing of the wavefunctions.

13

Based on this analysis, these states can now be given the standard spectroscopic notation according to their energy ordering. The ground state will be labeled $X^2\Sigma$, the first two excited states will be labeled $A^2\Pi$ and $B^2\Sigma$ and the next two states $C^2\Pi$ and $D^2\Sigma$.

The repulsion of the $^2\Pi$ and $^2\Sigma$ states should significantly affect the observed transitions in LiMg and LiCa. The lower set of states are stable enough to support substantial concentrations of molecules given an appropriate chemical production mechanism. The upper set of states should be repulsive and therefore will not support any concentrations. Observed emissions in LiMg and LiCa should therefore result from allowed transitions between the lower $^2\Pi$ and $^2\Sigma$ states and the ground state.

A quantitative determination of the electronic structure of LiMg and LiCa has been obtained by means of ab initio calculations of the potential energy curves.[24] These calculations were completed by H. Michels of United Technology Research Center as part of a cooperative effort to obtain both a theoretical and experimental understanding of these excimers. The calculational procedure that was utilized was the valence configuration interaction (VCI) method.[22] For these calculations a spin free nonrelativistic Hamiltonian was employed in the Born-Oppenheimer approximation. Symmetry compatible electronic wavefunctions, composed of linear combinations of atomic orbitals and depending on the nuclear coordinates were made to be optimum approximations to solutions of the Schrodinger equation by involving the variational principle.[23]

A full VCI expansion was chosen for the LiCa studies using an optimized minimum basis: Li(1s), Ca(1s, 2s, 2p) for the core

14

electrons and a double zeta optimized basis: Li(2s,2s̄, 2p,2p̄),
Ca(3s, 3s̄, 3p, 3p̄) for the valence shell description. This basis
yielded a ^{2}S-^{2}P Li excitation energy of 14830/cm (14904/cm = experimental value) and a ^{1}S-^{3}P Ca excitation energy of 15135/cm (15225/cm =
experimental value), thus insuring a proper long-range mixing of the
wavefunctions connecting to Li*(^{2}P)+Ca(^{1}S) and Li(^{2}S)+Ca*(^{3}P).[24] A
similar basis set was used for the LiMg studies with similar results.

The calculated potential energy curves for LiCa and LiMg[27] are
shown in Figures 4 and 5. As predicted, qualitatively the ground
states of both molecules exhibit small van der Waals potentials. The
LiCa ground state is more strongly bound (580/cm) than the LiMg ground
state (137/cm). The A^{2}Π and B^{2}Σ states are more strongly bound than
the C and D states. The coefficients of the wavefunction expansions
showed that the excited electronic states of both molecules were
strongly mixed even at relatively large internuclear separation. At
shorter internuclear separation, the A^{2}Π and B^{2}Σ states assumed more
of the character of the alkaline earth (^{3}P) and Li(^{2}P) states
respectively. The changing characters of the electronic states
with internuclear separation strongly affects their transition
probabilities to the ground state because of the different Li(^{2}P-^{2}S)
and Ca(^{3}P-^{1}S) transition probabilities. The magnitude of this effect
will be determined in the next section. Calculations of the quartet
states were not performed since they do not optically connect to the
ground state and do not interact with the doublet states.

The spectroscopic constants for the ground state, A and B
states of LiMg and LiCa[27] are shown in Tables 1 and 2. The energy levels

15
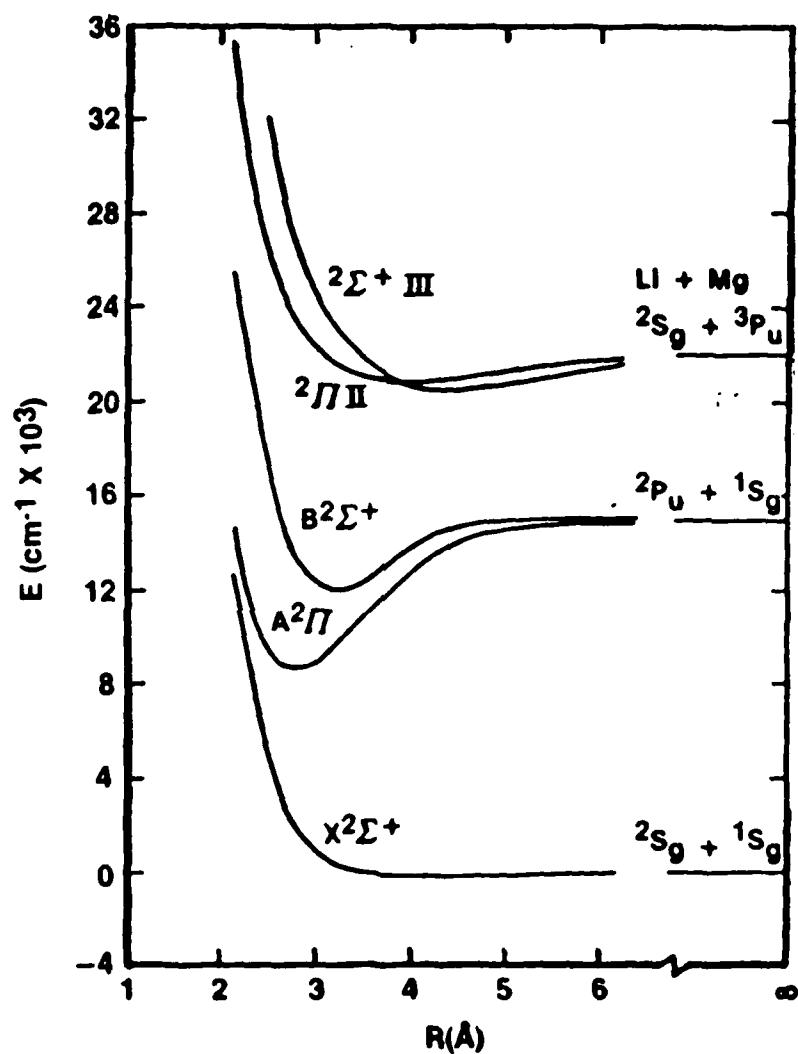
Figure 4 - Potential Energy Curves for LiMg
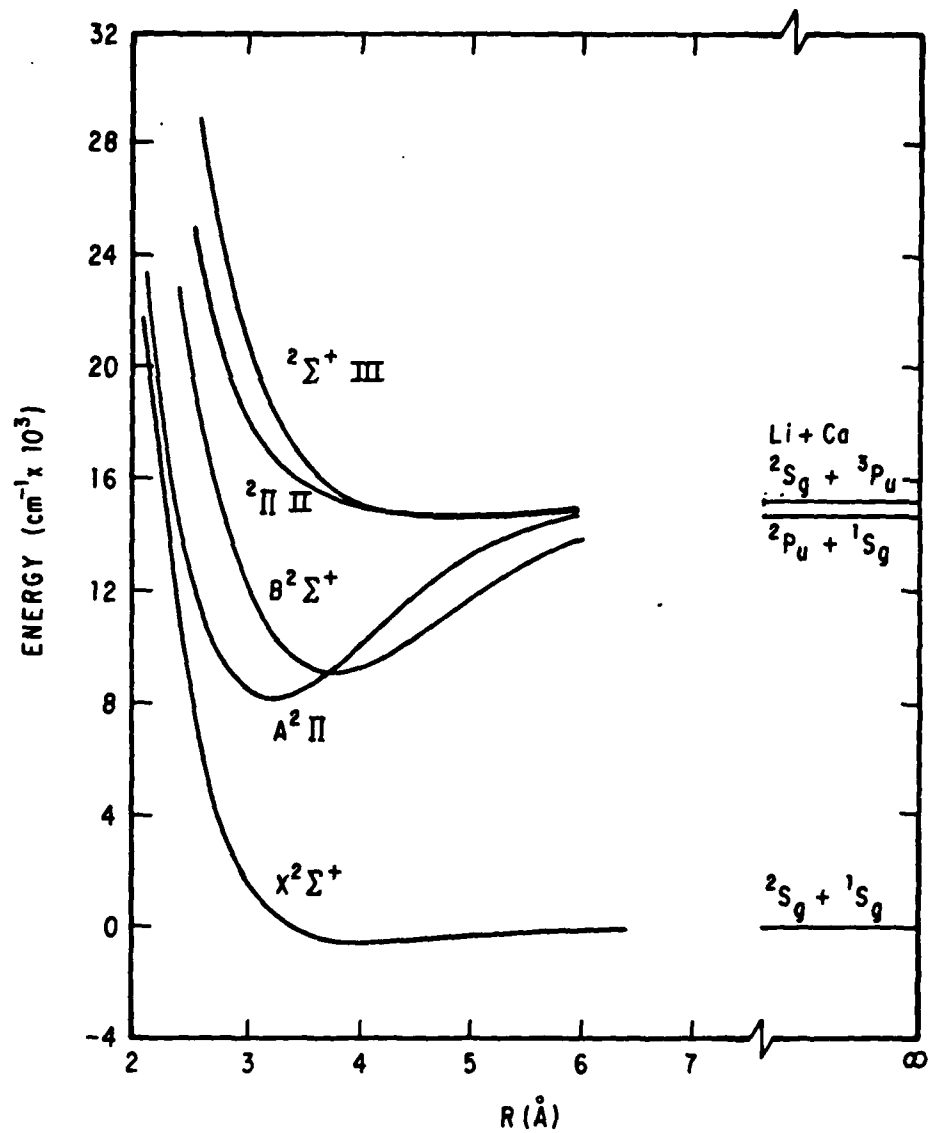
Figure 5 - Potential Energy Curves for LiCa

Table I - LiCa Calculated Spectroscopic Constants

Spectroscopic	State		
Constant	$X^2\Sigma$	$A^2\Pi$	$B^2\Sigma$
T_e(ev)	0.0000	1.0800	1.1700
ω_e(cm^{-1})	93.3600	252.4400	197.4400
$\omega_e X_e$(cm^{-1})	7.3200	1.2900	.9600
α_e(cm^{-1})	.0119	.0019	.0009
B_e(cm^{-1})	.1890	.2740	.1950
r_e(A)	3.8830	3.2260	3.8220
D_e(eV)	.0720	.8820	.7650
D_0(eV)	.0670	.8660	.7520

Table II - LiMg Calculated Spectroscopic Constants

Spectroscopic Constant	State		
	$X^2\Sigma$	$A^2\Pi$	$B^2\Sigma$
T_e (ev)	0.0000	1.1200	1.5619
ω_e (cm^{-1})	65.7000	302.5000	328.2000
$\omega_e\chi_e$ (cm^{-1})	6.9000	2.0000	8.7000
α_e (cm^{-1})	.0160	.0032	.0040
B_e (cm^{-1})	.2024	.4010	.2770
r_e (A)	3.9280	2.7900	3.3560
D_e (eV)	.0167	.7630	.3000
D_0 (eV)	.0073	.7450	.2800

of each state are described by the Dunham expression:

$$E(e,v,J) = T_e + \omega_e(v+\tfrac{1}{2}) + \omega_e\chi_e(v+\tfrac{1}{2})^2 + \cdots$$
$$B_e J(J+1) - \alpha_e(v+\tfrac{1}{2})(J(J+1))$$

where T_e is the electronic energy, ω_e is the vibrational spacing, $\omega_e\chi_e$ is the anharmonic correction, B_e is the rotational constant and α_e is the vibrational and rotational coupling constant. The remaining terms in Tables 1 and 2 are r_e the internuclear separation where the potential energy curve reaches a minimum and D_e and D_o the dissociation energies of the state measured from the bottom of the potential well and first vibrational level respectively.

2. Electronic Transitions in LiMg and LiCa

Radiative transitions between the excited $^2\Pi$ and $^2\Sigma$ states and the $^2\Sigma$ ground state of LiMg and LiCa are electric dipole allowed transitions.[29] The transitions in LiMg and LiCa are expected to be both bound-bound and bound-continuum, based on application of the Franck-Condon principle to Figures 4 and 5. Electric dipole transitions in bound-continuum systems have been analyzed by Mies[30] and have been calculated for LiMg and LiCa by Michels.[31] The bound and continuum spectra are characterized by matrix elements for the transitions where the vibrational wavefunctions are obtained by numerical solution of the Schrodinger equation using the Numerov method[32,33] and the continuum wavefunctions are obtained using the method of Allison and Dalgarno.[34] In both cases the dipole moment function which varies with internuclear distance is required to calculate the matrix elements. The dipole moment function is calculated from the molecular wavefunctions and dipole moment operator for the transition. These

20

calculated dipole moment functions for the $A^2\Pi$, $B^2\Sigma$, $C^2\Pi$ and $D^2\Sigma$ to $X^2\Sigma$ transitions for both LiMg and LiCa are shown in Figures 6 and 7. At shorter internuclear distances the $^2\Sigma$-$^2\Sigma$ transitions have stronger transition moments because the excited state $^2\Sigma$ molecular wavefunction is dominated by the Li(^{2}P) atomic orbital. The Li(^{2}P-^{2}S) transition has a large transition probability (A=10^8/sec). The $^2\Pi$ states are dominated by the character of ^{3}P states of the alkaline earth atoms resulting in a smaller dipole moment function. The alkaline earth (^{3}P-^{1}S) transition probabilities are small (A=10^4/sec). At large internuclear separation, the dipole moment functions are more strongly affected by the wavefunctions associated with the separated atom limits. The $A^2\Pi$ and $B^2\Sigma$ states have larger transition moments which result from the dominance of the Li(^{2}P) character of the wavefunction while the $C^2\Pi$ and $D^2\Sigma$ tend to the alkaline earth ^{3}P limit with resulting smaller transition probabilities. In all cases the $^2\Pi$ states retain more of the ^{3}P character resulting in smaller overall dipole moment functions for the $^2\Pi$-$^2\Sigma$ transitions than for the corresponding $^2\Sigma$-$^2\Sigma$ transitions.

The dipole moment functions shown in Figures 6 and 7 were used to evaluate bound-continuum and bound-bound matrix elements and to predict the emission spectrum resulting from $A^2\Pi$-$X^2\Sigma$ and $B^2\Sigma$-$X^2\Sigma$ transitions.[27] The results are shown in Tables 3 through 10. The bound-contiuum emission tables for LiCa(III,IV) and for LiMg(VII,VIII) show the center wavelengths of various peaks in the emission spectrum resulting from transitions from upper state vibrational levels to the continuum of the ground state. Since each level(v) has a wavefunction with v+1 nodes, the reflection of these nodes into the continuum

21
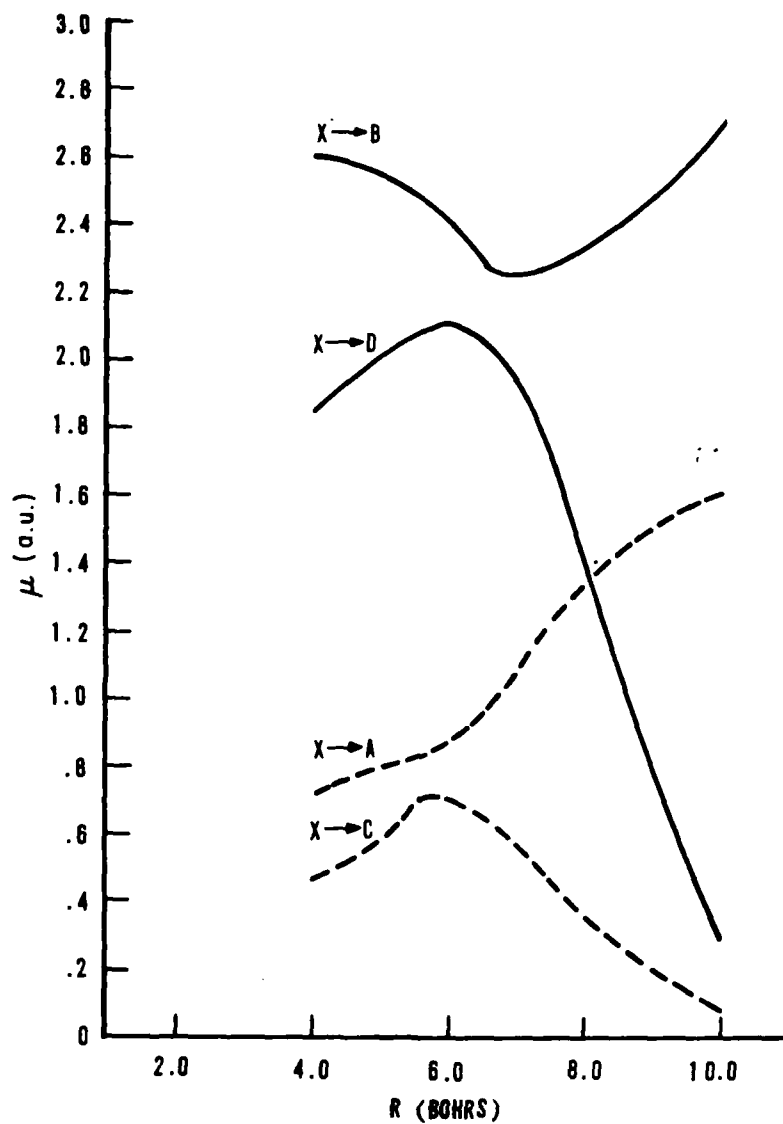
Figure 6 - Dipole Transition Moments for LiMg
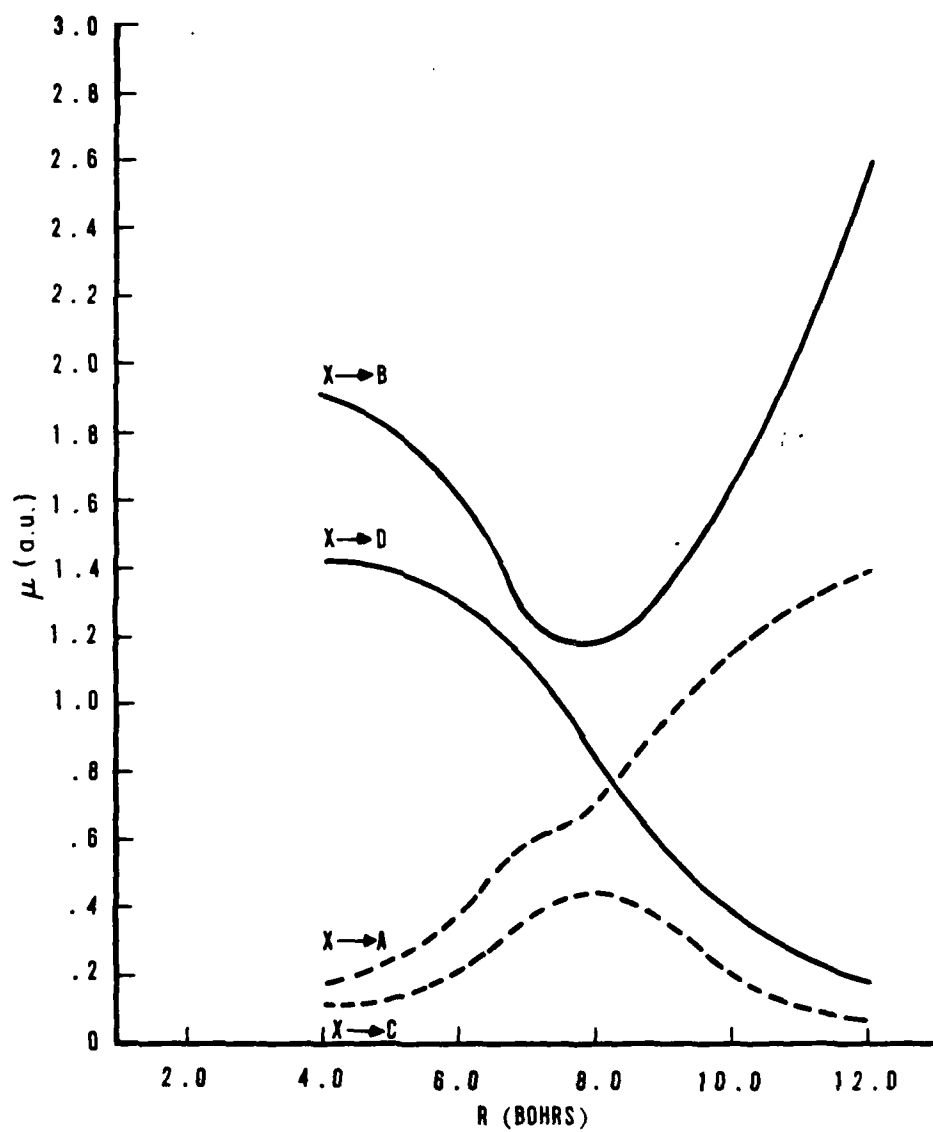
Figure 7 - Dipole Transition Moments for LiCa

result in the multiple peaks shown. Not all of the peaks for all the transitions are shown since the transition moments become negligible with increasing wavelength.

The bound-continuum tables also list the relative amplitudes of the transitions. In both LiMg and LiCa the B-X transitions have the largest vibrational transition amplitudes. This is due to the larger transition moments for the Σ-Σ transitions and the fact that the B state r_e are larger than the A state resulting in transitions to flatter portions of the continuum curve. For the case of LiCa, it is apparent that most of the bound-free emission should be localized in the region of 1010-1020 nm and should result from $v' = 3,4,5$ of the B state. In LiMg the major contributions to the bound-free spectrum should originate from the B state; $v' = 0,1,2,3,4,5$, and should appear in the region of 720-820nm.

The bound-bound emission tables for LiCa(V,VI) and LiMg(IX,X) show that the strongest emissions are the Σ-Σ emission. Again this can be attributed to both the stronger transition moments and the location of the potential wells. In LiCa however higher vibrational levels of the A state (v'=3,etc) have nonnegligible transition amplitudes. Overall the largest transition amplitudes in LiCa result from v'=3 in the $A^2\Pi$ states and v'=0, 1 in the $B^2\Sigma$ state. In LiMg the major contributions to the bound bound spectrum should originate from the $B^2\Sigma$ state and should appear in the region of 690-750.

The emission spectrum resulting from the $C^2\Pi$ and $D^2\Sigma$ states of LiMg and LiCa to the $X^2\Sigma$ ground state were not discussed because these states are primarily repulsive and, therefore, would support only a very small steady state density of molecules. Additionally, these

24

Table III - LiCa($A^2\Pi$-$X^2\Sigma$) Bound-Free Emission Spectrum

Upper State Vibrational Level	Center Wavelength(nm)	Relative Amplitude
v'=0	1237.5	.010
1	1178.5	.012
	1343.2	.003
2	1145.0	.001
	1205.0	.007
	1394.9	.002
3	1113.7	.006
	1133.0	.012
	1234.5	.004
	1434.5	.001
4	1084.5	.017
	1154.0	.008
	1266.0	.003
	1486.0	.000
5	1056.9	.005
	1093.3	.013
	1170.7	.006
	1286.1	.002
6	1047.7	.021
	1103.7	.010
	1182.6	.005
	1300.5	.002

Table IV - LiCa($B^2\Sigma$-$X^2\Sigma$) Bound-Free Emission Spectrum

Upper State Vibrational Level	Center Wavelength(nm)	Relative Amplitude
v'= 0	1091.4	.000
1	1069.1	.017
	1106.3	.000
2	1055.9	.045
	1102.8	.001
	1154.2	.000
3	1027.6	.351
	1052.9	.059
	1099.6	.001
	1150.6	.000
4	1008.2	.907
	1012.3	1.00
	1050.1	.075
	1096.5	.075
	1152.6	.002
5	1009.0	.907
	1047.4	.088
	1093.6	.003
	1149.3	.000
	1211.1	.000

Table V - LiCa ($B^2\Sigma$-$X^2\Sigma$) Bound-Bound Emission Spectrum
λ(nm); Relative Intensity(Energy/sec)

v' v''	0	1	2	3	4	5	6	7
0	1047.2 1.00	1026.3 .154	1006.4 .172	987.5 .071	969.4 .049	952.2 .025	935.7 .014	920.0 .008
1	1053.2 .529	1032.1 .075	1012.0 .035	992.8 .140	974.6 .122	957.2 .128	940.5 .101	924.6 .079
2	1059.3 .183	1037.9 .452	1017.6 .050	998.2 .078	979.8 .002	962.2 .003	945.4 .029	929.3 .055
3	1065.7 .029	1044.1 .589	1023.5 .013	1004.0 .002	985.3 .091	967.5 .068	950.5 .058	934.3 .019

Table VI - LiCa($A^2\Pi$-$X^2\Sigma$) Bound-Bound Emission Spectrum
λ(nm); Relative Intensity(Energy/sec)

v' v''	0	1	2	3	4	5	6	7
0	1139.0 .005	1107.4 .035	1077.9 .124	1050.1 .295	1024.0 .527	999.5 .761	976.3 .932	954.4 1.00
1	1149.0 .011	1116.8 .064	1086.8 .184	1058.6 .329	1032.1 .404	1007.2 .346	983.6 .189	961.4 .041
2	1157.7 .018	1125.1 .095	1094.6 .219	1066.0 .289	1039.2 .220	1013.9 .072	990.0 .000	967.6 .095
3	1166.2 .029	1133.1 .126	1102.2 .229	1073.2 .207	1046.0 .070	1020.4 .001	996.3 .110	973.5 .288

Table VII - LiMg($A^2\Pi$-$X^2\Sigma$) Bound-Free Emission Spectrum

Upper State Vibrational Level		Center Wavelength(nm)	Relative Amplitude
v'=	0	1338.2	.006
	1	1211.3	.010
		1505.5	.002
	2	1127.3	.016
		1291.7	.004
		1610.6	.010
	3	1082.5	.024
		1186.1	.007
		1354.6	.002
		1686.2	.001
	4	1024.6	.034
		1107.0	.010
		1215.5	.004
		1393.0	.002
	5	988.7	.047
		1047.1	.016
		1133.3	.007
		1247.3	.003
	6	955.7	.062
		1002.1	.022
		1062.2	.011
		1151.0	.006
	7	925.4	.075
		968.8	.031
		1016.4	.016
		1159.0	.009

Table VIII - LiMg($B^2\Sigma$-$X^2\Pi$) Bound-Free Emission Spectrum

Upper State Vibrational Level	Center Wavelength(nm)	Relative Amplitude
v'= 0	802.2	.828
1	783.4	.966
	841.8	.552
2	757.3	1.00
	771.4	.448
	811.8	.310
3	745.0	.638
	754.0	.552
	787.5	.310
	813.3	241
4	726.1	.706
	748.0	.310
	766.5	.276
	786.0	.241
	811.7	.207
5	714.5	.793
	763.8	.259
	783.0	.224
	808.5	.207
	847.2	.397

Table IX - LiMg($A^2\Pi$-$X^2\Sigma$) Bound-Bound Emission Spectrum
λ(nm); Relative Intensity(Energy/sec)

v'	0	1	2	3	4
0	1111.0	1075.4	1042.5	1011.9	983.6
	.000	.000	.000	.000	.000
1	1117.1	1081.2	1047.9	1017.0	988.4
	.000	.000	.000	.000	.001
2	1121.9	1085.6	1052.0	1020.9	992.1
	.000	.000	.000	.000	.001

v'	5	6	7	8	9
0	957.2	932.6	909.7	888.3	868.1
	.001	.004	.013	.032	.072
1	961.7	936.9	913.9	892.3	871.9
	.003	.009	.023	.052	.099
2	965.2	940.7	917.0	895.2	874.8
	.003	.008	.020	.040	.068

Table X - LiMg($B^2\Sigma$-$X^2\Sigma$) Bound-Bound Emission Spectrum
λ(nm); Relative Intensity(Energy/sec)

v'	0	1	2	3	4
0	795.8	780.5	766.3	753.2	741.3
	.004	.024	.088	.228	.443
1	799.0	783.5	769.2	756.1	744.0
	.008	.042	.124	.240	.306

v'	5	6	7	8	9
0	730.3	720.3	711.2	702.9	695.6
	.669	.807	.791	.634	.408
1	732.9	722.9	713.7	705.4	698.0
	.235	.069	.007	.224	.665

states are not accessible in the experiments conducted in this thesis due to energy considerations which will be explained in the discussion of the experimental results.

Finally there was no attempt to incorporate the effects of temperature and state dependent chemical production rates into the calculations. The calculations show the transition amplitudes derived from quantum mechanical considerations. To relate these transition amplitudes to real intensities it is necessary to consider how an ensemble of molecules is distributed among all the possible energy levels as a result of collisional effects. These considerations will be included in the comparison of the experimental data to the theory.

C. Experimental Considerations.

1. Heatpipe Operation

The spectroscopic experiments performed for recording emission spectra from LiMg and LiCa required metal atom densities of approximately $10^{16}/cm^3$. This required heating the metals to temperatures of 600-1000°C.[35] In 1969, Vidal and Cooper developed a device called a heatpipe oven for use in spectroscopic experiments,[36] which had the capability to maintain uniform densities of reactive metal vapors over long periods of time. Figure 8 shows the design of the heatpipe, which consists of a straight pipe sealed at both ends with windows containing ports for access to a vacuum pump and inert gas supply. Cooling chambers are located at each end and a heater coil is wrapped around the central region to heat the metal contained inside. Inside the heated region, internal to the pipe, is a wire mesh material which serves to reflux condensed metal vapor back to the hot interior. When the device is operated, it is first filled with an inert gas and the metal to be vaporized. When heated, the metal melts, wets the wire mesh wick and then evaporates. The vapor diffuses toward both ends until it reaches a cooler region where it condenses. The condensed metal flows toward the center heated portion of the pipe as a result of capillary action on the wick. When sufficient heat is added to achieve a temperature such that the metal vapor pressure equals the pressure of the inert gas previously introduced into the cell, the cycling of the metal sets up a region at the center of the heatpipe where only the metal vapor exists at a vapor pressure equal to the inert gas pressure.
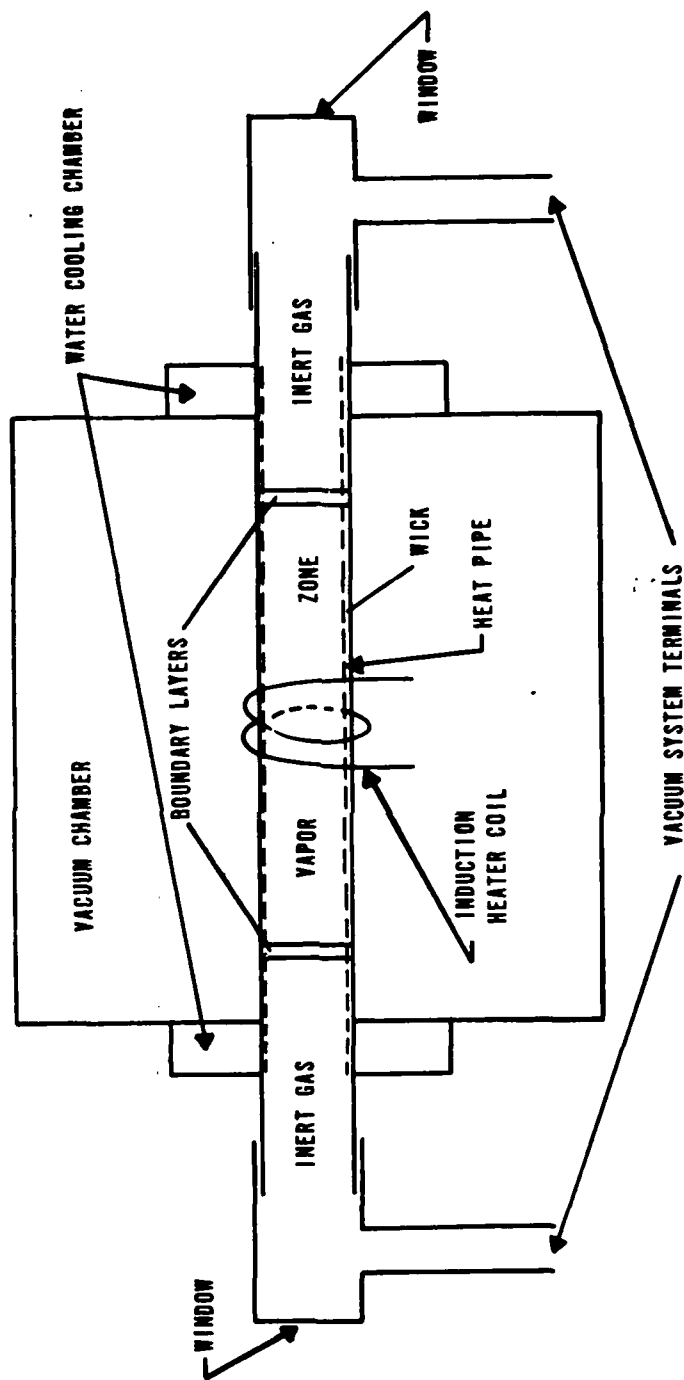
Figure 8 - Straight Heatpipe

Well defined regions or zone boundaries are observed between the metal vapor and the inert gas. With Li in the heatpipe, experiments have demonstrated that the temperature is uniform within the heated region to within 1°C.[36] When two metals having different vapor pressure curves are introduced into the heatpipe, a second set of zone boundaries are formed. The central region of the heatpipe contains a mixture of both metals, with the higher vapor pressure metal confining the lower vapor pressure metal. The second region contains only the higher vapor pressure metal which is confined by the inert gas.[37]

When both metals used are Group I metals which readily wet the wick and flow back to the center of the heatpipe, a situation such as that described above can be maintained. Wicking of Group II metals is much more difficult to obtain and in many cases, the heatpipe must be operated with the buffer gas pressure in excess of the metal pressure to better confine the metal. In this case, no well defined zone boundaries are formed and no pure metal regions are formed. The inert gas pressure in the metal region is just the difference between the inert gas pressure measured in the cold region and the metal pressure defined by the temperature. Even with these changes, the same processes of evaporation, condensation, and flow continue.

Another physical parameter that must be considered in the operation of a two metal heatpipe is the solubility of one metal in another. If one metal is completely soluble in another, the vapor pressure of the solution is reduced by the molar ratio of the two metals (Raoult's Law).[38] This result holds for dilute two component solutions. Deviation from the dilute solution situation requires experimental verification that metal vapor pressures have not been

34

perturbed. However, the lower the solubility of the two metals in each other, the smaller should be the effect on the vapor pressures. The solubility of Group II metals in Group I metals is known to be 2% or less[39-41] which should result in small deviations to the vapor pressure curves.

2. Apparatus

The mixed metal heatpipe used in the experiments for this thesis was modified from the design of Cooper and Vidal to accommodate optical excitation of the metals and observation of the resulting emission. The heatpipe was formed in the shape of a cross as shown in Figures 9 and 10. This allowed a laser beam to be passed through in one direction and the resulting fluorescence to be viewed from the side. The design was slightly modified from one developed by D. J. Benard to achieve 1000°C operation. The modification involved removal of all brass and copper parts since their melting points were being exceeded. The heatpipe was fashioned from a solid stainless steel cylinder, 4" in diameter and 6" high. The cylinder was bored to form a central chamber and to accept four lateral sidearms and one vertical arm, as well as four 1 KW cartridge heater. Water cooling coils were soldered onto each of the sidearms and connected in series. The sidearms were closed at the end by pyrex windows. The vertical arm was connected to a vacuum pump, a pressure gauge and a supply of inert gas. Three-inch sections of wire mesh folded in cylindrical shapes were inserted into each of the arms to serve as the wicks. Provisions were made for several thermocouples by boring one-inch deep holes in the stainless steel cylinder. The chromel-alumel thermocouples were inserted and connected to calibrated direct readout temperature
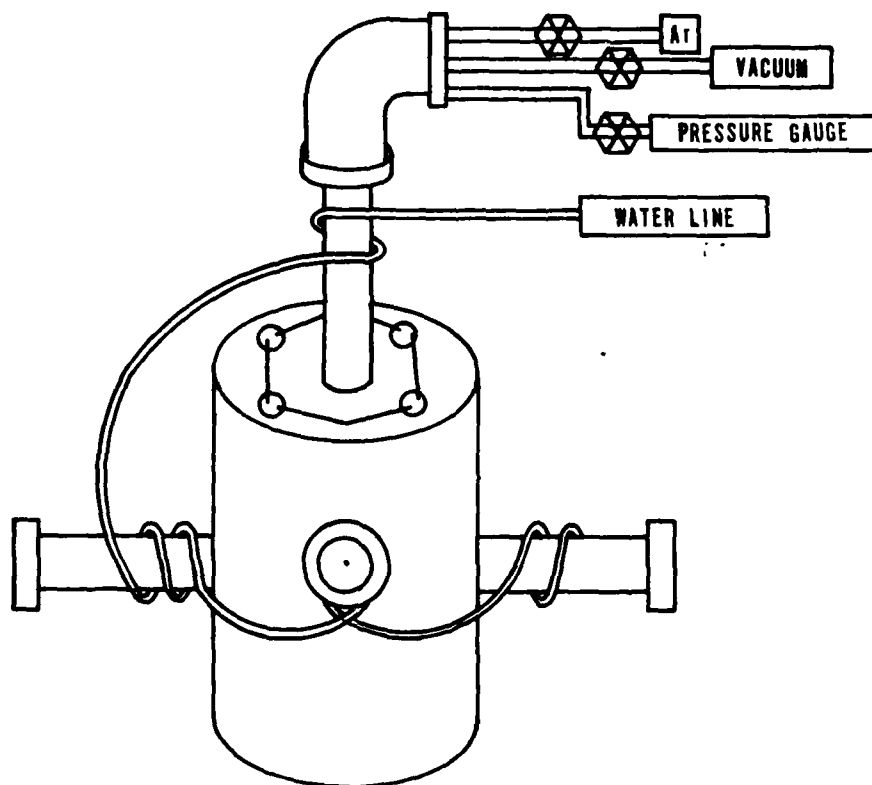
35

Figure 9 - Side View of Crossed Heatpipe

CONFIGURATION KEY

1. COOLING COILS
2. OUTER SUPPORT CANISTER
3. INSULATED REGION
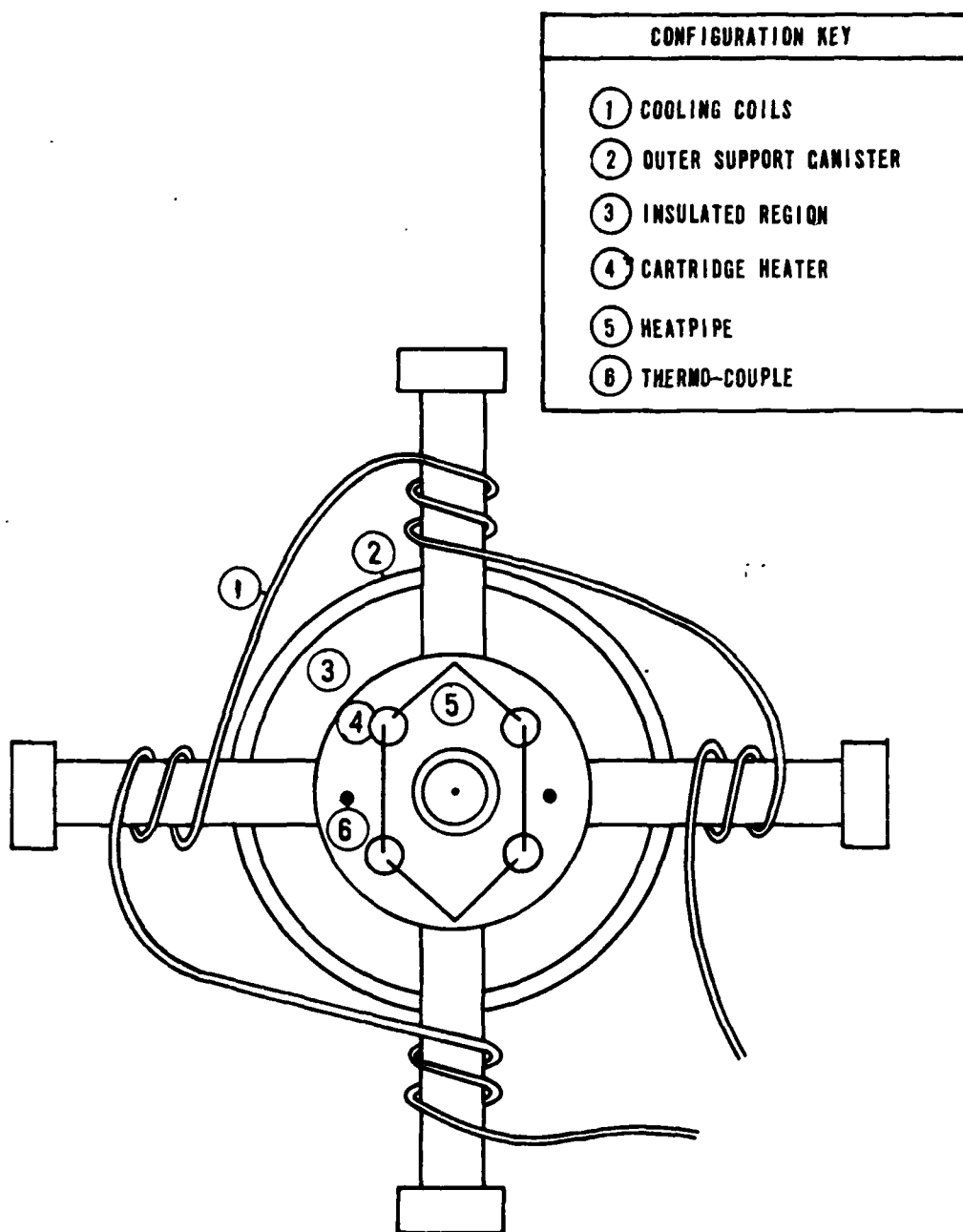4. CARTRIDGE HEATER
5. HEATPIPE
6. THERMO-COUPLE

Figure 10 - Top View of Crossed Heatpipe

controllers. The four 1KW heaters were connected in a series-parallel arrangement and then wired to a 22 amp Variac. The heatpipe itself was wrapped in high temperature insulation and was then enclosed in a support capsule, which allowed only the arms to extend. Metals were inserted into the heatpipe from the top by removing the elbow on the upper arm of the heatpipe as shown in Figure 9. The heatpipe was operated at temperatures of 600°C to 1000°C which corresponded to Group I and Group II vapor pressures of 1-200 torr. The inert gas pressure was varied from 1-600 torr, depending on the pressures of the metals in the heatpipe. The inert gas pressure was always kept higher than the vapor pressure of the Group II metal. Three to four hours were generally required to bring the heatpipe to a stable temperature of 800°C. Several days operation with one fill of 2-5 grams of each metal was generally obtained.

3. Experimental Configurations

a. Emission Experiments

The purpose of the emission experiments was to detect the presence of LiMg and LiCa excimers by observation of spontaneous emission resulting from the $A^2\Pi$ and $B^2\Sigma$ to $X^2\Sigma$ transitions. To accomplish this various laser sources were used to excite the alkali metal, which in turn was expected to react with the alkaline earth producing the excimer.

The experimental configuration is shown in Figure 11. A listing of all equipment used in all the experiments is shown in Appendix A. The output of an Ar+ laser, or a dye laser pumped by an Ar+ laser was modulated by a mechanical chopper at 10Hz-1KHz, reflected off of two turning mirrors and passed through a Brewster window into the heatpipe

38

where it was absorbed by the species in the heatpipe. The resulting fluorescence was focused by a lens, dispersed by a one-meter scanning monochromator and projected on a detector. A water-cooled photomultiplier tube sensitive from 400-1000nm and an intrinsic Ge, liquid nitrogen cooled solid state detector, sensitive from 800-1800nm were used to observe the fluorescence.

When the photomultiplier was used, the signal was first amplified and then analyzed by a phase sensitive detector. The output of the Ge detector was transmitted directly to the phase sensitive detector. The resulting output signals were then recorded on the chart recorder. By scanning the monochromator at a fixed rate (A/min) and setting the chart recorder speed at a fixed rate (cm/min), an intensity profile of the emission from the heatpipe as a function of wavelength was obtained.

Several considerations were important in conducting these experiments. First, the laser output had to be stable in both power and frequency. Next, the $f^{\#}$ of the focusing lens system with the heatpipe arm as its constraining aperture had to be matched to the $f^{\#}$ of the monochromator for maximum light collection efficiency. Additionally, the resolution of the monochromator was matched to the product of the scan rate of the monochromator and the integration time of the phase sensitive detector. Finally, the phase reference of the lockin amplifier was adjusted for maximum output signal.

Several calibrations were performed to insure that accurate data were obtained. The wavelength reading on the monochromator was calibrated using Ar, Hg, and Ne lamps which emitted standard spectral lines. The monochromator was found to be accurate to ±1A over the
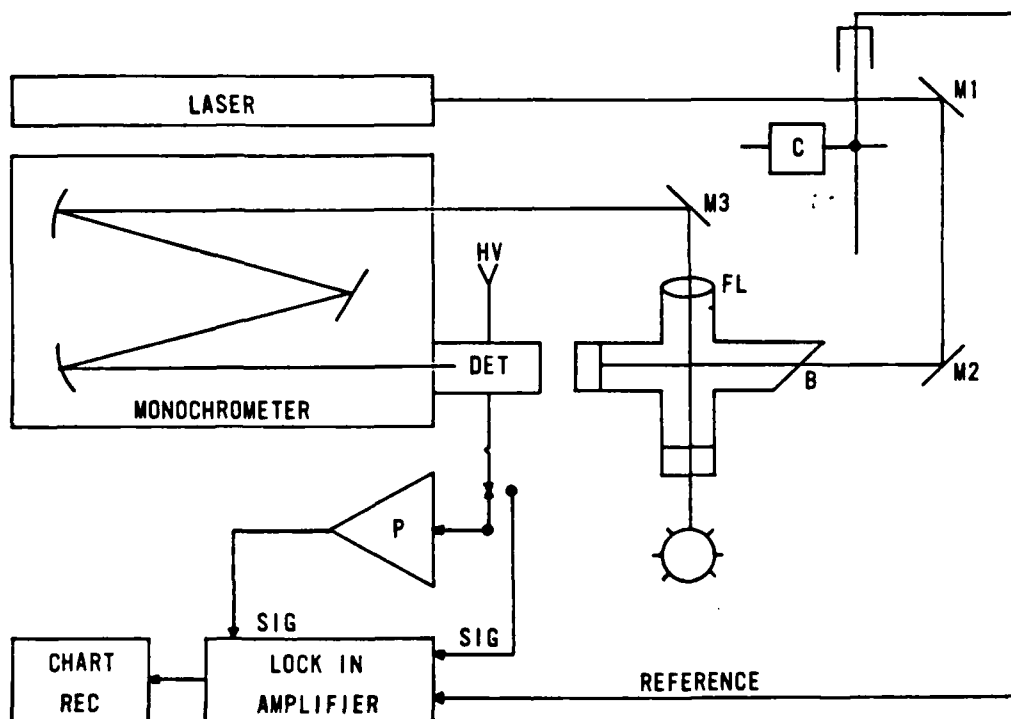
39

Figure 11 - Chemiluminescence Experiment Configuration

range of 650-1200nm. The combined accuracy of the scan rate of the monochrometer(A/min) and the scan rate of the chart recorder(cm/min) was determined to be $\pm$.01A/cm. Additionally, the combined detector/monochrometer response curve was mapped from 450nm to 1100nm using a standard blackbody source operating at 1000°C.

b. Absorption Experiments

Absorption experiments which utilized both a white light source and a laser source were performed to determine the presence of species not detected in emission and to monitor changes in species concentrations.

The white light absorption experiments were performed by modifying the setup in Figure 11. The laser was removed and a quartz halogen lamp was focused through one arm of the heatpipe. The mechanical chopper was moved to a position between the light source and the monochromator. A pin-hole was also placed in front of the light source to limit the intensity of the source and define the source aperature. The same general procedures of scanning the mono-chromator as a function of wavelength while recording the signal on a chart recorder were followed. Observed variations in intensity as a function of wavelength were then correlated to absorptions by species in the heatpipe.

Another set of experiments were designed to monitor the absorption of a laser source. In these experiments an Ar^+ laser operating on a wavelength resonant with one of the Li_2 transitions as shown in Table XI[46] was passed directly through the heatpipe. Its power was measured both before and after th- heatpipe at various

ble XI - Li$_2$(X-B) Transitions Resonant With Ar$^+$ Lines

λ	B$^1\Pi$		X$^1\Sigma$	
	v'	J'	v''	J''
458	9	9	2	8
	9	5	2	5
476	4	24	1	24
488	2	31	1	30
	6	45	3	46
	4	73	0	74
514	9	38	9	37
	3	30	5	29
	8	61	7	61

temperatures with just Li and with Li in combination with Mg. The results after measuring and accounting for losses on the windows provided infomation on the alkali metal concentrations and perturbations to these concentrations due to chemical reactions or large photon fluxes.

D. Results and Analysis

1. Introduction

Laser induced chemiluminescence experiments were initially performed with many different combinations of Group I/II metals utilizing the emission experiment configuration previously described. Li, Na, and K were tested in combination with Mg, Ca, Sr, Ba, Zn and Cd. In all cases the intent was to optically excite an alkali dimer or interalkali diatomic which would chemically react with the Group II metal to form an excimer whose spontaneously decay could be observed. Only the combinations of Li and Mg and Li and Ca led to the observation of emissions that could not be explained in terms of previously analyzed alkali metal or alkaline earth diatomics. The following sections will describe the results of the experiments with Li, Mg and Ca.

2. Absorption Experiments

An initial characterization of the species present in the heatpipe was performed to determine impurity levels prior to conducting emission experiments. Additionally, interactive effects between the Li and Mg or Ca such as vapor pressure suppression were assessed.

With the experimental apparatus configured for the white light absorption experiments, the spectrum shown in Figure 12 was obtained with only Li in the heatpipe at a temperature of 900°C and 432 torr

total pressure. The published Li and Li_2 vapor pressures at 900°C are 2.5 and .1 torr, respectively. The absorbing species were identified using published spectroscopic data.[43-45] The primary absorptions resulted from the Li_2 ($X^1\Sigma-A^1\Pi,B^1\Pi$) and $Li(^2S-^2P)$ transitions. There were several impurities present (Ba, Na, K). Their concentrations were at least two orders of magnitude less than the Li concentration based on comparison of the relative absorption areas for these equally strong absorbers. Trace amounts of Ca were also evident. Addition of Mg to the heatpipe resulted in the appearance of the Mg absorption shown at 457nm. The observation of Mg absorption on the forbidden $^1S-^3P$ transition was indicative of large concentrations. When either Mg or Ca were added, no additional impurities were observed and no changes were noted in the strength of the Li and Li_2 absorptions. Therefore, there was no apparent supression of the Li/Li_2 concentrations from the addition of Mg.

Figure 13 shows the results of the laser absorption experiments for one set of temperatures. The absorption on the Li_2(X-B) transition is linear in laser power for the case of Li alone and for Li + Mg present in the heatpipe for laser powers of .08 watts to 1.1 watts. The significance of the linear response will be discussed in the next chapter. Additionally, there is less than a 10% difference in the laser absorption profiles with and without Mg present. Computing an average value of I/I_o for each set of data and applying Beer's law, $[Li_2]\sigma l$ varies by only 3%. These results indicate that the addition of Mg does not suppress or perturb the Li_2 density within the accuracy of the experiment (±10% due to temperature variations). The laser absorption data supports the qualititative data from the white light
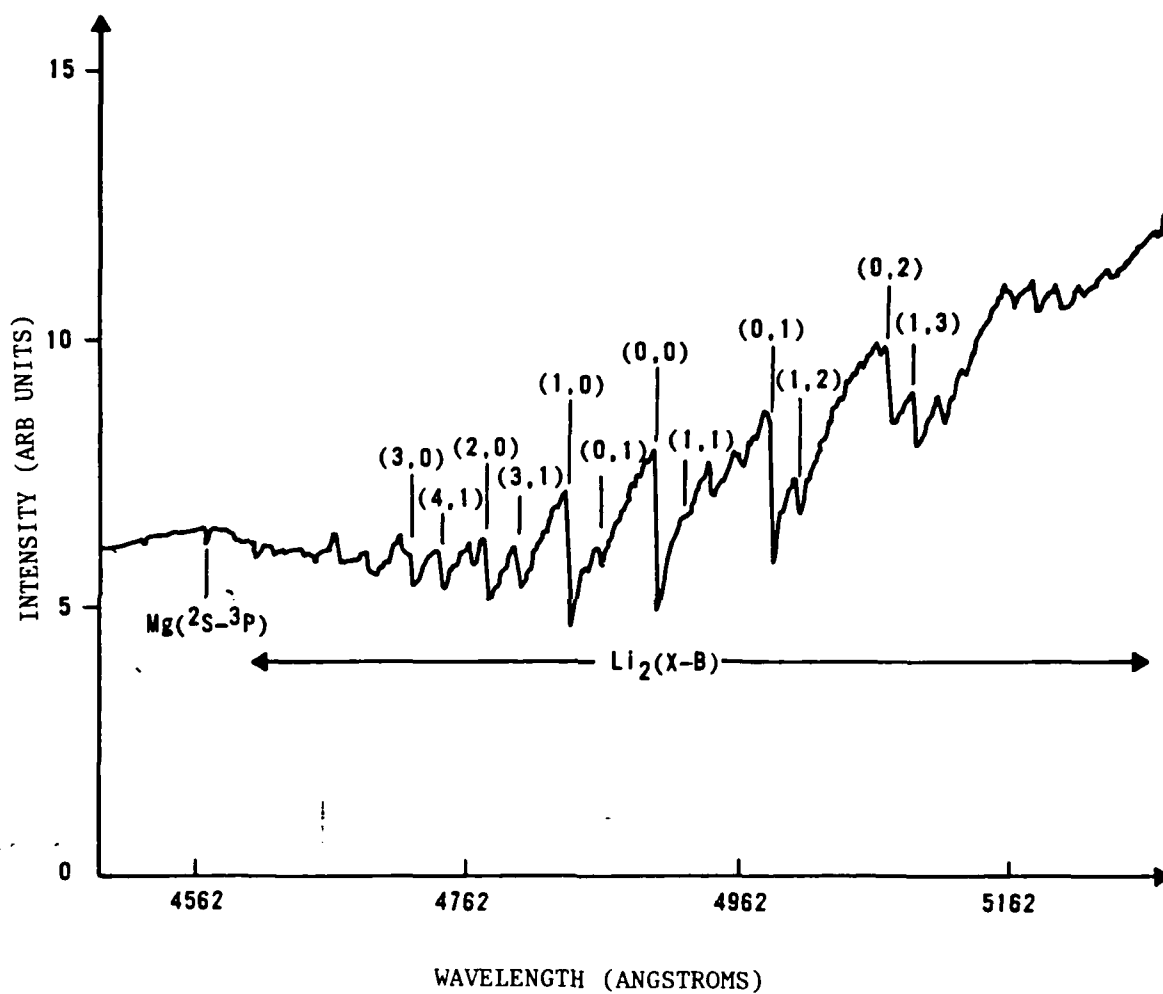
44

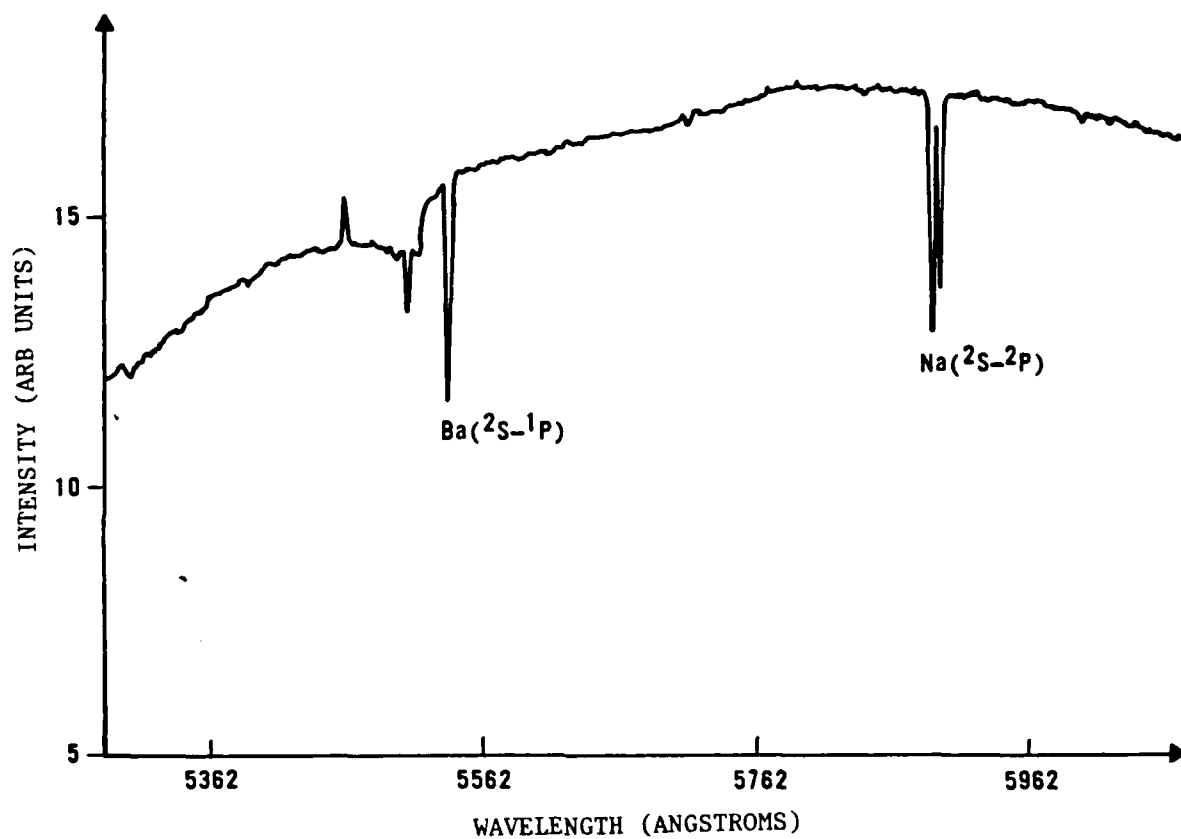Figure 12(a) - Li Absorption Spectrum 450 - 520nm

45

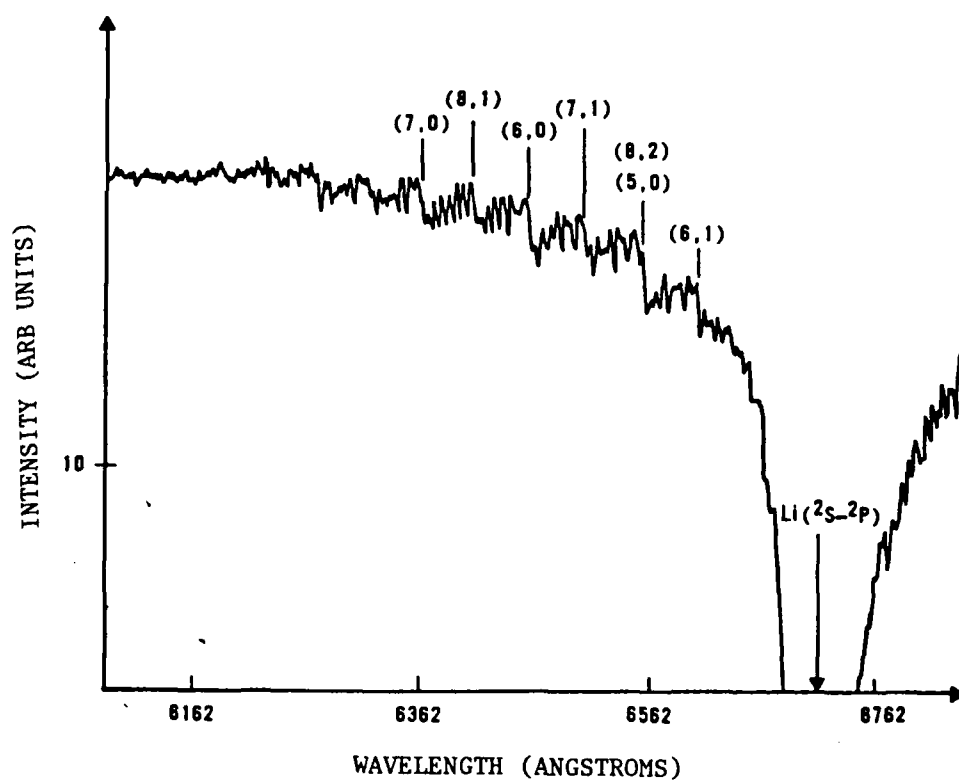Figure 12(b) - Li Absorption Spectrum 530 - 600nm

46

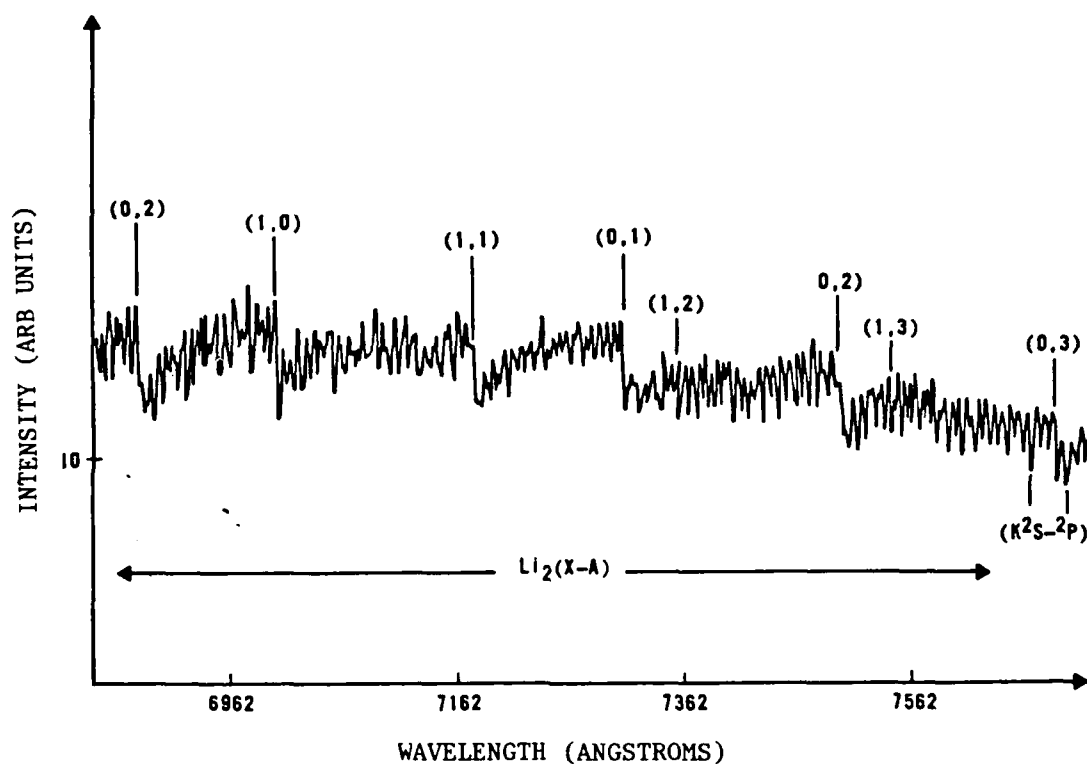Figure 12(c) - Li Absorption Spectrum 610 - 680nm

47

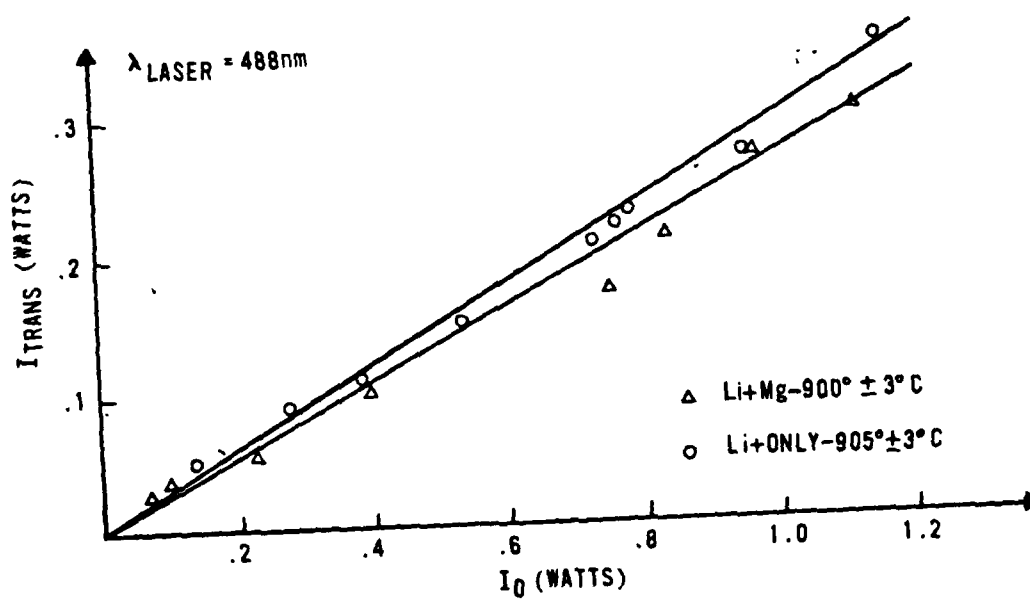Figure 12(d) - Li Absorption Spectrum 690 - 760nm

48

Figure 13 - Laser Absorption Data

absorption experiments and provides the additional information that no
perturbation is observed as a result of the absorption of the laser
light and subsequent excited state reactions involving Mg. Therefore
published data on the vapor pressures can be used to determine the
species number densities at a given temperature.

2. Fluorescence Experiment Results

a. Results

As in the absorption experiments, emission spectra were recorded
with only Li, Mg, and Ca and combinations of Li and Mg and Li and Ca.
The results of the Li only experiments are shown in Figure 14. The
spectrum was recorded with Li present at a temperature of 900°C and
total pressure of 400 torr with the Ar+ laser operating on the 488nm
line at 1 watt output power. Various other lines of the laser (476
and 458nm) also resulted in observation of the same emissions only
varying in intensity. The spectra were assigned as shown and the
observed emissions were identified as Li_2(B-X), 470-530nm; $Li(^2P-^2S)$,
671nm; and Li_2(A-X), 630-900nm; based on comparison of observed
emissions to published data.[43-45] No emission was observed from any
impurities. Additionally, no emission whatsoever was observed at
wavelengths of 930nm-1300nm. Emission spectra taken under the same
conditions with only Mg or Ca present showed no emission in the range
of 450nm-1300nm.

The combinations of Li/Mg and Li/Ca resulted in observation
of the Li emissions described above reduced in intensity 50-70% with
the added features shown in Figures 15 and 16, respectively.

Several experiments were performed to determine the source of these
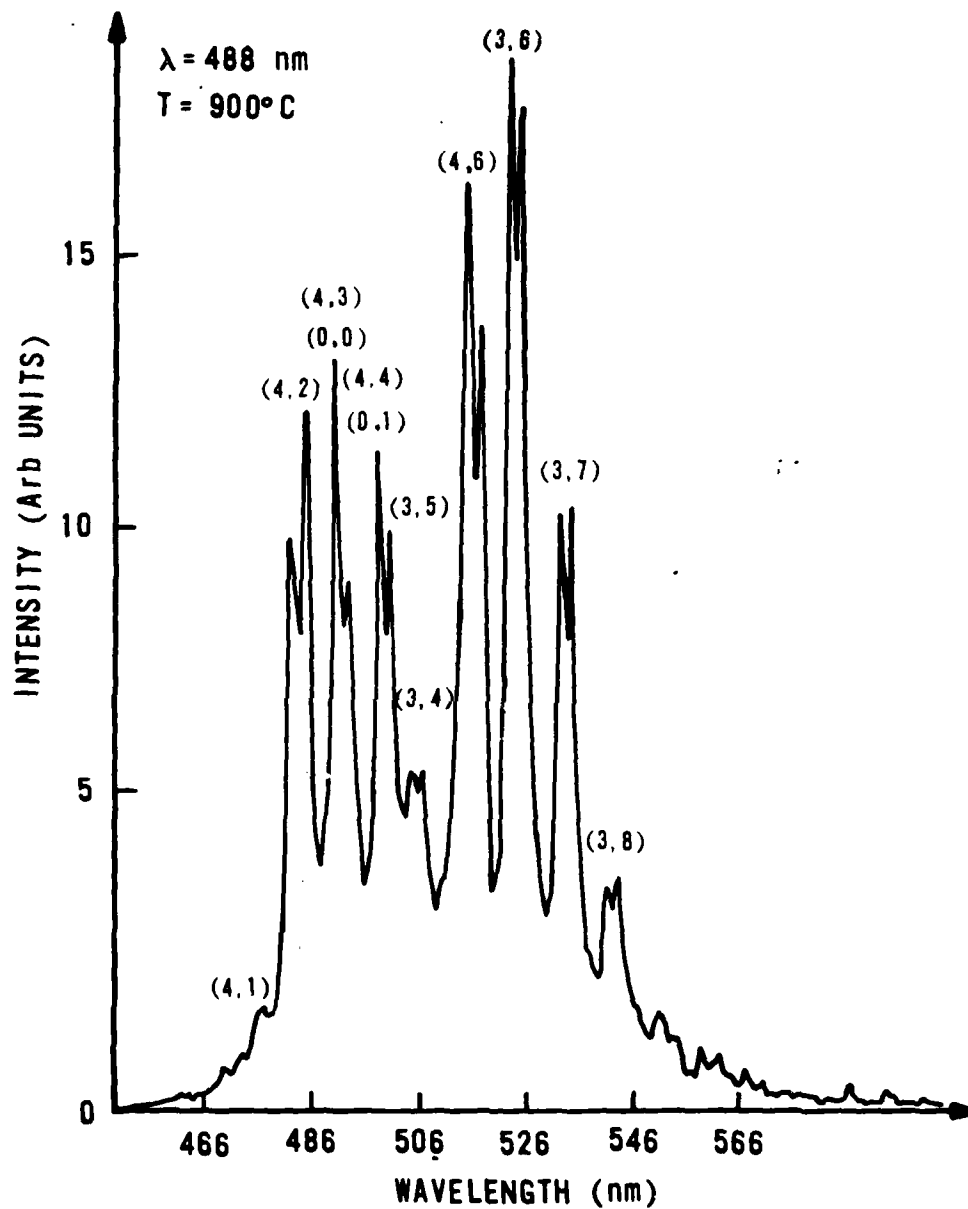new emissions and the mechanisms by which they were produced. In both

50

Figure 14(a) - Li_2(B-X) Fluorescence 460-560nm

51

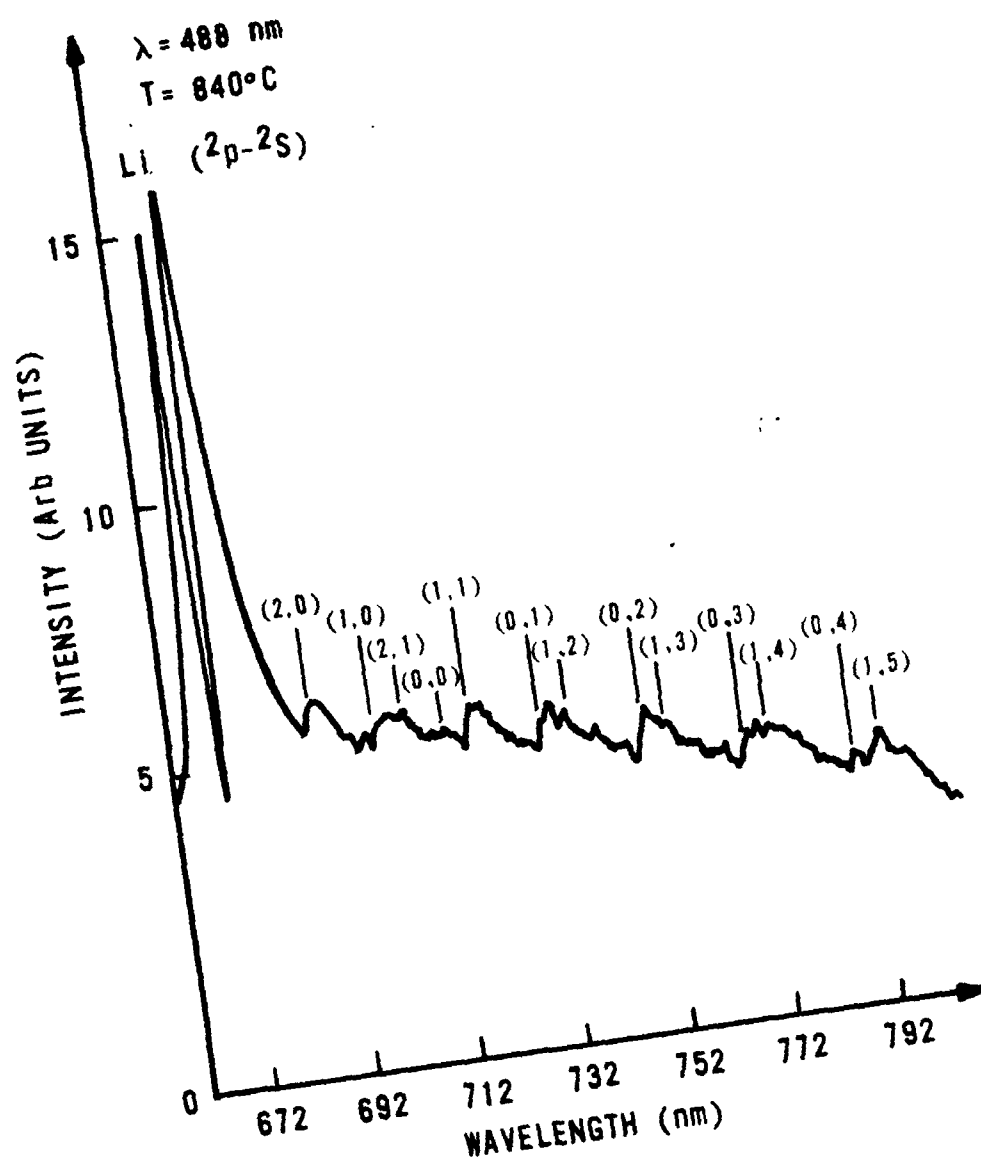Figure 14(b) - Li$_2$(A-X) Fluorescence 660-790nm
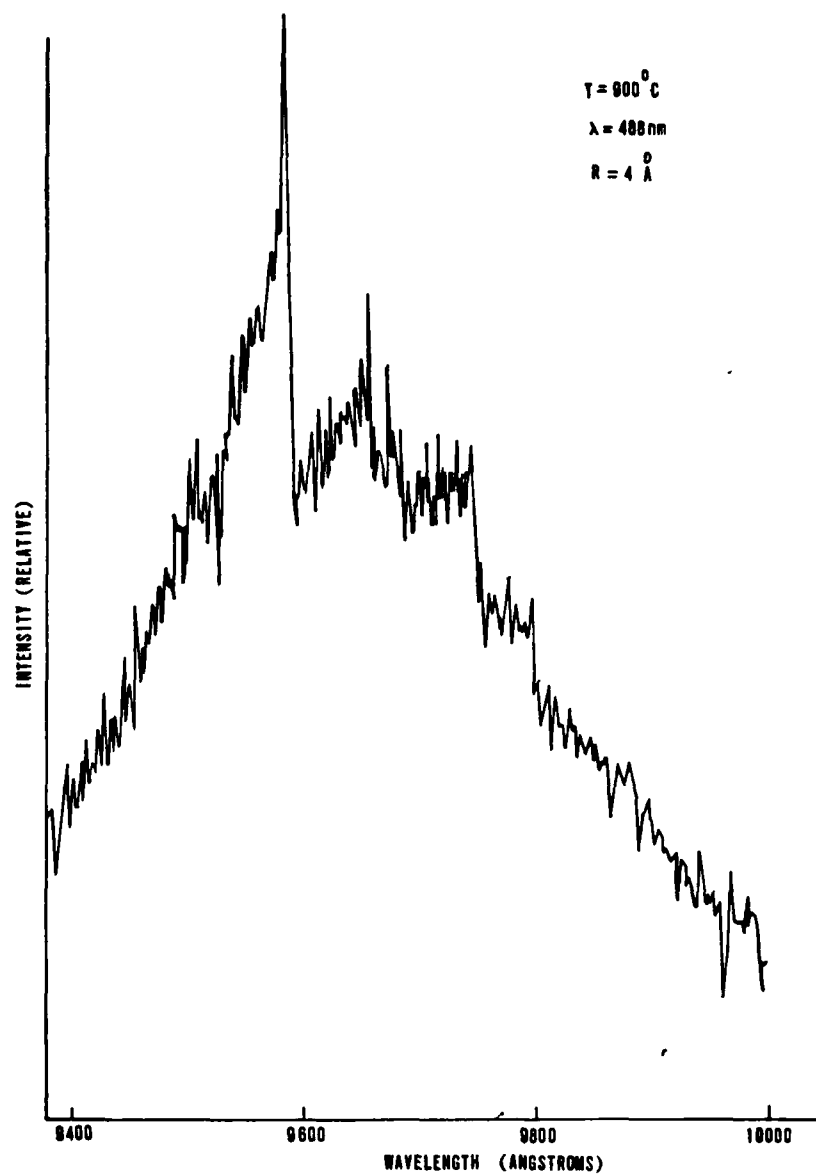
52

T = 900°C
λ = 488nm
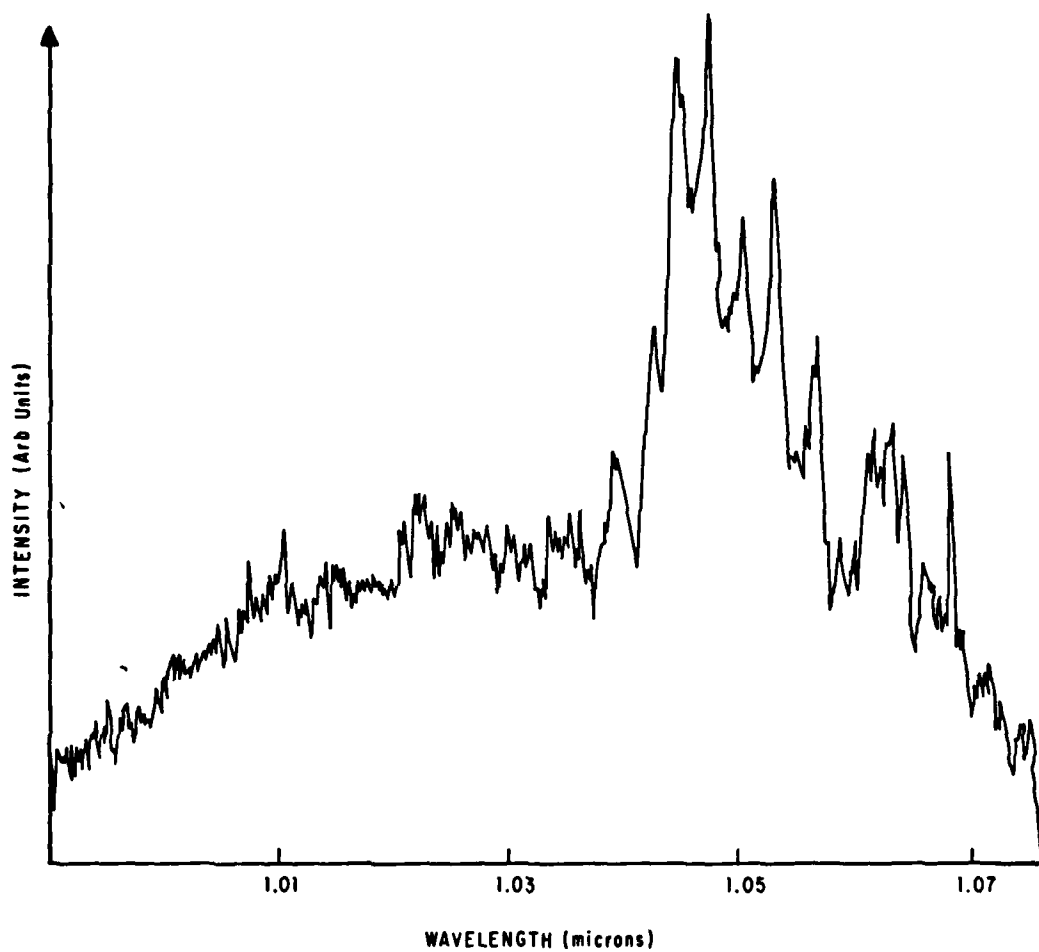R = 4 Å

Figure 15 - LiMg Emission

53

Figure 16 - LiCa Emission

cases large amounts of impurities (K, Na, Ba) were introduced into the heatpipe. No effect was observed on either spectrum. Additionally Ne was substituted for Ar as the inert gas again with no effect. This led to the conclusion that Li and Ca or Li and Mg were the only participants in the emission. In addition, the dependence of the intensity of the LiMg emission on laser power and inert gas pressure was investigated. Figures 17 and 18 show that the dependence on laser power was linear and there was an inverse dependence on inert gas pressure.

A qualitative investigation of the temperature dependence of the emission intensity showed that the LiMg intensity maximized at 900°C and was first detectable was 800°C. The LiCa emission was first visible at 920°C and was still increasing at the maximum temperature of operation 970°C.

In addition to the 1040nm spectrum observed with Li and Ca present in the heatpipe, the feature shown in Figure 19 was also observed. Under higher resolution numerous bandheads were observed. The 780nm emission exhibited a vibrational spacing of $\omega_e' = 130/cm$, $\omega_e'' = 70/cm$ and $\Delta T_e = 13,070/cm$. The observed emission did not correlate to any predicted LiCa transitions. Additionally, the formation of highly excited LiCa would have had to result from energy pooling processes and therefore the emission intensity should be quadratic in laser power. Figure 20 shows that the power dependence is clearly linear. Vibrational analysis suggests that the emission correlates to a previously unobserved transition between the first excited state of $Ca_2(Ca(^3P)+Ca(^1S))$ since the ω_e'' agrees with previously determined values for the ground state spacing for Ca_2.[47]
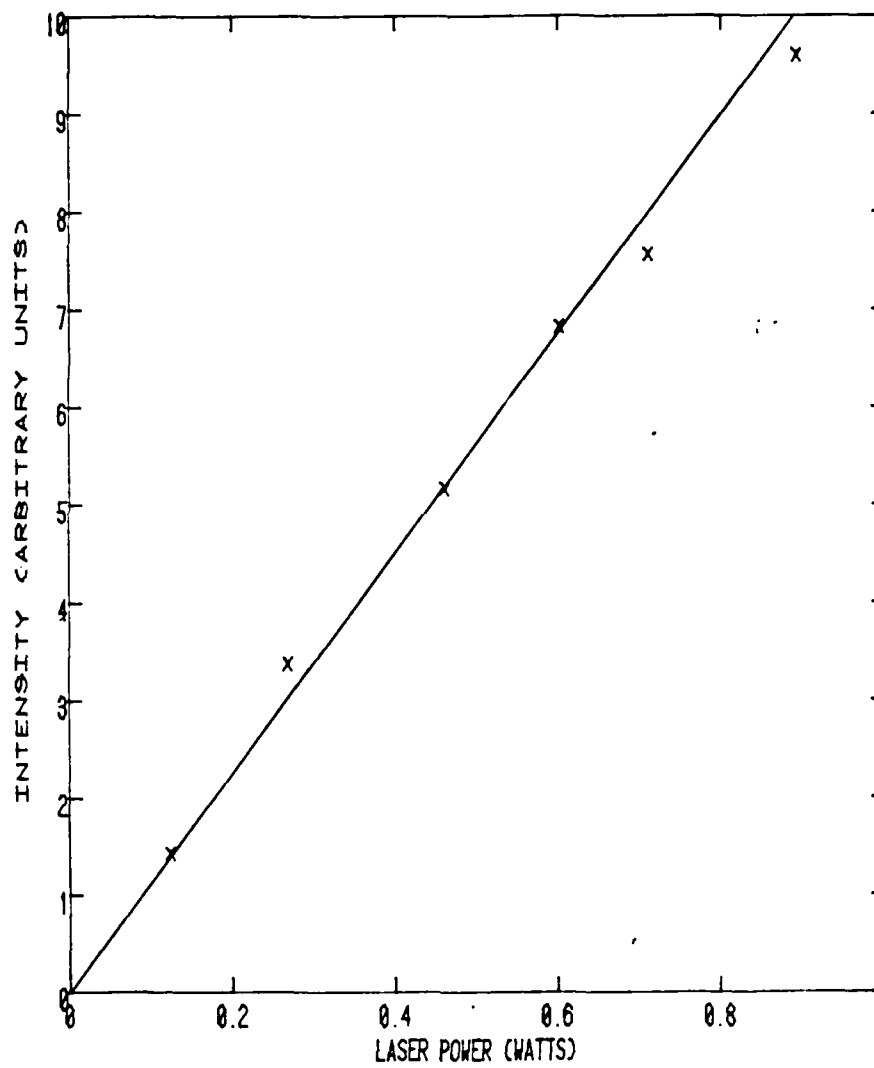
55

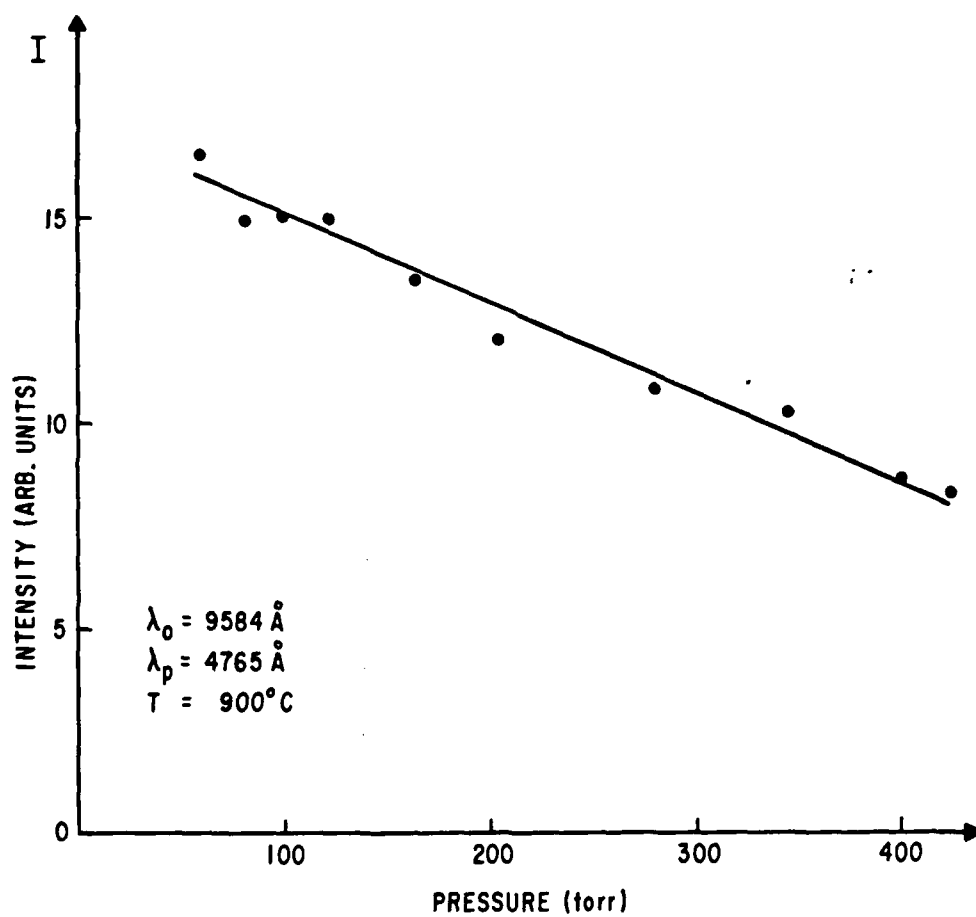Figure 17 - LiMg Emission Intensity Dependence on Laser Power

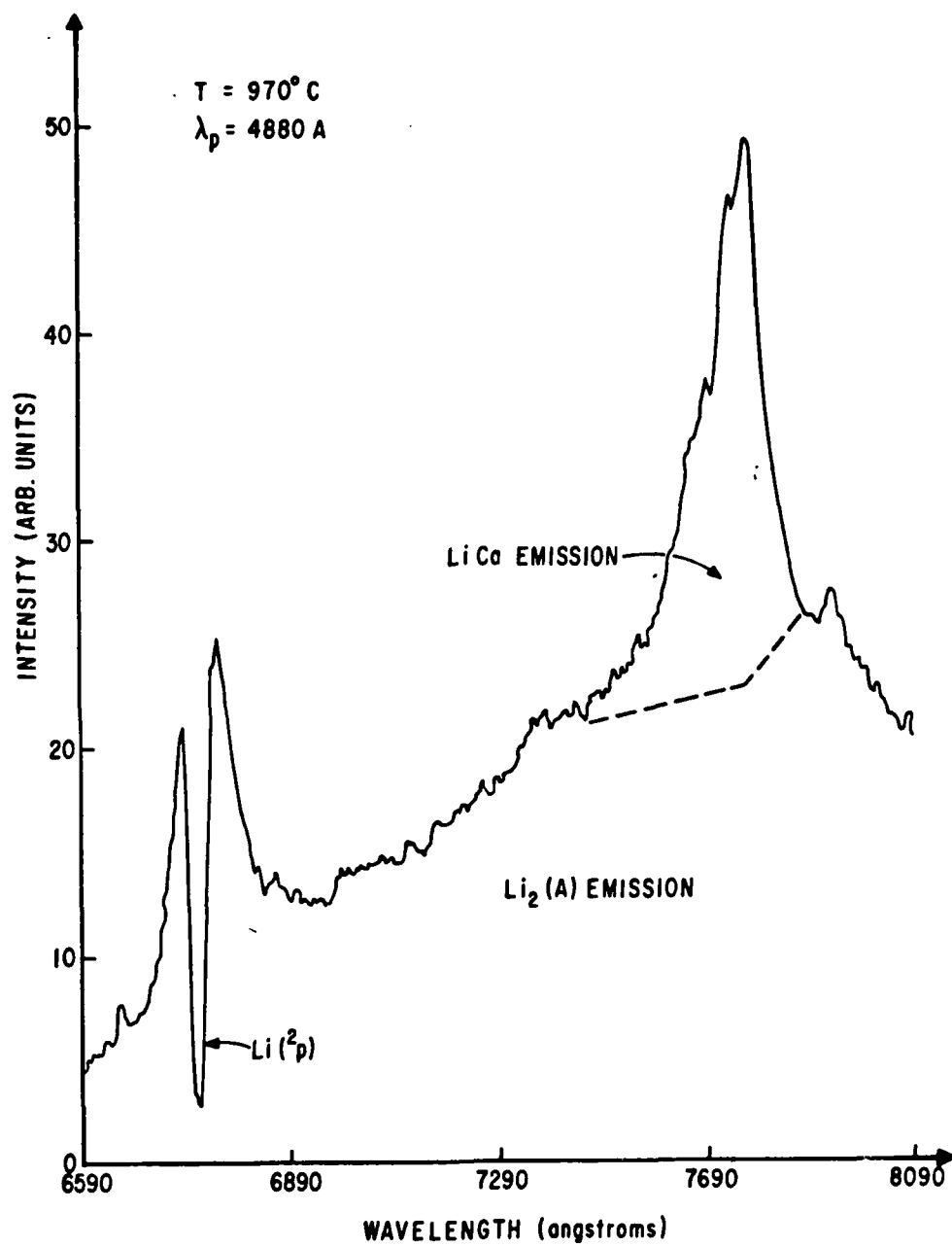Figure 18 - LiMg Emission Intensity Dependence on Inert Gas Pressure

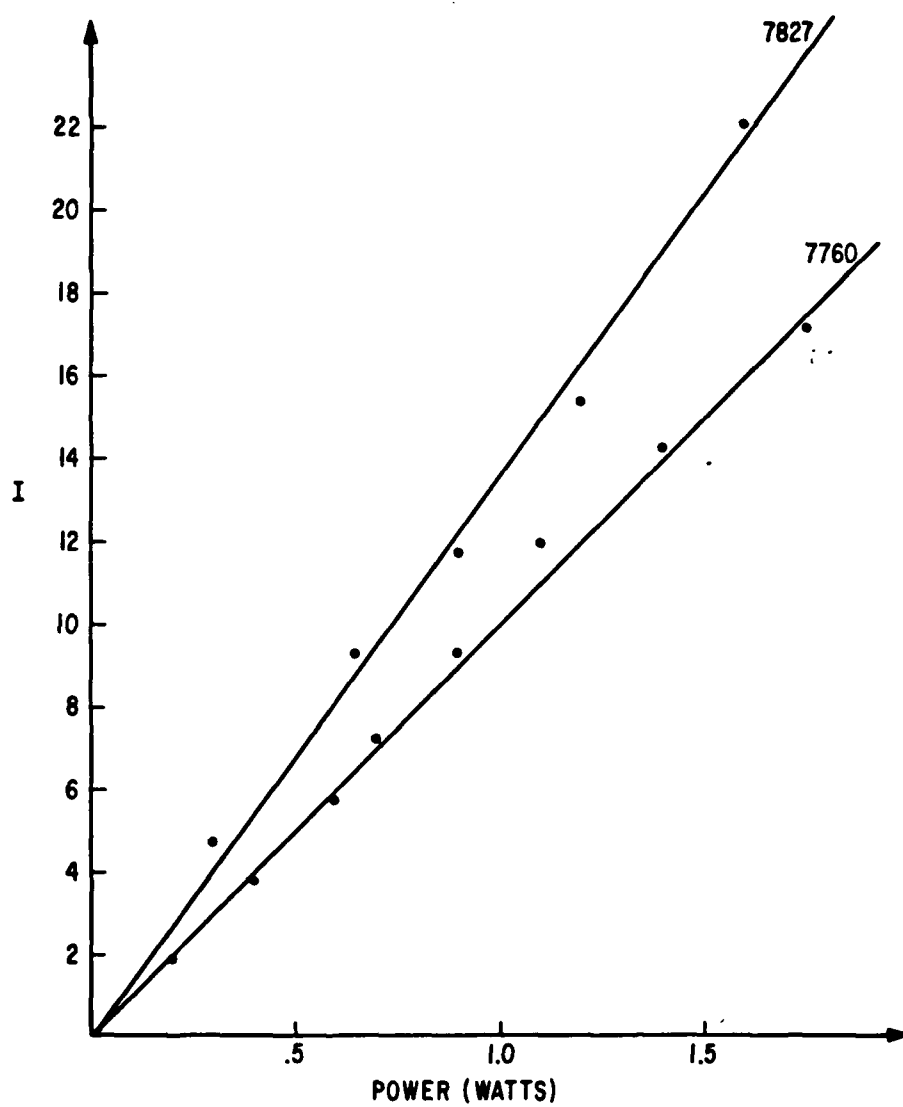Figure 19 - Li/Ca 780nm Emission

Figure 20 - LiCa 780nm Emission Intensity Dependence on Laser Power

b. LiMg and LiCa Spectroscopic Analysis

Both the 960nm LiMg emission and 1040nm LiCa emission exhibited
band heads characteristic of bound-bound diatomic spectra as well as
continuum structure characteristic of excimer emission. Analysis of
the emission was limited by several factors. Since, the excimers were
formed by chemical reaction there was no selective way of producing a
given upper state vibrational level as in a laser fluorescence
experiment so that individual vibrational transitions could be
isolated. Additionally, the observed vibrational progressions
included only a few vibrational levels. A crude analysis was performed
based on the assumption that the ground state is much more weakly
bound than the excited state. Therefore smaller spacings were assigned
to the lower state and larger spacings to the excited states.
Additionally, it was assumed that the upper and lower state potential
curves were not shifted very much from one another. This results in
transitions such as $v'=0$ to $v''=0$, $v'=1$ to $v''=1$. If there is a large
shift, the more likely transitions might be $v'=4$, 5, 6 to $v''=0$ for
example. The data provided no way to distinguish between the two
cases. Using these assumptions the vibration assignments shown in
Tables 12 and 13 were made for the 960nm LiMg emission and 1040nm LiCa
emission. The resulting spectroscopic constants are shown in Tables 14
and 15 with the calculated constants from Tables 1 and 2 in parenthesis.

The experimental results for LiMg and LiCa can now be compared to
the theoretical predictions from Tables 3 through 10 as shown in
Tables 16 and 17. The LiMg results show that the experimentally derived
vibrational assignment for the upper state was shifted by four
vibrational levels.

Table XII - LiMg Spectral Assignment(λ-nm)

v' v"	0	1	2
0	974.4	951.4	---
1	979.4	955.4	---
2	---	958.4	935.6

Table XIII - LiCa Spectral Assignments(λ-nm)

a) $A^2\Pi-X^2\Sigma$

v' v"	0
0	1049.9
1	1056.3
2	1062.7
3	1067.6

b) $B^2\Sigma-X^2\Sigma$

v' v"	0	1
0	1047.0	---
1	1052.7	---
2	1058.7	1038.0
3	---	1044.1

Table XIV - LiMg Spectroscopic Constants

State Constant	$X^2\Sigma$	$A^2\Pi, B^2\Sigma$
T_e(ev)	0	1.27(1.12,1.56)
D_e(ev)	---	.58(.76,.30)
ω_e(1/cm)	50(60)	250(302,328)
$\omega_e\chi_e$(1/cm)	23(7)	---

Table XV - LiCa Spectroscopic Constants

State Constant	$X^2\Sigma$	$A^2\Pi$	$B^2\Sigma$
T_e(ev)	0	1.181(1.08)	1.184(1.17)
D_e(ev)	---	.666	.663
ω_e(1/cm)	55(93)	---	188(197)
$\omega_e\chi_e$(1/cm)	5(7)	---	---

Table XVI - LiMg Experimental vs. Predicted Spectrum

v'	v"	Wavelength (microns)		Relative Intensity	
A²Π	X²Σ	λ_{calc}	λ_{obs}	calc	obs
3	0	1.0060	------	----	----
	1	1.0011	------	----	----
4	0	.9770	.9744	.08	.54
	1	.9810	.9794	.15	.33
5	0	.9512	.9514	.13	.51
	1	.9552	.9559	.25	.81
	2	.9592	.9584	.38	1.00
6	0	.9268	-----	.38	---
	1	.9312	-----	.54	---
	2	.9342	.9356	.69	.22
7	0	.9037	-----	.77	---
	1	.9109	-----	1.00	---

Table XVII - LiCa Experimental vs. Synthetic Spectrum

v'	v"	Wavelength (microns)		Relative Intensity	
$B^2\Sigma$	$X^2\Sigma$	λ_{calc}	λ_{obs}	calc	obs
0	0	1.0472	1.0470	1.00	1.00
	1	1.0531	1.0527	.53	.60
	2	1.0593	1.0587	.18	.10
	3	1.0650	--	.03	--
1	0	1.0260	--	.12	--
	1	1.0320	--	.07	--
	2	1.0379	1.0380	.34	.40
	3	1.0441	1.0441	.44	.50
$A^2\Pi$	$X^2\Sigma$				
3	0	1.0501	1.0499	.24	.30
	1	1.0569	1.0563	.28	.40
	2	1.0625	1.0627	.24	.25
	3	1.0679	1.0676	.18	.15

Even after this correction, there is poor agreement between the intensity distributions. The discrepancies observed in the spectroscopic constants can be clarified after matching the calculated spectra to the experimental spectra.

Examining LiMg first, Table 16 shows the comparison of experiment to theory. The first important point is that the observed emission can be assigned to the $A^2\Pi-X^2\Sigma$ transitions. The assigned transitions, however, were off by four vibrational levels in the upper state (ie, the observed transitions are 4,0; 5,0; etc, not 0,0; 1,0) The discrepancies in the vibrational constants result from the inability to account for the rotational effects in the experimental data. The term in the energy equation for a vibrational and rotational level that includes coupling of vibrational motion and rotational motion is $\alpha_e(V+\frac{1}{2})(J(J+1))$. For large J values ($J_{max}$ ~35 for T=900°C) this introduces a shift in the spectrum that is proportional to the vibrational quantum number which in effect reduces the observed vibrational spacing.

There are several other apparent discrepancies between the theory and experiment. The theoretical calculations indicated that the most intense emission should emanate from the LiMg $B^2\Sigma$ states in the region of 700-800nm. If the formation reaction is $Li_2(B)$ and Mg --> LiMg and Li, then there is 11,600/cm energy available for population of LiMg states (Li_2 is bound by 8900/cm and a 488nm photon carries 20,500/cm energy resulting in 11,600/cm available energy). Since T_e of LiMg $B^2\Sigma$ is 12,600/cm this state is not accessible to the formation reaction and no $B^2\Sigma-X^2\Sigma$ emission should be observed.

The reaction to form LiMg($A^2\Pi$) v'=0 is 2400/cm exothermic and
thermochemically neutral for $A^2\Pi$, v'=8. The exothermicity of the
reaction may provide the basis for explaining the apparent discrepancy
between the observed and calculated $A^2\Pi$-$X^2\Sigma$ intensity profiles shown
in Table 16. The chemical reaction may be selectively populating the
lower vibrational levels.

An alternative explanation for the intensity variation is an
error in the calculation of the ground state potential. Small changes
in the shallow ground state potential will shift the classical turning
points of the vibrational levels resulting in significant changes in
the Franck-Condon envelope.

A small shift of the classical turning points of the ground
state vibrational levels to shorter internuclear separation (.3Å)
either from an inward shift of the entire ground state well (3.9Å-->
3.6Å; less than a 10% change) or from a change in shape would shift
the intensity maximum from the calculated v'=9, v"=0 to v'=4, v"=0
transition.

The observed continuum emission from LiMg peaks at a wavelength
of 960-980nm which is consistent with the fact that the most intense
bound-bound emission results from v'=4, 5, 6.

Excellent agreement was obtained between theory and experi-
ment in the case of LiCa as shown in Table 17. The experiment provides
evidence that emission results from population of the $A^2\Pi$ and $B^2\Sigma$
states. Since these states lie lower in energy than the corresponding
states in LiMg ($A^2\Pi$, T_e = 8711/cm and $B^2\Sigma$, T_e = 9437/cm) there is
sufficient energy available in the formation reaction (11,600/cm) to
populate both states. Finally, the LiCa ground state was easier to

66

calculate because it has substantially more binding than the LiMg ground state (580/cm vs 135/cm)-see tables I and II. Both of these factors may have led to closer agreement in the LiCa case.

Figure 21 demonstrates the agreement between the calculated and experimental bound-continuum emission spectrum as well as the bound-bound spectra. The continuous emission which originates from transitions from the $v'=3$, 4, 5 of the $B^2\Sigma$ state to the continuum, peaks in the region of 1010nm as predicted theoretically. For purposes of clarity the bound-bound emissions were not weighted by the large number of rotational transitions emitting times their Doppler width. This results in the apparent amplitude discrepancy between the bound-bound and bound-continuum theoretical spectra.

Finally, it should be noted that there was good agreement between the observed and calculated spectroscopic constants with the exception of the ground state ω_e. As in the case of LiMg, this discrepancy can be accounted for by consideration of the large vibrational-rotational coupling constant for the ground state, together with the larger rotational quantum numbers ($J_{max}=40$) resulting from the high temperature.

E. Summary of Results

A study of combinations of Group IA/IIA metals resulted in the identification of two new emitters, LiMg and LiCa. These species were produced as a result of an initial excitation of $Li_2(B)$ and subsequent chemical reaction. The observed emissions were correlated with the results of ab initio calculations with good agreement. Several other pieces of data were obtained on LiMg which will affect the kinetics analysis as explained in the next chapter.
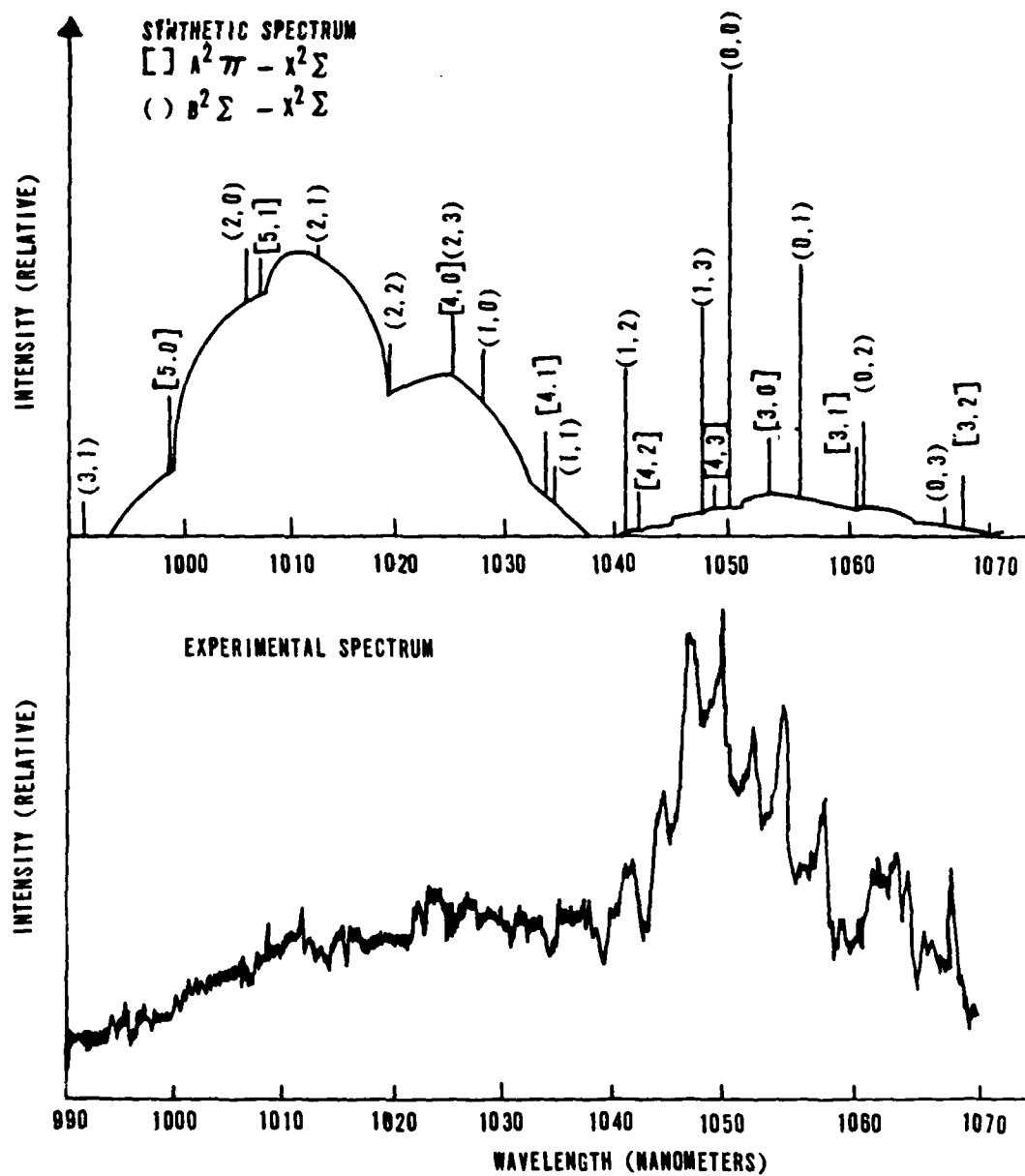
67

Figure 21 - LiCa Theoretical Spectrum Compared to Experimental Results

68

Chapter III - LiMg Kinetics

A. Introduction

This chapter presents an analysis of the kinetic processes
relevant to gas phase Li/Li_2 and $Li/Li_2/Mg$ systems. A kinetic model
is developed based on the experimental observations from the previous
chapter and published studies of the equivalent Na/Na_2 and K/K_2
systems.[48] Time dependent and steady state analyses of the rate
equations are presented and correlated with experimental measurements
of time delays and relative intensities to determine the rate
constants.

B. Theory

1. Species Concentrations in a Li/Mg gas.

The primary constituents of an equilibrium gas phase mixture
of lithium and magnesium are Li, Mg, Li_2, Mg_2 and LiMg. The contributions
of polyatomics (Li_3, Li_2Mg, etc.) to the total pressure are assumed to
be negligible[59,60] since not only is their binding energy expected to
be small but their formation rates are also expected to be small since
the potential reactants (LiMg, Li_2, etc.) are expected to be present
in small concentrations. The gas phase concentrations of Li atoms, Li
dimers and Mg atoms have been measured to within 15% uncertainty in
pure Li or pure Mg gases from 200°C to 1000°C as described in Nesmeyanov[51]
and are best characterized by the expressions shown in Appendix B.
Based on the experimental data shown in Chapter 2, it will be assumed
throughout this study that the Li_2, Li and Mg densities can be determined
directly from Nesmeyanov's expressions for their unperturbed equilibrium

vapor pressure curves.

There is no published data on the equilibrium concentrations of LiMg and minimal data on Mg_2. Mg_2 has been observed in a pure Mg gas and its ground state was determined to be bound by 400/cm.[52] Utilizing this information, the Mg_2 density in a pure Mg gas was calculated as shown in Appendix C. The density ratio Mg_2/Mg was determined to be 1.6 X 10^{-4} at 900°C which was a typical experimental operating temperature. Equilibrium arguments can be used to estimate the effect of Li on Mg_2 densities. The LiMg equilibrium concentration can be obtained similarly. The Mg_2 density is coupled to the Li_2 density through LiMg as shown below:

$$Mg_2 + Li \leftrightarrow LiMg + Mg$$
$$Li_2 + Mg \leftrightarrow LiMg + Li$$
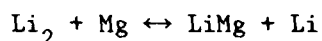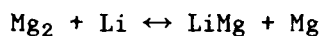
The first reaction is nearly thermoneutral since the equilibrium constant is $\exp(-\Delta E/kT)$ = .3 for kT = 800/cm at 900°C and ΔE is determined from the difference of the Mg_2(400/cm) and LiMg(135/cm) bond energies. Therefore nearly equal concentrations of Mg_2 and LiMg will be maintained. The second reaction is strongly driven to the left since Li_2 is bound by 8900/cm and the resulting equilibrium constant is 2.1 x 10^{-5}. In effect the Li_2 concentration suppresses the LiMg concentration which in turn keeps the Mg_2 concentration low. This effect was quantified by application of the Gibbs-Duhem relationship[53] as shown in Appendix D. The results were Mg_2/Mg and LiMg/Mg ratios of 1.2 x 10^{-5} and 2 x 10^{-7} at the reference temperature of 900°C. Therefore, the result of adding Li to a pure Mg gas is to suppress the Mg_2 density by an order of magnitude and also produce a small equilibrium concentration of LiMg. Table XVIII summarizes the

absolute magnitude of all the species concentrations in the mixed LiMg

gas. The knowledge of these relative species concentrations will

provide the basis for determining the importance of competing

processes in the optically excited Li/Mg system.

Table XVIII - LiMg Gas Phase Concentrations at 900°C

Species	Concentration
Li	$9.0 \times 10^{16}/cm^3$
Li_2	$4.8 \times 10^{15}/cm^3$
LiMg	$1.8 \times 10^{11}/cm^3$
Mg	$9.0 \times 10^{17}/cm^3$
Mg_2	$1.1 \times 10^{13}/cm^3$

2. $Li_2(X)$ Perturbation Due to Photon Flux.

The data presented in Chapter 2, Figure 14, demonstrated that the

$Li_2(X)$ density at 900°C was unperturbed (±10%) by optical excitation

from a 488nm, 1 watt Ar^+ laser beam. A theoretical estimate of the

magnitude of the perturbation can be obtained from a rate equation

analysis of the $Li_2(B)$ concentration including both optical excitation

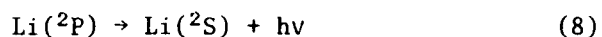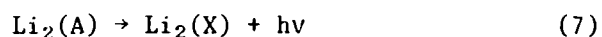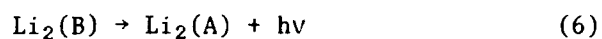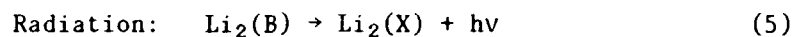and decay terms while ignoring stimulated emission:

$$d[Li_2(B)]/dt = I\sigma[Li_2(X)]/h\nu + [Li_2(B)]/\tau \qquad 2.1$$

where I is the intensity of the laser ($1W/cm^2$), σ is the effective

absorption cross section (cm^2) of the Li_2(X-B) transition, hν is the

photon energy (20500/cm), and $1/\tau$ is the Li_2(B) decay rate due to both

radiative and collisional processes. Neglecting the collisional

effects, $1/\tau$ is shown in Appendix E to be 10^8/s. The product $\sigma[Li_2(X)]$

was experimentally determined in Chapter 2 to be .12/cm at 900°C.

Using these results in equation 1 yields $[Li_2(B)] \cong 3 \times 10^9/cm^3$ and

$[Li_2(B)]/[Li_2(X)] = 10^{-6}$ where the density of Li_2(X) corresponds to

the unperturbed equilibrium vapor pressure. Other terms in the rate

equation which account for reactive losses of Li_2(B) such as

collisions with Li atoms, will further suppress the excited dimer

density. The $[Li_2(B)]$ density estimate derived here is therefore an

upper limit which shows that the perturbation of the ground state due

to the optical excitation does not exceed one part in 10^6.
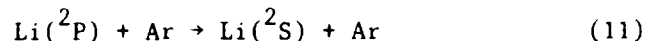
3. Reactions Involving Excited State Species

The excited Li_2(B) molecules produced by laser excitation may

transfer energy to or chemically react with other species as a result

of collisions. Such processes have been observed in both the Na/Na_2

and K/K_2 systems. In the Na/Na_2 system, Na_2(B) reacts with Na(^{2}S) to

produce Na_2(X) and Na(^{2}P).[48,49] Additionally, the reaction of Na_2(X)

with Na(^{2}P) has been shown to form Na(^{2}S) and Na_2 (a,A).[50] By

analogy, these same processes are postulated to occur in the Li/Li_2

system since the energy level structures and symmetries of the systems

are the same with one exception. As shown in Figure 22 the dissociative

$^3\Sigma$ state in Li_2 predissociates the a$^3\Pi$ state at very low vibrational

levels which does not happen in Na_2. Since predissociation rates are

much faster than collisional or radiative rates, processes involving

72

$Li_2(a^3\pi)$ as a reactant can be ignored in the Li/Li_2 system. The important reactions for the Li system are shown below.

Excitation:	$Li_2(X) + h\nu \rightarrow Li_2(B)$	(1)
Reaction:	$Li_2(B) + Li(^2S) \rightarrow Li_2(X) + Li(^2P)$	(2)
	$Li(^2P) + Li_2(X) \rightarrow Li_2(A,a) + Li(^2S)$	(3)
	$Li(^2P) + Li(^2S) \rightarrow Li(^2S) + Li(^2S)$	(4)
Radiation:	$Li_2(B) \rightarrow Li_2(X) + h\nu$	(5)
	$Li_2(B) \rightarrow Li_2(A) + h\nu$	(6)
	$Li_2(A) \rightarrow Li_2(X) + h\nu$	(7)
	$Li(^2P) \rightarrow Li(^2S) + h\nu$	(8)
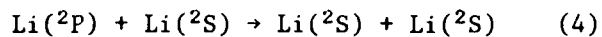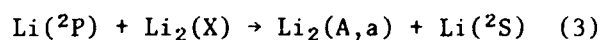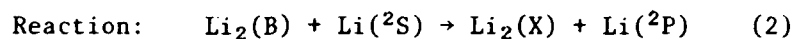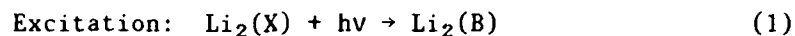
These reactions account for all the emissions that were observed in the fluorescence of Li vapor and reported in Chapter 2.

Since the experiments in this thesis were performed in an environment which included an inert gas, the inert gas deactivation reactions must also be considered in the specification of the kinetic model as shown below:

$$Li_2(B) + Ar \rightarrow Li_2(X) + Ar \qquad (9)$$

$$Li_2(A) + Ar \rightarrow Li_2(X) + Ar \qquad (10)$$

$$Li(^2P) + Ar \rightarrow Li(^2S) + Ar \qquad (11)$$
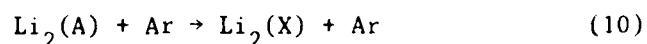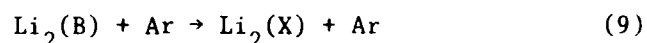
Electronic to translational energy conversion rates are generally small (10^{-13} to $10^{-16} cm^3/s$) and therefore these reactions should have a small effect on the overall kinetics.
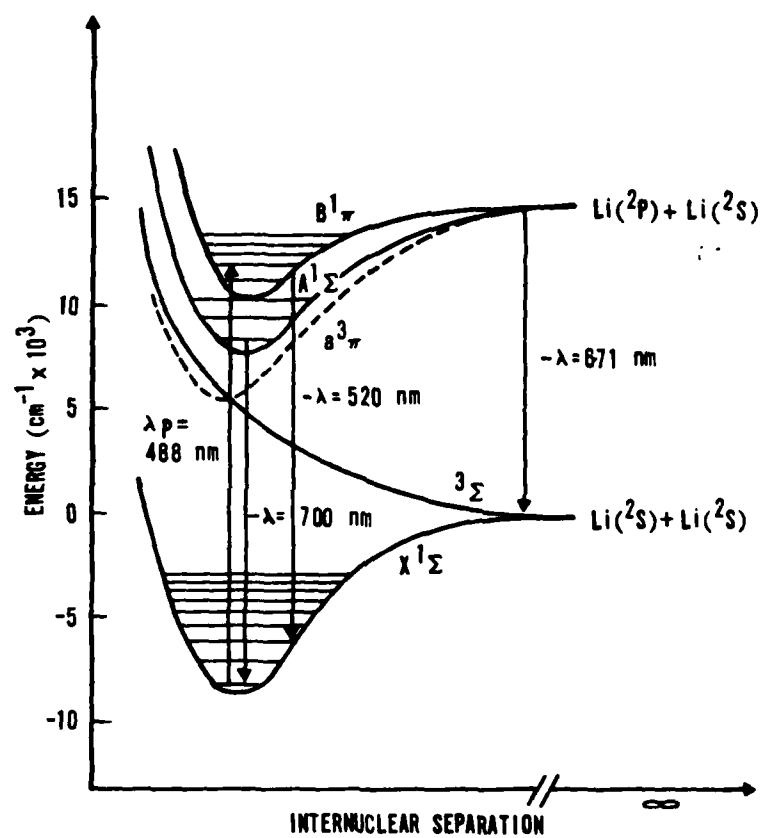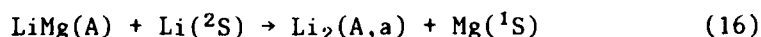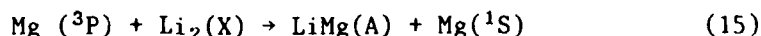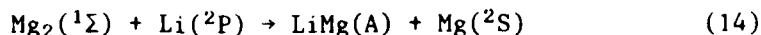
Figure 22 - Li$_2$ Potential Energy Curves

The model that has been developed for the Li system ignores reactions involving collisions of two excited states species to form a doubly excited species (energy pooling) and three body reactions, as does the previous work on K and Na which was conducted in the same density regimes as the experimental work in this thesis. There are several Li/Li_2 states accessible to energy pooling reactions of $Li_2(B)$, $Li_2(A)$ and $Li(^2P)$. None of these were observed in emission. This result is consistent with expectations in that gas kinetic formation rates ($10^{-10} cm^3/s$) limit the pooling reactions involving excited states species with densities of $10^9/cm^3$ - 10^{10} /cm^3 to form doubly excited states at rates of .1/s - 1/s while the rates for forming singly excited species are typically 10^5 - $10^7/s$.

Three body recombination reactions such as Li + Li* + M → Li_2 (A) + M are also ignored. At typical total pressures of 100 torr the three body rates are several orders of magnitude less than the corre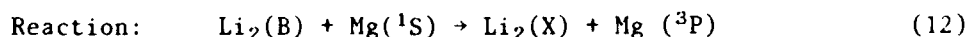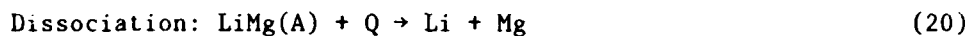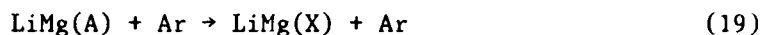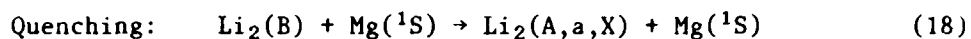sponding two body rates, since the product of a typical density ($10^{18}/cm^3$) and a typical three body rate of $10^{-32} cm^6/s$ is much less than the typical two body rate of $10^{-12} cm^3/s$ to $10^{-10} cm^3/s$.

The addition of Mg to an optically excited Li system, creates several other possible kinetic channels including those which form the excimer LiMg(A). The possible new reactions are listed below:

Reaction: $\qquad Li_2(B) + Mg(^1S) \rightarrow Li_2(X) + Mg\ (^3P)$ $\qquad\qquad$ (12)

$\qquad\qquad\qquad Li_2(B) + Mg(^1S) \rightarrow LiMg(A) + Li(^2S)$ $\qquad\qquad$ (13)

$\qquad\qquad\qquad Mg_2(^1\Sigma) + Li(^2P) \rightarrow LiMg(A) + Mg(^2S)$ $\qquad\qquad$ (14)

$\qquad\qquad\qquad Mg\ (^3P) + Li_2(X) \rightarrow LiMg(A) + Mg(^1S)$ $\qquad\qquad$ (15)

$\qquad\qquad\qquad LiMg(A) + Li(^2S) \rightarrow Li_2(A,a) + Mg(^1S)$ $\qquad\qquad$ (16)

Radiation: $\qquad LiMg(A) \rightarrow LiMg(X) + h\nu$ $\qquad\qquad\qquad\qquad$ (17)

Quenching: $Li_2(B) + Mg(^1S) \rightarrow Li_2(A,a,X) + Mg(^1S)$ (18)

$LiMg(A) + Ar \rightarrow LiMg(X) + Ar$ (19)

Dissociation: $LiMg(A) + Q \rightarrow Li + Mg$ (20)
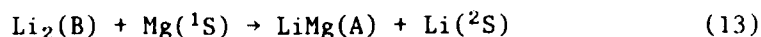
These reactions follow from consideration of reaction exoergicity, as well as the reaction correlation diagram shown in Figure 23. Several of the above reactions can be shown to be negligibly important in the specification of the LiMg kinetic model. Reaction (12), the production of $Mg(^3P)$ from collisions of Mg with $Li_2(B)$, is 3000/cm endothermic (kT is 815/cm at 900°C) and spin forbidden. Additionally, this reaction competes with the reaction forming the excimer (13) which is exothermic and spin allowed. Also, there was no observation of $Mg(^3P)$ emission in the experiments. For these reasons, reactions involving $Mg(^3P)$ (12,15) will be ignored. Reaction (14) involving formation of LiMg(A) by collisions of $Li(^2P)$ with $Mg_2(X^1\Sigma)$ can be similarly ignored, since the reaction is spin forbidden and the small densities of both $Li(^2P)$ and $Mg_2(X^1\Sigma)$ present will combine to make this reaction many orders of magnitude smaller than the reactions forming LiMg(A) by collisions of Mg with $Li_2(B)$ as shown below.

A steady state analysis of the production of $Li(^2P)$ through collisions of $Li(^2S)$ with $Li_2(B)$ yields the following expression for $Li(^2P)$:

$$[Li(^2P)] = [Li_2(B)][Li]K_f/A(Li)$$

where K_f is the formation rate and A(Li) is the radiation trapped decay rate. The maximum value of $[Li_2(B)]$ was previously determined to be $3 \times 10^9/cm^3$, [Li] is $9 \times 10^{16}/cm^3$ at 900°C from Table XVIII and A(Li) is $1 \times 10^6/s$ by analogy with Na. By assuming a gas kinetic formation rate of
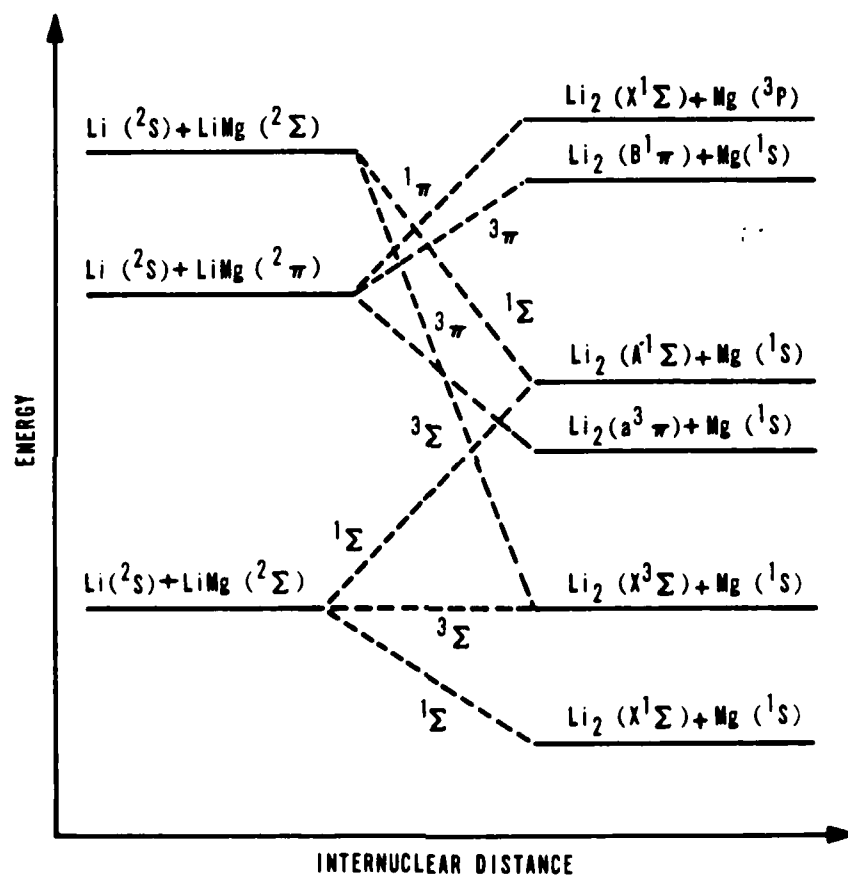
76

Figure 23 - LiMg Reaction Symmetries

10^{-10} cm^3/s, it is found that an upper limit to [Li(^{2}P)] is 3 x

10^{10}/cm^3 . With this information the relative formation rates of

LiMg(A) by reactions (13) and (14) can then be compared. Therefore

[Li(^{2}P)][Mg$_2$]K$_1$/[Li$_2$(B)][Mg]K$_2$ equals 10^{-5} assuming K$_1$ $\cong$ K$_2$.

Additionally reaction (14) should also produce LiMg(B) emission which

is not observed. Therefore reaction (14) will be ignored in the

remainder of the analysis.

Reaction (18), the direct quenching of Li$_2$(B) to Li$_2$(X) is

unlikely since there are no intermolecular curve crossings connecting

the states. Quenching of Li$_2$(B) to the a$^3\Pi$ state is spin forbidden.

Quenching to the A$^1\Pi$ state may be accomplished through curve crossings

in the triatomic formed in the collision of Li$_2$(B) with Mg. Since the

LiMg excited states lie intermediate to the Li$_2$(B) and Li$_2$(A) states

there is also a direct route along intermolecular curves by which

Li$_2$(B) can be converted in Li$_2$(A) as shown in Figure 16. This

reaction is therefore likely to have a significant rate in the LiMg

kinetic model.

Finally, the possibility of collisional dissociation of LiMg(A) -

reaction(20) must be considered. Since LiMg(A) is bound by only

4000/cm and has a lifetime of several μ seconds (Appendix E), at a

typical pressure of 100 torr it may undergo numerous collisions

(10^6 coll/torr-sec x 10^2 torr x 1μsec = 100 collisions) prior to

radiative decay. Since 5 consecutive energy addition collisions would

dissociate LiMg(A) for kT of 800/cm reaction (20) must be

considered. The same reactions are ignored for Li$_2$(B) and Li$_2$(A)

because their radiative lifetimes are two orders of magnitude shorter

than LiMg(A) which allows at most only one collision on the average

78

before radiation. If the lifetime of the LiMg(A) state is not determined by radiative decay but by reactive or collisional decay which significantly shortens the lifetime then the thermal dissociation process may be ignored in LiMg also.

As in the case of the mixed Li and Ar system, the effects of three body reactions were considered negligible. The experimental data shown in Figure 18 demonstrated that the LiMg(A) emission intensity increased with decreasing pressure in the range of 50-425 torr. If a three body reaction was responsible for the excimer formation, there would have been at least an initial increase in intensity with increasing pressure followed by a decrease when the inert gas quenching rate equaled the product of the third body density and the three body formation rate.

The possibility of energy pooling reactions in the Li/Mg system is also ignored for the same reasons as in the pure Li system; the production rates of doubly excited species are extremely small due to small $(10^8/cm^3 - 10^{10}/cm^3)$ excited state densities. Additionally there was no observation of emission from doubly excited species. Initially, the possibility existed that the LiMg emission occurred as a result of an energy pooling process. However, the linear power dependence of the emission intensity shown in Figure 17 contradicts this hypothesis since emission resulting from a species produced as a result of energy pooling would have shown a quadratic dependence on the laser power.

In addition to considering the reactions involved in the Li/Mg system, the effects of radiation trapping and diffusion need to be examined. In the thesis experiments, a cyclindrical volume of Li/Mg gas was excited along the axis by a laser beam. The emission from

79

this cylinder was viewed from a direction perpendicular to the axis. The emitted radiation therefore had to pass through several centimeters of the Li/Mg gas. The typical gas densities at 900°C were $10^{17}/cm^3$ Li, $10^{16}/cm^3$ Li_2 and $10^{18}/cm^3$ Mg. Since radiation trapping is known to have an important effect on atomic emitters at densities of $10^{13}/cm^3$ the Li(^{2}P-^{2}S) radiation was expected to be significantly radiation trapped. For the same transition in Na the trapped lifetime has been calculated to increase from a natural lifetime of 16nsec to a constant value of 10μsec over the pressure range of .1 - 10 torr.[50] In this same temperature range, Na_2 radiation is not significantly radiation trapped since the dimer density is 20-100 times lower than the atomic density and the number of potential absorbers per unit frequency is substantially decreased due to rotational and vibrational dilutions. These same assumptions will be applied to the Li/Mg system. The lifetimes of molecular emitters will be assumed unperturbed by radiation trapping while the trapped lifetime of Li(^{2}P) will be measured in the experiments.

It has been shown that optical pumping in the Li/Li_2 system does not significantly perturb the concentration of Li_2. However, when Mg is present an additional complication occurs. Whereas in a pure Li system the optically excited Li_2(B) molecules eventually decay back to Li_2(X), with Mg present the dimers may be dissociated due to the excimer formation reactions. Therefore in steady state in the optically pumped region the dimer concentration may be suppressed to the point where three body recombination and diffusion balance the loss of dimers caused by excimer formation. Since diffusion and recombination are normally slow processes there is a possibility that the Li_2 concentration will be substantially depressed. Figure 13 demonstrated

80

that experimentally this was not observed. It is difficult to analyze this problem a priori since the rate of dimer loss due to excimer formation is not known and it is difficult to assess the effects of reactions (1) and (2) which tend to enhance the rate of formation of Li_2 in addition to suppressing Mg_2.

Radial diffusion of ground state species is negligible since the ground state density gradients are small as was previously shown. The excited species density gradients however are much larger and since they are produced in the center region they will diffuse out. However, the short lifetimes of these species (10^{-6}s - 10^{-8}s) will prevent them from diffusing very far before radiative decay. Assuming a hard sphere model the diffusion rate D is just $\bar{v}/2[N]\pi r^2$ where $\bar{v}$ is the thermal velocity $\bar{v} = \sqrt{2kT/m}$, [N] is the number density and r the species radius. Using typical values for the 100 torr, 900°C regime D = 1 cm^2/s. An excited state species with a lifetime of $\tau < 10^{-6}$ sec diffuses typically $\sqrt{D\tau}=10^{-3}$cm prior to decay. Therefore since the laser beam is typically 10^{-1}cm in diameter diffusive loss of the excited species can be ignored.

The following figures summarize the important features of the LiMg kinetic model. Figure 24 shows the energy flow in an optically excited Li/Mg system. Figure 25 summarizes the important reactions. The approximations that have been made in defining the model are listed in Figure 26. The rate equations corresponding to the reactions listed in Figure 25 are summarized in Figure 27.

4. Steady State Analysis

Using the rate equations from Figure 20 steady state solutions were determined for the various excited state emitters for the cases

of a pure Li system and a mixed Li/Mg system as shown in Figure 21. In these so' ions the ground state species densities are assumed to be the equilibrium concentrations specified by the temperature. These solutions will be related to the results of experiments where the relative emission intensities of $Li_2(A)$, $Li_2(B)$ were measured in pure Li and mixed Li/Mg systems. The measured intensity ratios were used to infer the equivalent concentration ratios. Using this experimental data several of the rate constants in the equations in Figure 21 were determined.
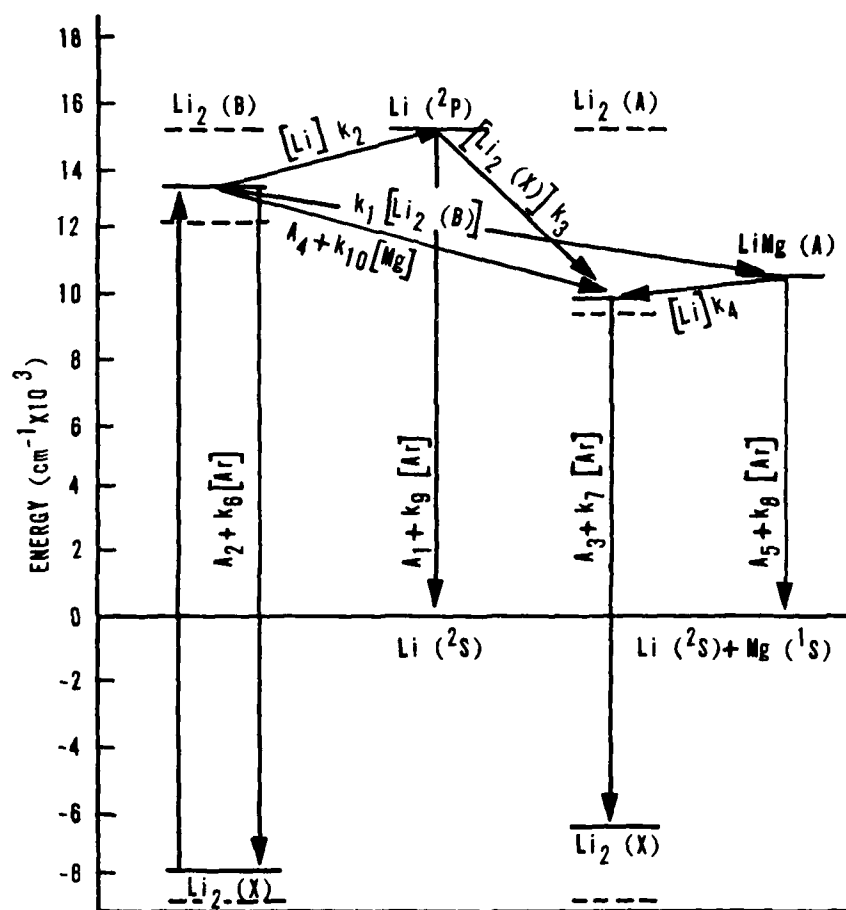
Figure 24 - LiMg System Energy Flow

Reaction	Rate Constant Designation	Literature Value

A. Excitation

$Li_2(X)+h\upsilon \rightarrow Li_2(B)$

B. Primary

$Li_2(B)+Mg \rightarrow LiMg(A)+Li$	$K_1(cm^3/s)$	None
$Li_2(B)+Li \rightarrow Li_2(X)+Li(^2P)$	$K_2(cm^3/s)$	(2×10^{-9})*

C. Secondary

$Li(^2P)+Li_2(X) \rightarrow Li_2(A,a)+Li$	$K_3(cm^3/s)$	(3.4×10^{-9})*
$LiMg(A)+Li \rightarrow Li_2(A,a)+Mg$	$K_4(cm^3/s)$	None
$LiMg(A)+Ar \rightarrow Li(^2P)+Mg+Ar$	$K_5(cm^3/s)$	None

D. Radiation

$Li(^2P) \rightarrow Li+h\upsilon$	$A_1(1/s)$	3.72×10^7
$Li_2(B) \rightarrow Li_2(X)+h\upsilon$	$A_2(1/s)$	1×10^8 (Appendix E)
$Li_2(A) \rightarrow Li_2(X)+h\upsilon$	$A_3(1/s)$	5.56×10^7
$Li_2(B) \rightarrow Li_2(A)+h\upsilon$	$A_4(1/s)$	1×10^7 (Appendix E)
$LiMg(A) \rightarrow LiMg+h\upsilon$	$A_5(1/s)$	1.1×10^6 (Appendix G)

E. Quenching

$Li_2(B)+Ar \rightarrow Li_2(X)+Ar$	K_6	None
$Li_2(A)+Ar \rightarrow Li_2(X)+Ar$	K_7	None
$LiMg(A)+Ar \rightarrow LiMg(X)+Ar$	K_8	None
$Li(^2P)+Ar,Li \rightarrow Li+Ar,Li$	K_9	None
$Li_2(B)+Mg \rightarrow Li_2(A)+Mg$	K_{10}	None

*Na System Rates

Figure 25 - LiMg Reactions

END
DATE
FILMED
10-82
DTIC

1. Ground State Densities Li, Li_2, Mg are Unperturbed by:

    a) Li-Mg Interactions

    b) Laser Interactions

2. Pooling Reactions are Insignificant

3. Three Body Reactions are Insignificant

4. Li/Li_2 Kinetics are Analogous to Na/Na_2 Kinetics

5. Endothermic Reactions Considered Insignificant

6. Diffusive Effects are Unimportant

7. Radiation Trapping Affects Only Atomic Emitters

8. Mg_2, $Li_2(a)$ Reactions Insignificant

Figure 26 - List of Assumptions

I. $d[Li_2(A)]/dt = [Li(^2P)][Li_2(X)]K_3 + [LiMg(A)][Li]K_4$
$$+ [Li_2(B)]A_4 - [Li_2(A)](A_3 + K_7[Ar])$$

II. $d[Li_2(B)]/dt = I\sigma[Li_2(X)]/h\nu - [Li_2(B)](A_2 + A_4 + K_1[Mg]$
$$+ K_2[Li] + K_6[Ar])$$

III. $d[Li(^2P)]/dt = [Li_2(B)][Li]K_2 - [Li(^2P)]([Li_2(X)]K_3 + A_1$
$$+ [Ar]K_9) + [LiMg(A)]K_5[Ar]$$

IV. $d[LiMg(A)]/dt = [Li_2(B)][Mg]K_1 - [LiMg(A)]([Li]K_4 + A_5$
$$+ [Ar](K_8 + K_5)$$

Figure 27 - LiMg System Excited State Rate Equations

1. Pure Li Case:

   I. $[Li_2(A)] = ([Li(^2P)][Li_2(X)]K_3 + [Li_2(B)A_4]/A_{K3}$

   $A_{K3} = A_3 + K_7[Ar]$

   II. $[Li_2(B)] = ((I\sigma/h\nu)[Li_2(X)])/A_{K2}$

   $A_{K2} = A_2 + A_4 + K_2[Li] + K_6[Ar]$

   III. $[Li(^2P)] = ([Li_2(B)][Li]K_2)/A_{K1}$

   $A_{K1} = A_1 + [Li_2(X)]K_3 + [Ar]K_9$

2. Li/Mg Case

   I. $[Li_2(A)] = [Li_2(A)]_{No\ Mg}$
   $$+ ([Li_2(B)[Mg]K_{10} + [LiMg(A)][Li]K_{4a})/A_{K3}$$

   II. $[Li_2(B)] = (I\sigma/h\nu)[Li_2(X)]/(A_{K2} + (K_1 + K_{10})[Mg])$

   III. $[Li(^2P)] = [Li_2(B)][Li]K_2/(A_{K1} + [LiMg(A)][Ar]K_5)$

   IV. $[LiMg(A)] = [Li_2(B)][Mg]K_1/A_{K5}$

   $A_{K5} = A_5 + [Li]K_4 + [Ar](K_8 + K_5)$

Figure 28 - Steady State Solutions to Excited State Rate Equations

5. Time Dependent Analysis of Li/Mg Kinetic System

If _ laser excitation source which produces $Li_2(B)$ is modulated at a frequency ω then the resulting products of the excitation will also exhibit a similar periodic time dependent behavior. Since the reaction products in the system are formed through collisional processes and decay by both radiative and collisional processes taking finite amounts of time, the system response will lag the excitation. These time lags or phase shifts can be measured and related to kinetic and radiative rates. The technique of time delay or phase shift measurement has been used extensively for the determination of the lifetimes of excited states.[55-58] In many cases of experimental interest a simple relationship exists for the phase shift ϕ of the emitter relative to the exciter: $\tan\phi = \omega\tau$ where ω is the modulation frequency and τ the excited state lifetime. In general, however, the response of a kinetic system involving many kinetically active species will not be as simple. In fact, it may be too complex to be of use in determining kinetic rates except in certain limiting cases wich simplify the input/output relationship. The simplest case occurs when the excitation or perturbations are sufficiently small that the system responds in a linear fashion. In order to justify the use of linear response or small signal theory to characterize the response of the LiMg system, it is necessary to establish that the magnitude of the nonlinear terms in the rate equation are small when compared to the magnitude of the corresponding linear terms.

The previous analysis and experimental measurements of the Li/Mg system have demonstrated that many of the nonlinear processes are unimportant in modeling the LiMg system. Experimentally the absorption

88

of laser power was observed to be linear in laser intensity both with
and without Mg present. Additionally the LiMg emission intensity
showed a linear dependence on laser power. Further, the analysis in
the previous several sections supported these experimental
observations and also showed that the nonlinear processes of
diffusion, energy pooling, and three body reactions can be ignored.
However, even with the elimination of these processes, there remain
certain nonlinear terms in the rate equations shown in Figure 27. The
nonlinearities arise from terms which contain products of excited
state and ground state densities as well as products of ground state
densities and the laser intensity. The ground state(G), excited
state(E), and laser intensity(I) terms are all functions of time that
have a constant term and a time varying part as shown below. The
magnitude of the time varying portions are always less than the
constant terms since G,E and I are positive definite quantities.

$$G(t) = G_0 + \Delta G(t)$$

$$E(t) = E_0 + \Delta E(t)$$

$$I(t) = I_0 + \Delta I(t)$$

The nonlinear terms in the rate equations which arise from products of
these expressions are $\Delta G(t)\Delta E(t)$ and $\Delta G(t)\Delta I(t)$. Analysis in the
previous sections has shown that typically $\Delta G/G_0$ was approximately 10^{-7}
and ΔG is approximately equal ΔE. Since the laser was at least 70%
modulated $\Delta I \sim I_0$. Therefore, all terms such as $\Delta G(t)\Delta E(t)$ and
$\Delta G(t)\Delta I(t)$ are always small compared to terms like $\Delta E(t)G_0$ and
$\Delta I(t)G_0$. The constant terms G_0E_0, etc., were excluded experimentally
by accepting only the time varying portion of the output. The cross
terms $\Delta G(t)E_0$ and $\Delta G(t)I_0$ can also be excluded when compared to terms

like $\Delta E(t)G_0$ or $\Delta I(t)G_0$ since $\Delta E(t)/E_0$ and $\Delta I(t)/I_0 \cong 1$ and $G_0 >> E_0$.

Applying these concepts to the rate equations in Figure 20 simplifies the nonlinear differential equations to a series of coupled linear differential equations. If each species density and the laser intensity is then expanded in a Fourier series and is substituted into the rate equations, the differential equations are reduced to complex algebraic expressions. This method of solution is applicable because of the superposition principle which applies to linear systems and the orthogonality of the basis functions which make up the Fourier expansion. Then examining only those terms at the fundamental frequency, applying the previous analysis regarding elimination of negligibly small terms and using the Euler identity, an expression for the phase shift ϕ can be obtained. In the case where the system is first order then the simple result $\tan \phi = \omega\tau$ is obtained where τ represents the lifetime of an excited state. These procedures can further be clarified by using the $Li_2(B)$ rate equation as an example.

The rate equation for $Li_2(B)$ can be solved by Fourier transformation of the periodically modulated laser and all the species densities as shown below:

$$I(t) = I_o + I_1 e^{i(\omega t)} + \ldots$$

$$[Li_2(B)] = [Li_2(B)]_o + [Li_2(B)]_1 \, e^{i(\omega t + \phi B)} + \cdots$$

$$[Li] = [Li]_o + [Li]_1 \, e^{i(\omega t + \phi L)} + \cdots$$

$$[Li_2(X)] = [Li_2(X)]_o + [Li_2(X)]_1 \, e^{i(\omega t + \phi X)} + \cdots$$

The phase of the laser is arbitrarily set to zero while all other phases are defined to be phases relative to the laser. All the

coefficients are real time independent quantities. By excluding the nonlinear terms, cancelling $e^{i\omega t}$ in each term, and keeping only the terms at frequency ω, as previously discussed, the rate equation for the $Li_2(B)$ density converts to an algebraic expression:

$$
\begin{aligned}
i\omega \, [Li_2(B)]_1 e^{i(\phi B)} = {} & I_0(\sigma/h\nu) \, [Li_2(X)]_1 e^{i(\phi X)} \\
& + I_1(\sigma/h\nu)[Li_2(X)]_0 e^{i(\phi La)} + [Li_2(B)]_1 \\
& (A_2 + A_4 + K_2 \, [Li]_0 + K_6 \, [Ar]o)e^{i(\phi B)} \\
& + [Li_2(B)]_0 \, [Li]_1 K_2 e^{i(\phi L)}
\end{aligned}
$$

The term $I_0[Li_2(X)]_1 \ll I_1[Li_2(X)]_0$ for the case of nearly complete modulation and small ground state perturbations since $[Li_2]_1/[Li_2]_0 \sim 10^{-6}$. Also the term $[Li_2(B)]_0[Li]_1 \ll [Li_2(B)]_1 \, [Li]_0$ since $[Li_2(B)]_0 \cong [Li_2(B)]_1$ for nearly complete modulation and $[Li]/[Li]_0 < 10^{-4}$ based on the previous steady state analysis which showed that $[Li^*]/[Li] \cong 10^{-4}$. By eliminating these negligibly small terms it is seen that:

$$
(i\omega + A_2 + K_2[Li]_0 + K_6[Ar]_0)[Li_2(B)]_1 e^{i\phi B} = I_1 \sigma/h\nu[Li_2(X)]o
$$

which reduces to

$$
\tan \phi_B \; = \; \omega/(A_2 + A_4 + K_2 \, [Li]_0 + K_6[Ar]_0)
$$

by use of the Euler identity.

Although this analysis is somewhat more complicated than for collisionally unperturbed emission, the results are nonetheless of the

same form; $\tan \phi = \omega \tau$ where $1/\tau = A_2 + A_4 + K_2[Li]_o + K_6[Ar]_o$. Here τ is easily recognized as the kinetically controlled lifetime of $Li_2(B)$ due to both radiative decay and collisional losses of the excited state. The results of the phase shift experiments can therefore be analyzed in the standard Stern-Vollmer form where $1/\tau$ or $\omega/\tan \phi$ is plotted versus pressure or species densities. The Stern-Vollmer intercept is then the radiative decay rate in the absence of collisions and the slope of the line is the rate constant for collisional loss of the excited state species.

The derivations of the phase shift expressions for the other excited species present in the Li only and Li/Mg systems are presented in Appendix F and summarized in Figure 30. For simplicity of presentation the "kinetic decay rates" A_{K1} through A_{K5} have been used in the equations for the phase shifts and are separately defined. In all of the derivations the same previously defined assumptions are used. The expressions for the phase shifts between $Li_2(B)$ and $Li(^2P)$ as well as $Li_2(B)$ and $LiMg(A)$ yield the same form as above. The expression for the phase of $Li_2(B)$ relative to $Li_2(A)$ is much more complicated due to the existence of multiple formation processes involving several excited state species each having a unique phase relationship with the laser (i.e. second order kinetics).

I. $Li_2(B) - Li(^2P)$ Phase Shift No Mg:

$$\omega / \tan\phi_1 = A_{K1}$$

$$A_{K1} \equiv A_1 + [Li_2(X)]K_3 + [Ar]K_9$$

II. $Li_2(B) - Li_2(A)$ Phase Shift No Mg:

$$\omega / \tan\phi_3 = (A_{K3}A_4 + (A_{K3}A_{K1}+\omega^2)\Delta)/(A_4 + (A_{K1}+A_{K3})\Delta)$$

$$A_{K3} \equiv A_3 + [Ar]K_7$$

III. $Li_2(B) - LiMg(A)$ Phase Shift:

$$\omega / \tan\phi_5 = A_{K5}$$

$$A_{K5} \equiv A_5 + [Li]K_4 + [Ar](K_5 + K_8)$$

Figure 30 - Li/LiMg Phase Shift Expressions

C. Experimental Configuration

1. $\;$ _teady State Efficiency Measurements

Measurements were made of the effect on emission of addition of Mg to a heatpipe containing just Li when excited by an Ar ion laser. Changes in emission intensity from the Li_2(B-X) and Li_2(A-X) transitions were interpreted as resulting from kinetic processes involving Mg. Additionally, by comparing the change in Li_2(B) emission upon Mg addition with the appearance of LiMg* emission the efficiency of excimer production was determined.

The experiments were performed using the same configuration as for the initial laser chemiluminescence studies described in Chapter 2. Emission spectra were recorded from 450nm to 1100nm with only Li present and with both Li and Mg present. A bandpass filter was used to exclude the second order Li_2(B) emission which obscured the LiMg emission in the region of 940nm-1000nm. The areas under the emission curves were then integrated after correcting for variations in the detector sensitivity over the wavelength range, as well as the bandpass filter response. The relative intensities and changes in the intensities of both LiMg* and Li_2(B) were then used with the steady state equations from Figure 28 to relate various kinetic rates.

2. Phase Shift Measurements

Time delays (or phase shifts) of one optical signal relative to another were recorded at various frequencies and various species number densities(temperatures). As an example, the phase delay of the LiMg emission relative to the Li_2(B) emission was measured and related via the phase shift equations shown in Figure 30 to the LiMg decay rate.

The phase shift experiments were performed using a slight modification of the laser chemiluminescence experimental configuration shown in Figure 11. The mechanical chopper was replaced by an electro-optic modulator which could be operated at frequencies between 10KHz and 1MHz. Additionally, a high frequency lockin amplifier was required to extend the operating range to 1MHz. Since according to $\tan\phi = \omega\tau$ it is expected that a phase shift of .35° will be obtained at a modulation frequency of 100KHz for $\tau = 10$nsec, it is necessary to use higher modulation frequencies to study short lived species. In this series of experiments the phase relationships between the laser, $Li_2(B)$, Li^*, $Li_2(A)$ and LiMg were measured both with and without Mg present at various species densities.

3. Intensity Measurements

An additional set of measurements were made where the intensity of $Li_2(B)$ fluorescence was recorded versus temperature in the absence of Mg. Since radiation trapping of $Li_2(B)$ is negligible and the absorption of the laser linearly tracks the $Li_2(X)$ concentration any deviation from proportionality between fluorescence intensity versus temperature and the vapor pressure curves must represent collisional deactivation of $Li_2(B)$ by Li atoms. The experiment was performed in the same configuration as shown in Figure 11 where instead of covering the entire spectral range, only the $Li_2(B)$ intensity as a function of temperature was monitored.

D. Results and Analysis

1. Introduction

The previously developed steady state rate equations were used to interpret the experimentally determined steady state efficiency, phase shift and intensity data. The results were interpreted for two separate cases: Li alone present and Li present in combination with Mg. The Li only case is analyzed first, since the rate constants determined for this case provide essential inputs to the interpretation of the combined Li/Mg system. Because of the complexity of the analysis extensive use is made of appendices for discussion of ancillary issues.

2. Li Only System

a. Determination of K_3 - $Li_2(X) + Li(^2P) \rightarrow Li_2(A) + Li(^2S)$ $Li(^2S)$

Figure 31 shows a Stern Vollmer plot derived from the $Li_2(B)$ - $Li(^2P)$ phase shift data where the data was related to the equation

$$\omega/\tan\phi = A_1 + [Ar]K_9 + [Li_2(X)]K_3$$

Each data point is an average of nine individual points; three each at 100KHz, 150KHz, and 200KHz. The error bars show one standard deviation of the data. Since during the course of the experiments the Ar density was held constant and only the $Li_2(X)$ density was varied, the slope of the curve can only be attributed to rate constant K_3, the rate of production of $Li_2(A)$ from collisions of $Li_2(X)$ with $Li(^2P)$, equal 6.5 x $10^{-10} cm^3/s$. The intercept is the sum of the remaining two constant terms. The intercept was, therefore, used to establish an upper limit to the rate constant $K_9 < 5$ x $10^{-13} cm^3/s$. Correspondingly

96

if the quenching term is considered negligible then an upper bound of 2μ sec is obtained for the radiation trapped lifetime. This is in reasonable agreement with the value of 10μ sec obtained for the Na system.[48]

    b. Determination of K_2 - $Li_2(B)$ + $Li(^2S)$ → $Li_2(X)$ + $Li(^2P)$

    A determination of K_2 was obtained from measurements of the phase shift between $Li_2(B)$ and $Li_2(A)$ at $850^{\circ}C$ and $895^{\circ}C$. The data is shown in Table 18.

$T(^{\circ}C)$	$\omega/\tan \phi$
850	$3.1 \pm .9 \times 10^6$
895	$6.8 \pm .3 \times 10^6$

Table 18 - $Li_2(B)$ - $Li_2(A)$ Phase Shift (No Mg) Phase Shift

Again each entry for $\omega/\tan\phi$ was an average of 9 values; 3 each taken at 100KHz, 150KHz, and 200KHz. The uncertainties shown are the standard deviations of the data. The data were related to the expression shown below as described in Appendix F, section II.

$$\tan\phi_3/\omega = (A_4 + (A_{K1} + A_{K3})\Delta)/(A_{K3}A_4 + (A_{K3}A_{K1} + \omega^2)\Delta)$$

where
$$\Delta \equiv [Li_2(X)]_0 K_3 [Li]_0 K_2/(\omega^2 + A_{K1}^2)$$

Rate constant K_2 was determined to be $2.7 \pm 1.5 \times 10^{-10}$ cm^3/s over the range of $850^{\circ}C$ - $895^{\circ}C$.

    A second determination of K_2 was made from the results of the experiments where $Li_2(B)$ fluorescence intensity was recorded as a
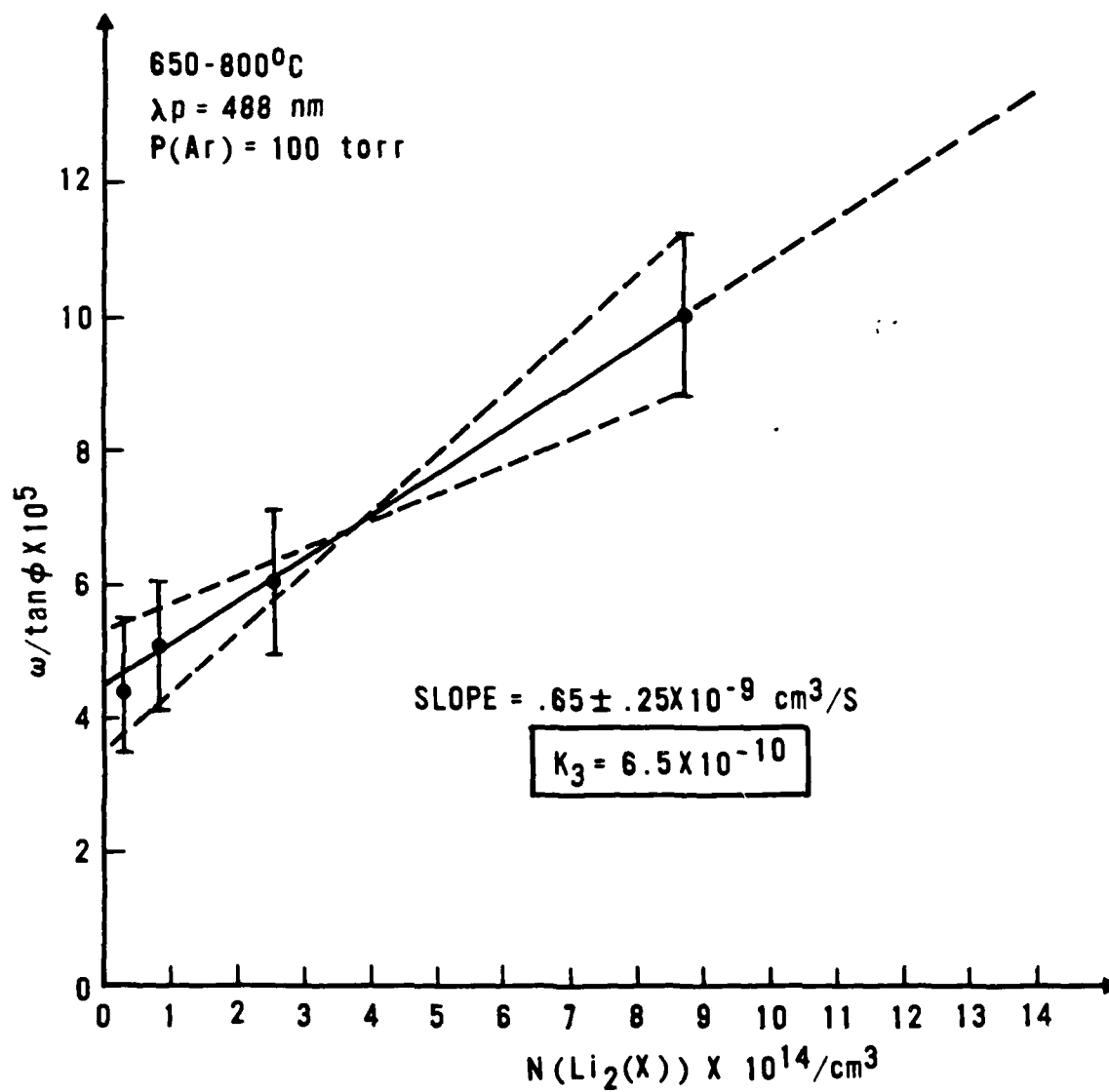
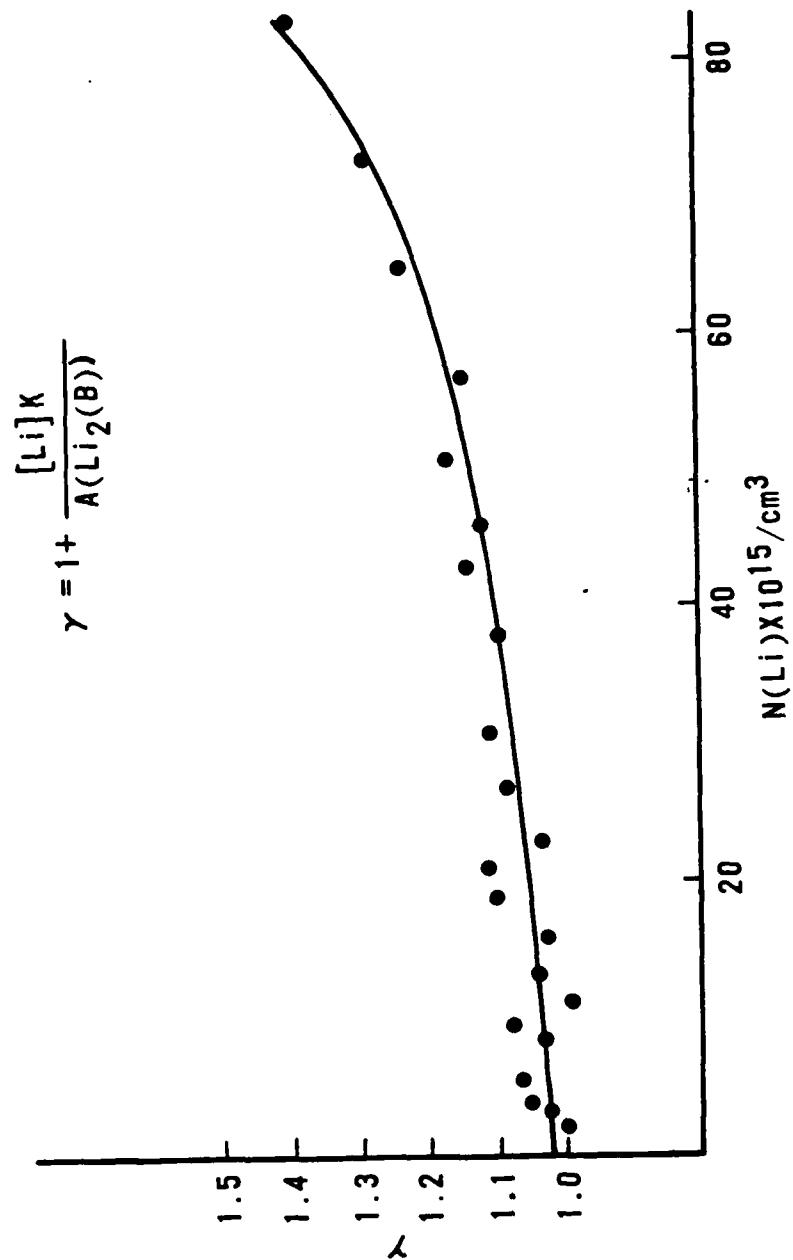Figure 31 - Li(^{2}P) - Li$_2$(B) Phase Shift Data

$$\gamma = 1 + \frac{[Li]K}{A(Li_2(B))}$$

Figure 32 - Li$_2$(B) Emission Intensity Versus Wavelength

function of temperature as shown in Figure 32. The data is related to the expression shown below as derived from the steady rate equations in Appendix H:

$$\gamma = 1 + K_2 \, [Li]/A_2$$

where γ is the ratio of the recorded $Li_2(B)$ emission intensities at temperatures T_i and T_o times the ratio of $[Li_2(X)]$ at temperatures T_o and T_i: $\gamma \equiv ([Li_2(B)]_{Ti}/[Li_2(B)]_{To}) \times ([Li_2(X)]_{To}/[Li_2(X)]_{Ti})$. In the absence of collisions therefore $\gamma = 1$. With the experimental values of γ, the values of $[Li]$ and $[Li_2(X)]$ at a given temperature from Appendix B, and the $Li_2(B)$ A coefficient from Appendix E, an average value of K_2 over the temperature range of the data was determined as shown in Appendix H. K_2 (the rate of deactivation of $Li_2(B)$ by Li) was determined to be $4.3 \pm 1.5 \times 10^{-10}$ cm^3/s over the temperature range of 800°C - 9. °C.

The values of rate constant K_2 obtained from two different experiments were within experimental uncertainties. However both analyses required the use of estimates for unknown physical parameters. The intensity data analysis used the estimated value of the $Li_2(B)$ A coefficient from Appendix E. The phase shift analysis required rate constant K_3 which was previously determined as well as the estimated $Li_2(B-A)$ radiative rate also from Appendix E. The value of K_2 used in future analysis will be the intermediate value of the two measurements: $K_2 = 3.5 \pm 2.1 \times 10^{-10} cm^3/s$.

The rate constants determined for the Li only system are summarized in Table 19. Utilizing the values of rate constants K_2 and K_3 expressions can be developed for the kinetic lifetimes of $Li(^2P)$ and $Li_2(B)$, A_{K2} and A_{K1} respectively by using the algebraic

100

expressions as given in Figure 25. The rates that were determined for the Li/Li$_2$ system were of the same order of magnitude as those for the Na/Na$_2$ system. This result which was expected lends confidence to the experimental approach that has been employed to determine the kinetic rates.

Table 19 - Li System Kinetic Rates

$K_2 = 3.5 \pm 2.1 \times 10^{-10}$ (cm^3/s)

$K_3 = 6.5 \pm 2.5 \times 10^{-10}$ cm^3/s)

$K_9 < 5 \times 10^{-13}$ cm^3/s)

A_1(Radiation Trapped) $< 2\mu$ sec

$A_{K1} = 4.5 \times 10^5 + [Li_2(X)]\ 6.5 \times 10^{-10}$ (1/s)

$A_{K2} = 1.0 \times 10^8 + [Li]\ 3.5 \times 10^{-10}$ (1/s)

3. Li/Mg System

The majority of the Li/Mg system rate constants were derived from measurements of the efficiency of light production experiments. A summary of these results are shown in Table 20. All of the efficiency measurements were made at a temperature of 890°C with 100 torr of Ar present using one watt of 488 nm Ar ion laser light for excitation. The integrated emission intensities of Li$_2$(B), Li$_2$(A) and LiMg(A) were determined both with and without Mg present. The recorded intensities were corrected for wavelength dependent detector and filter responses. The ratios of the integrated intensities of the various emissions are recorded in Table 20.

Table 20 - Intensity Ratios

$T = 890°C$, $P(Ar) = 100torr$, $\lambda = 488nm$

I.   Li Only

  a. $Li_2(A)/Li_2(B) = .52$

II. Li + Mg

  a. $Li_2(A)/Li_2(B) = .63$

  b. $LiMg/Li_2(B) = .09$

  c. $LiMg/Li_2(A) = .14$

III. Changes in Intensity

  a. $Li_2(B)$ with $Mg/Li_2(B)$ without $Mg = .35$

  b. $Li_2(A)$ with $Mg/Li_2(A)$ without $Mg = .42$

IV. LiMg Conversion Efficiency

  $LiMg/(Li_2(B)$ without $Mg - Li_2(B)$ with $Mg) = .048$

  a. Determination of $K_1 + K_{10} - Li_2(B) + Mg \rightarrow LiMg(A) + Li$

  $\rightarrow Li_2(A) + Mg$
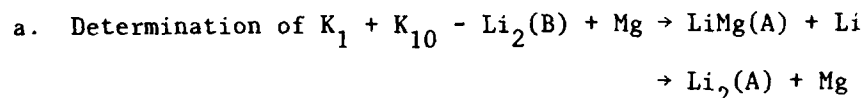
The total rate of deactiviation of $Li_2(B)$ by collision with Mg

atoms was determined from the data in Table 20. According to the

kinetics model Mg may either quench $Li_2(B)$ to $Li_2(A)$ (K_{10}) or react to

form $LiMg(A)$ (K_1). Experimentally, a 65% reduction of $Li_2(B)$ emission

was measured after the addition of Mg, which is indicative of the fact

that the Mg deactivation by collision is two times faster than

radiative decay. This experimental result can be related to the

steady state equations for $Li_2(B)$ with and without Mg present. The

ratio of the two steady state equations taken from Figure 21 is shown

below. The subscripts P and M refer to the pure Li case and the mixed
Li + Mg case respectively.

$$[Li_2(B)]_P/[Li_2(B)]_M = (A_{K2} + (K_1 + K_{10})Mg)/A_{K2}$$

By using the expression for A_{K2} from Table 19 together with the values
of $[Li_2] = 7.9 \times 10^{16}/cm^3$, $[Mg] = 8.1 \times 10^{17}/cm^3$ from Appendix B and
$[Li_2(B)]_P/[Li_2(B)]_M = 2.86$ from Table 20, then $(K_1 + K_{10})$ equal 2.9 ± 1
$\times 10^{-10} \, cm^3$.

b. Determination of K_4 - LiMg(A) + Li $\rightarrow$ Li_2(A,a) + Mg

In addition to measurements of the light conversion efficiency,
the phase shift between LiMg(A) and Li_2(B) was measured for
temperatures of $880^{\circ}C$ - $910^{\circ}C$. The results are shown in Table 21.
Each measurement is the mean of at least seven individual

Table 21 - LiMg Phase Shift Data

$\lambda = 488$ nm, $P(Ar) = 100$ torr

Temperature	$\omega/\tan\phi$
$880^{\circ}C \pm 3^{\circ}C$	$1.4 \pm .5 \times 10^7$
$900^{\circ}C \pm 3^{\circ}C$	$.5 \pm .2 \times 10^7$
$905^{\circ}C \pm 3^{\circ}C$	$.6 \pm .3 \times 10^7$
$910^{\circ}C \pm 3^{\circ}C$	$1.5 \pm .6 \times 10^7$
$900^{\circ}C \pm 10^{\circ}C$	$1.0 \pm .5 \times 10^7$

measurements spanning the frequency of 50 - 250 KHz. Because the
signal to noise ratio was not high, the data tends to have rather large

standard deviations.

The LiMg phase shift data can be related to the phase shift equation from Appendix F:

$$A_{K5} = \omega/\tan\phi 5 = A_5 + [Li]K_4 + [Ar](K_8 + K_5)$$

where A_5 is the LiMg* A coefficient, [Li] K_4 is the deactiviation rate from Li collisions with LiMg(A) and $(K_8 + K_5)$ are Ar deactivation rate constants. The sum of rate constants $K_8 + K_5$ is determined in Appendix H to be $< 2 \times 10^{-12}$ cm^3/s based on data from Chapter 2, Figure 19, where the LiMg emission intensity was measured as a function of Ar pressure. For 100 torr (8.3×10^{17}/cm^3) of Ar the term $[Ar](K_8 + K_5) < 1.6 \times 10^6$ which is negligible in comparison to the measured value for A_{K5} of 1×10^7. Therefore, the sum $A_5 + [Li]K_4$ is approximately 1×10^7/s. Since theoretically $A_5 \sim 1.3 \times 10^6$/sec as shown in Appendix E, its contribution to A_{K5} is also negligible. Therefore, A_{K5} reduces to a single term $[Li]K_4 = 10^7$/s, and thus $K_4 = 1.1 \pm .5 \times 10^{-10}$ cm^3/s. The last approximation will be further reinforced by showing that experimentally $A_5 \sim 4 \times 10^5$/sec.

c. Determination of K_{10} - $Li_2(B) + Mg \rightarrow Li_2(A) + Mg$

The efficiency experiment data in Table 20 shows that Mg interacts with $Li_2(B)$ in such a way as to produce an enhanced density of $Li_2(A)$, since the $Li_2(A)/Li_2(B)$ ratio is .52 without Mg and .63 with Mg. The kinetic model accounts for this result in two ways. Mg may directly quench $Li_2(B)$ to $Li_2(A)$ - (K_{10}) or Mg may react with $Li_2(B)$ producing the excimer LiMg(A) - (K_1) and then the excimer molecules may in turn collide with Li atoms producing $Li_2(A)$ - (K_{4a}).

104

An upper bound to K_{10} can be obtained by assuming $K_{4a}=0$ and by then comparing the $Li_2(A)$ steady state equations with and without the Mg terms. The resulting ratio is shown below where the pure Li case is subscripted P and the mixed Li/Mg case is subscripted M:

$$\frac{[Li_2(A)]_M}{[Li_2(A)]_P} = \frac{[Li(^2P)]_M[Li_2(X)]K_3 + [Li_2(B)]_M(A_4 + [Mg]K_{10})}{[Li(^2P)]_P[Li_2(X)]K_3 + [Li_2(B)]_P A_4}$$

Appendix I develops the relationship $[Li(^2P)] = 10[Li_2(B)]$. Making this substitution above and using the ratios $[Li_2(A)]_M/[Li_2(A)]_P = .42$, $[Li_2(B)]_M/[Li_2(B)]_P = .35$ from Table 20, $[Li_2(X)]$ and $[Mg]$ equal $4.1x10^{15}/cm^3$ and $8.1x10^{17}/cm^3$ at $890^{\circ}C$ respectively, A_4 equal $1x10^7$ from Appendix E and K_3 equal $6.5x10^{-10} cm^3/s$ from section 2.a, then $K_{10} < 9.1x10^{-12} cm^3/s$. Thus, the value of K_{10} is less than 3% of the sum of $K_1 + K_{10}$ as determined in section 3.a. Therefore, the calculation in this section substantiates that K_1 is the rate constant for the dominant $Li_2(B)$ deactivation process and is equal to 2.9×10^{-10} cm^3/s.

d. Determination of LiMg(A) A Coefficient - A_5

The value of A_5, the LiMg(A) A coefficient can be evaluated from a combination of the LiMg phase shift data and relative intensity data. The steady state rate equation for LiMg (Figure 21) can be rewritten as

$$[LiMg(A)]/[Li_2(B)] = [Mg]K_1/A_{K5}$$

The ratio on the left hand side of the equation is obtained from the

product of the integrated intensity ratio $I(LiMg(A))/I(Li_2(B)) = .09$

from Tab' 20 and the ratio of the $Li_2(B)$ and $LiMg(A)$ A coefficents

$(10^8/A_5)$. The right hand side can be evaluated since A_{K5} was

previously determined to be $1 \times 10^7/s$ from the phase shift data, $[Mg]$

at $890°C$ is $8.1 \times 10^{17}/cm^3$ from Appendix B. Now since $K_1 \gg K_{10}$ (i.e.

that the chemical reaction rate of Mg with $Li_2(B)$ is much larger than

the quenching rate) and $K_1 = 2.9 \pm 1 \times 10^{-10}$ cm^3/s, the resulting

value of $A_5 = 3.8 \times 10^5/s$. The radiative lifetime for $LiMg(A)$ is

therefore 2.6μ seconds. The experimentally obtained value of the LiMg

A coefficient is between the two theoretical values $1.3 \times 10^6/s$ for

the bound-free emission and $.2 \times 10^4/s$ for the bound-bound emission as

shown in Appendix E.

    e. Determination of K_{4a} (Formation of $Li_2(A)$ from LiMg)

            and K_{4b} (Formation of $Li_2(a)$ from LiMg)

If now it is assumed that all the additional $Li_2(A)$ emission that

occurs upon addition of Mg is due to reaction of Li with $LiMg(A)$ (K_{4a})

and the formation of $Li_2(A)$ due to the quenching reaction is

negligible $(K_{10}\cong 0)$, then an upper bound on K_{4a} can be determined from

the same $Li_2(A)$ data used above. As shown above:

$$\frac{[Li_2(A)]_M}{[Li_2(A)]_P} = \frac{[Li(^2P)]_M[Li_2(X)]K_3 + [LiMg(A)]\ [Li]K_{4a} + [Li_2(B)]_M A_4}{[Li(^2P)]_P[Li_2(X)]K_3 + [Li_2(B)]_P A_4}$$

and using the same values as before plus the ratio $[LiMg(A)]/[Li_2(B)]_1$

$= (.09)/(.35) \times (A_2/A_5) = 67.7$ from Table 20 and Appendix E, then K_{4a}

$< 4.8 \times 10^{-13}$ cm^3/s. The value of K_{4a} is thus found to be small

compared to the total value calculated for K_4 in section 3.b.

Therefore, $K_4 \cong K_{4b} = 1.1 \pm .5 \times 10^{-10}$ cm^3/s implies that the reaction of the excimers with Li atoms yield predominantly Li$_2$(a) rather than Li$_2$(A).

Finally, since the production of Li$_2$(A) may result from either direct quenching from the B state or reactions with LiMg and the balance of the two cannot be determined from the data, only upper bounds for the two rate constants K_{10} and K_{4a} can be determined.

A summary of the rates determined for the Li/Mg system is shown below:

$$K_1 = 2.9 \pm 1 \times 10^{-10} \text{cm}^3/\text{s}$$

$$K_{4a} < 4.8 \times 10^{-13} \text{ cm}^3/\text{s}$$

$$K_{4b} = 1.1 \pm .5 \times 10^{-10} \text{ cm}^3/\text{s}$$

$$A_5 = 3.8 \times 10^5/\text{s}$$

$$K_{10} < 9.1 \times 10^{-12} \text{ cm}^3/\text{s}$$

$$K_8 + K_5 < 1.3 \times 10^{-12} \text{ cm}^3/\text{s}$$

Figure 26 summarizes the specification of the LiMg model. Either a measurement has been made or an upper bound determined for every rate in the model.

Table 22 - LiMg Model Rate Measurements

Reaction	Rate Constant Designation	Specified Value

A. Excitation

$Li_2(X)+h\upsilon \rightarrow Li_2(B)$

B. Primary

Reaction	Rate Constant Designation	Specified Value
$Li_2(B)+Mg \rightarrow LiMg(A)+Li$	$K_1 (cm^3/s)$	$2.9\pm1 \times 10^{-10}$
$Li_2(B)+Li \rightarrow Li_2(X)+Li(^2P)$	$K_2 (cm^3/s)$	$3.5\pm2.5 \times 10^{-10}$

C. Secondary

Reaction	Rate Constant Designation	Specified Value
$Li(^2P)+Li_2(X) \rightarrow Li_2(A,a)+Li$	$K_3 (cm^3/s)$	$6.5\pm2.5 \times 10^{-10}$
$LiMg(A)+Li \rightarrow Li_2(A,a)+Mg$	$K_4 (cm^3/s)$	$<4.8 \times 10^{-13}; \ 1.1\pm.5 \times 10^{-10}$
$LiMg(A)+Ar \rightarrow Li(^2P)+Mg+Ar$	$K_5 (cm^3/s)$	$<2 \times 10^{-12}$

D. Radiation

Reaction	Rate Constant Designation	Specified Value
$Li(^2P) \rightarrow Li+h\nu$	$A_1 (1/s)$	3.72×10^7
$Li_2(B) \rightarrow Li_2(X)+h\nu$	$A_2 (1/s)$	1×10^8 (Appendix E)
$Li_2(A) \rightarrow Li_2(X)+h\nu$	$A_3 (1/s)$	5.56×10^7
$Li_2(B) \rightarrow Li_2(A)+h\nu$	$A_4 (1/s)$	1×10^7 (Appendix E)
$LiMg(A) \rightarrow LiMg+h\nu$	$A_5 (1/s)$	3.8×10^5

E. Quenching

Reaction	Rate Constant Designation	Specified Value
$Li_2(B)+Ar \rightarrow Li_2(X)+Ar$	K_6	$<3 \times 10^{-13}$
$Li_2(A)+Ar \rightarrow Li_2(X)+Ar$	K_7	$<10^{-11}$ (Assumed)
$LiMg(A)+Ar \rightarrow LiMg(X)+Ar$	K_8	$<2 \times 10^{-12}$
$Li(^2P)+Ar,Li \rightarrow Li+Ar,Li$	K_9	$<5 \times 10^{-13}$
$Li_2(B)+Mg \rightarrow Li_2(A)+Mg$	K_{10}	$<9.1 \times 10^{-12}$

Chapter IV - Summary, Conclusions and Recommendations

During the thesis work, two new diatomic species (LiMg and LiCa) were observed and characterized. Using laser induced chemiluminescence, a characteristic emission spectra was obtained. Ab initio calculations were used to construct a synthetic spectrum which was in good agreement with the experimental data. Additionally, the formation and decay kinetics for the LiMg system were examined theoretically and experimentally. It was concluded that LiMg was formed in an excited state as a result of reaction of excited $Li_2(B)$ with Mg atoms. The principle decay channels included reaction back to $Li_2(A)$ by collisions of the LiMg excimer with Li atoms and radiative decay.

Several additional experiments could be performed which would add to the body of knowledge of the Group IA/IIA excimers. Other combinations of IA/IIA metals could be studied in chemiluminescence experiments using experimental apparatus in which the two metal pressures could be varied independent of one another. A vapor pressure mismatch between Na and Ca appeared to be the major reason for not observing emission from the NaCa excimer. Additionally, the kinetics of the LiCa system could be studied. Finally, further experiments could be performed on the LiMg system. The reaction of $Mg(^3P)$ with $Li_2(X)$ resulting in LiMg(B) + Li could be studied and the data used to better characterize the LiMg potential energy curves. Also the potential of LiMg as an optically pumped laser candidate could be examined.

REFERENCES

1. Golde, M. F. and B. A. Thrush, Chem Phys Lett, 29 (1974) 486.

2. Ewing, J. J. and C. A. Brau, Phys Rev, A12 (1975) 129.

3. Ewing, J. J. and C. A. Brau, J. of Chem Phys, 63 (1975) 4640.

4. Tellinghuisen, Joel and A. K. Hays, J. of Chem Phys, 65 (1976) 4473.

5. Rhodes, Ch. K., Topics in Applied Physics: Excimer Lasers, Springer-Verlag, Berlin, 1979, pp. 7-13.

6. Ibid, pp. 23-25.

7. Ibid, pp. 28-29.

8. Liveing and Dewar, Proc Roy Soc, 27 (1898) 350.

9. Barat, S., Proc Roy Soc, A10 (1925) 194.

10. Benard, D. J., W. D. Slafer, and P. H. Lee, Chem Phys Lett, 43, (1976) 69.

11. Benard, D. J., P. J. Love, and W. D. Slafer, Chem Phys Lett, 48 (1977) 321.

12. Benard, D. J. and W. D. Slafer, Chem Phys Lett, 56 (1978) 438.

13. Herzberg, Gerhard, Molecular Spectra and Molecular Structure, I. Spectra of Diatomic Molecules, Van Nostrand, New York, 1950, pp. 318-319.

14. Moore, Charlotte E., Atomic Transition Probabilities, Volume I, NSRDS-NBS 35, Dec. 1971, p. 9.

15. Ibid, p. 107.

16. Ibid, p. 243.

17. Hirschfelder, Joseph O, Charles F. Curtis, and R. Byron Bird, Molecular Theory of Gases and Liquids, John Wiley and Sons, Inc., pp. 1064-1067.

18. Bates, D. R., Advances in Atomic and Molecular Physics, Volume 13, Academic Press.

19. Lacey, A. J., and W. B. Brown, Molecular Physics, 27 (1974) 1013.

20. Herzberg, Gerhard, Electronic Spectra and Electronic Structure of Polyatomic Molecules, Van Nostrand and Reinhold, New York, 1966, pp. 295-296.

21. Goodisman, Jerry, _Diatomic Interaction Potential Theory, Vol. I_, Academic Press, New York, 1973, pp. 19-22.

22. Harris, F. E. and H. H. Michels, Intern. J. Quantum Chemistry, S(1967) 329.

23. Michels. H. H., "Proposed Technical Program for the Energetics and Collision Dynamics of Electronic Transition Laser Systems," UTRC, 23 Jul 79, p. 11.

24. Neumann, D. K., D. J. Benard, and H. H. Michels, Chem Phys Lett, 73 (1980) 343.

25. _Ibid_.

26. _Ibid_.

27. Michels, H. H., Private Communication.

28. _Ibid_.

29. Herzberg, _Spectra of Diatomic Molecules_, Van Nostrand, New York, 1950, pp. 243, 247, 257.

30. Mies, Fredrick H., Molecular Physics, 26 (1973) 1233.

31. Michels, H. H., Private Communication.

32. Cooley, J. W., Math Computations, 15 (1961) 363.

33. Cashion, J. K., J. Chem Phys, 39 (1963) 1872.

34. Allison, A. C. and A. Dalgarno, At Data I (1969) 91.

35. Nesmeyanov, A. N., _Vapor Pressure of the Elements_, Academic Press, New York, 1963, pp. 127, 177, 181.

36. Vidal, C. R. and J. J. Cooper, Applied Physics, 40 (1969) 3370.

37. Hessel, M. M. and P. J. Jankowski, Applied Physics, 43 (1972) 219.

38. Barrow, Gordon M., _Physical Chemistry_, McGraw-Hill, New York, 1966, p. 614.

39. Barat, S., Proc Roy Soc, A10 (1925) 194.

40. Smith, D. P., Zeit Anorg Chem, 1907 Vol. 56, p. 109.

41. Matthewson, H., Zeit Anorg Chem, 1906 Vol. 48, p. 191.

42. Krauss, M., P. Maldonado, and A. Wahl, J. Chem Phys, 54 (1971) 4944.

43. Suchard, S. N., _Spectroscopic Constants for Selected Diatomic Molecules, Volume II_, SAMSO-TR-76-31, 16 Feb 76, pp. L-2 to L-14.

44. Rosen, B. Donnees, <u>Spectroscopiques Relatives Aux Molecules Diatomiques</u>, Pergammon Press, Oxford, 1970, pp. 242-243.

45. Moo. Charlotte E., <u>Atomic Energy Levels, Volume I</u>, NSRDS-NBS 35, Dec. 1971, p. 9.

46. Hessel, Merill M. and C. R. Vidal, J. Chem Phys, <u>70</u> (1979) 4439.

47. Miller, John C. and Lester Andrews, Applied Spectroscopy Reviews, <u>16</u> (1980) 8.

48. Kopeikina, E. K. and M. L. Yanson, Opt Spectrosc, <u>41</u> (1976) 217.

49. Kraulinya, E. K., E. K. Kopeikina, and M. L. Janson, Chem Phys Lett, <u>39</u> (1976) 565.

50. Lam, L. K., T. Fujimoto, A. C. Gallagher, and M. M. Hessel, J. Chem Phys, <u>68</u> (1978) 3553.

51. Nesmeyanov, A. N., <u>Vapor Pressure of the Elements</u>, Academic Press, New York, 1963, pp. 120-126, 175-179.

52. Balfour, W. E. and A. E. Douglas, Can J. of Physics, <u>48</u> (1970) 901.

53. Heer, C. V., <u>Statistical Mechanics, Kinetic Theory, and Stochastic Processes</u>, Academic Press, New York, 1972, p. 240.

54. Holstein, J., Phys Rev, <u>83</u> (1951) 1159.

55. Bailey, E. A., J. Chem Phys, <u>21</u> (1953) 1315.

56. Horiguchi, Hiroyuki, Bulletin of the Chemical Society of Japan, <u>50</u> (1977) 1657.

57. Hesser, James E., J. Chem Phys, <u>48</u> (1968) 2518.

58. Lawrence, G. M., J. Quantitative Spectroscopy and Radiative Transfer, <u>5</u> (1965) 359.

59. Ewing, C. T. and J. P. Stone, Nucl Sci, <u>20</u> (1966) 44.

60. Nesmeyanov, A. N., <u>Vapour Pressure of the Elements</u>, Academic Press, New York, 1963, p. 443.

61. Heer, C. V., <u>Statistical Mechanics, Kinetic Theory, and Stochastic Processes</u>, Academic Press, New York, 1972, p. 282.

62. <u>Ibid</u>, p.262.

63. <u>Ibid</u>, p. 240.

64. <u>Ibid</u>, p. 240; Eqn 7.42, p. 249; Eqns 7.55, 7.56, 7.58.

65. Rosen, B. Donees, <u>Spectroscopiques Relatives Aus Molecules Diatomiques</u>, Pergammon Press, Oxford, 1970, p. 242-243.

66. Michels, H. H., Private Communication.

67. Balfour, W. E. and A. E. Douglas, Can J. Of Physics, <u>48</u> (1970) 901.

68. Wine, Paul H. and L. A. Melton, Chem Phys Lett, <u>45</u> (1977) 509.

69. Ducas, Theodore W., et. al., J. of Chem Phys, <u>65</u> (1976) 842.

70. Baumgartner, G. and Demtroder W., Z. Physik, <u>232</u> (1970) 462.

71. <u>Ibid</u>, p. 470.

72. Tango, William J. and Richard N. Zare, J. of Chem Phys, <u>33</u> (1970) 3094.

Appendix A - Experimental Equipment

Equipment	Manufacturer & Model
GaAs Photomultiplier Tube	RCA C31004A
Housing & Cooler	Products for Research TE1777S
Ge Detector	Applied Detector Corp. #304
Scanning Monochromator	McPherson 2051
Low Frequency Lockin Amplifier	Princeton Applied Research 124A
High Frequency Lockin Amplifier	Princeton Applied Research 5202
Preamplifier	Princeton Applied Research 181
Chart Recorder	Hewlett Packard 9313
Chopper	Princeton Applied Research 125A
Electro-optic Modulator	Coherent Associates 317
Function Generator	Tektronix FG 504
Universal Counter	Tektronix DC 505A
White Light Source	Unknown
Ar Ion Laser	Coherent Radiation CR-8
CW Dye Laser	Coherent Radiation 590
Oscilloscope	Hewlett Packard 1744A
Power Meter	Scientech 362
Pulsed Dye Laser	Phase-R DL-2100B
High Frequency Preamplifier	Hewlett Packard 461A

Appendix B

The species number densities used in the kinetics calculations were determined utilizing data from Table II in Nesmeyanov[60] which supplied the fitting coefficients for Li_2, Li, Mg and Ca to the equation log $P = A - B/T + CT + D \log T$ as shown below. The calculated pressures were then converted to number densities $(1/cm^3)$ assuming ideal gas behaviour.

	Li	Li_2	Mg	Ca
A	10.34540	18.37849	16.79743	53.65151
B	8345.574	11139.62	7844.230	12826.75
C	-.0000884	.0001634	.0002548	.0020016
D	-0.681060	-3.032090	-2.727980	-14.48467

Temp($^\circ$C)	Li	Li_2	Mg	Ca
650	1.67E15	3.10E13	2.92E16	4.72E14
700	4.42E15	1.06E14	6.76E16	1.36E15
750	1.06E16	3.21E14	1.43E17	3.47E15
800	2.31E16	8.68E14	2.81E17	8.01E15
850	4.71E16	2.13E15	5.16E17	1.70E16
870	6.13E16	2.99E15	6.47E17	2.24E16
875	6.55E16	3.24E15	6.84E17	2.40E16
880	6.98E16	3.51E15	7.23E17	2.57E16
885	7.44E16	3.81E15	7.63E17	2.74E16
890	7.92E16	4.13E15	8.06E17	2.93E16
895	8.44E16	4.46E15	8.50E17	3.13E16
900	8.97E16	4.83E15	8.96E17	3.34E16
905	9.54E16	5.22E15	9.44E17	3.56E16
910	1.01E17	5.63E15	9.94E17	3.79E16
915	1.08E17	6.08E15	1.05E18	4.03E16
920	1.14E17	6.55E15	1.10E18	4.29E16

Appendix C - Determination of Mg_2 Density in a Pure Mg Gas

The pressure for a nonideal gas can be expanded in a power series in the number density:

$$P = nkT[1 + nB(T) + n^2C(T) + \ldots \ldots]$$

where $B(T)$ and $C(T)$ are the second and third virial coefficients.[61] The terms in the power series represent the contribution to the pressure of the monomers, dimers, trimers, etc. The term of interest for Mg_2 is $n^2kTB(T)$. $B(T)$ can be calculated from the expression:

$$B(T) = 2\pi\int_0^\infty R^2 dR(1-e^{-U(R)/kT})$$

where R is the internuclear separation and $U(R)$ is the potential energy curve for the ground state.[62] For Mg_2 the $U(r)$ can be approximated by the square well shown below:[67]

$$U(r) = \infty \text{ for } r < r_o, \quad r_o = 3\mathring{A}$$
$$= -\varepsilon \text{ for } r_o < r < \alpha r_o, \quad -\varepsilon = 300/cm$$
$$= 0 \text{ for } r < \alpha r_o; \quad \alpha r_o = 6\mathring{A}$$

then

$$B(T) = 2\pi\int_{ro}^{\alpha r_o} R^2 dR(1-e^{\varepsilon/kT}) + 2\pi r_o^3/3$$
$$= (2\pi r_o^3/3)[1 - (\alpha^3 - 1)(e^{\varepsilon/kT} - 1)]$$

for a temperature of 900°C then $B(T) = 1.8 \times 10^{-22} cm^3$ and using the value for $N(Mg)$ at 900°C then $N(Mg_2) = 1.5 \times 10^{14}/cm^3$ or $Mg_2/Mg = 1.6 \times 10^{-4}$. By analogy, $B(T)$ for LiMg is a square well 100/cm deep and width 2A-6A, $B(T) = 6.9 \times 10^{-23} cm^3$ and $N(LiMg) = 5.6 \times 10^{12}/cm^3$ the ratio LiMg/Mg is 6×10^{-6}.

Appendix D - Mg_2 and LiMg Density Determination in a Li/Mg Gas Mixture

A chemical reaction can be analyzed by means of the Gibbs-Duhem relationship to determine one of the product densities given that the reactant densities and other product densities are known.[63] The Gibbs-Duhem relationships for the reactions:

$$Li_2 + Mg \underset{\leftarrow}{\overset{\rightarrow}{}} LiMg + Li$$
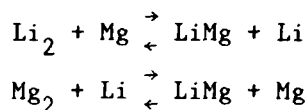
$$Mg_2 + Li \underset{\leftarrow}{\overset{\rightarrow}{}} LiMg + Mg$$

are

$$\frac{\exp[-BE(LiMg)/kT][m(Li_2)m(Mg)]^{1.5} \, B(LiMg) \, Q_v(Li_2) \, [LiMg][Li]}{\exp[-BE(Li_2)/kT][m(LiMg)m(Li)]^{1.5} \, B(Li_2) \, Q_v(LiMg) \, [Li_2][Mg]} = 1$$

and

$$\frac{\exp[-BE(LiMg)/kT][m(Mg_2) \, m(Li)]^{1.5} \, B(LiMg) \, Q_v(Mg_2) \, [LiMg] \, [Mg]}{\exp[-BE(Mg_2)/kT][m(LiMg) \, m(Mg)]^{1.5} \, B(Mg_2) \, Q_v(LiMg) \, [Mg_2] \, [Li]} = 1$$

where m( ) are the masses, B( ) are the diatomic rotational constants, BE( ) are the bond energies in 1/cm, and Q_v( ) are the vibrational partition functions[64] for the respective diatomic: $Q_v = \Sigma \exp(-\omega_e(v+\tfrac{1}{2})/kT)$. The vibrational partition functions depend on the vibrational spacing ω_e and the temperature (T) summed over the vibrational levels v. The values used to solve these equations are shown in the table below:[65,66,67]

	Li	Mg	Li_2	LiMg	Mg_2
m	7	24.3	14	31.3	48.6
ω_e			351.3	65.7	51.1
B_e			.67	.20	.09
Q_v			2.8	2.7	6.26
B.E.			8900	135	400

117

Then $[LiMg] = 3.9 \times 10^{-6}[Li_2][Mg]/[Li]$, $[Mg_2] = 5.9[LiMg][Mg]/[Li]$

and at 900°C using the data from Appendix B the results are shown
below:

$$[LiMg] = 1.9 \times 10^{11}/cm^3; \qquad [LiMg]/[Mg] = 2 \times 10^{-7}.$$

$$[Mg_2] = 1.1 \times 10^{13}/cm^3; \qquad [Mg_2]/[Mg] = 1.2 \times 10^{-5}.$$

Appendix E - Summary of Radiative Lifetime Data and Calculations

I. $Li_2(B)$ State Lifetime Estimate

There are no literature values for the $Li_2(B)$ state lifetime. Therefore the lifetime will be inferred from the relative lifetimes of the Na A and B states reported in the literature[68-72] as shown below:

Dimer State	Li_2	Na_2	K_2
$A^1\Sigma$	18.0ns±2	12.2ns±.3	------
$B^1\Pi$	(10ns)*	7.0ns±.4	11ns

*Inferred from $Na_2(B)/Na_2(A)$ lifetime ratio.

The $Li_2(B)$ lifetime estimate reflects the total decay rate of this state which radiates to both the $A^1\Sigma$ and $X^1\Sigma$ states. Since both the B-A and A-X transitions are states having approximately the same shape to their potential energy curves and the same R_e it is assumed that the Franck Condon envelopes are approximately the same.[65] The relative rate into each state is therefore proportional to the transition frequencies cubed. Therefore the $Li_2(B-X)$ radiative rate will be assumed to be 10^8/s and the $Li_2(B-A)$ rate will be assumed to be 10^7/s.

An additional estimate of the $Li_2(B)$ lifetime was obtained by comparing the area under the absorption curves from Figure 12. By comparing the B-X and A-X absorbed areas a ratio of the (B-X) to (A-X) A coefficients was obtained. Using the literature value for the $Li_2(A-X)$ A coefficient a value of 12nsec ± 4nsec was obtained for the $Li_2(B-X)$ radiative decay rate. The large uncertainty in this estimate is due to the difficulty of separating Li atom absorption from the overlapping dimer absorptions.

II. Summary of LiMg($A^2\Pi$) State Lifetime Calculations

Estimates of the bound free and bound bound transition probabilities were calculated by Michels using the potential energy curves shown in Figure 4 and dipole moment functions from Figure 6. Since the dipole moment function is changing rapidly with internuclear separation, the A coefficient also changes with vibrational level. The majority of the observed emission emanates from the $v' = 3,4,5$ of the A state. The average A coefficient for these three levels is $.13 \times 10^7$/s.

Bound-Free		Bound-Bound		
v'	A(1/s)	v'	v''	A(1/s)
0	$.6 \times 10^6$	0	0,2	.2, 1
1	$.7 \times 10^6$	1	0,2	3, 10
2	$.9 \times 10^6$	2	0,2	30, 100
3	$.11 \times 10^7$	3	0,2	200, 500
4	$.13 \times 10^7$	4	0,2	700, 2000
5	$.15 \times 10^7$	5	0,2	3000, 7000
6	$.17 \times 10^7$	6	0,2	10000, 30000

*Private Communication, H. Michels.

120

Appendix F - Phase Shift Derivations

I. $Li_2(B)$ - $Li(^2P)$ Phase Shift Derivation (No Mg)

The phase shift of $Li(^2P)$ relative to $Li_2(B)$ was determined using the rate equation for $Li(^2P)$ shown below from Figure 27:

$$d[Li^*]/dt = [Li_2(B)][Li]K_2 - [Li^*](A_1 + [Li_2(X)]K_3 + [Ar]K_9)$$

Then upon Fourier analyzing, keeping only terms of frequency ω, ignoring the negligibly small cross terms, cancelling the $e^{i\omega t}$, and algebraically rearranging:

$$[Li^*]_1 \exp(i\phi Li_2(B) - i\phi Li^*) = [Li_2(B)]_0[Li]_0 K_2 /$$
$$(i\omega + (A_1 + [Li_2(X)]_0 K_3 + [Ar]_0 K_9))$$

By defining

$$A_{K1} \equiv A_1 + [Li_2(X)]_0 K_3 + [Ar]_0 K_9$$

$$\phi_1 \equiv \phi(Li_2(B)) - \phi(Li(^2P))$$

$$\Delta \equiv [Li]_0 K_2 / (\omega^2 + A_{K1}^2)$$

And then substituting into the equation above:

$$[Li^*]_1 \exp(i\phi_1) = \Delta[Li_2(B)]_1(i\omega + A_{K1})$$

Then

$$Re([Li^*]) = \Delta[Li_2(B)]_1 A_{K1}$$

$$Im([Li^*]) = \Delta\omega[Li_2(B)]_1$$

Since by the Euler identity:

$$[Li*]_1 \exp(i\phi_1) = Re([Li*]) + iIm([Li*])$$

Thus:

$$\omega/\tan \phi_1 = A_{K1}$$

II. $Li_2(B)$ - $Li_2(A)$ Phase Shift (No Mg)

The phase of $Li_2(A)$ relative to $Li_2(B)$ was determined using
the rate equation for $Li_2(A)$ as shown below from Figure 27. Since
the formation of $Li_2(A)$ depends on both the direct process of radiation
from the B state and a second order process where Li^* is formed as
an intermediate the kinetics become quite complex.

$$d[Li_2(A)]/dt = [Li^*][Li_2(X)]K_3 + [Li_2(B)]A_4 - [Li_2(A)](A_3 + K_7[Ar]_0)$$

By Fourier analyzing, keeping only the terms at frequency ω,
ignoring the negligibly small terms and cancelling the $\exp(i\omega t)$
and algebraically rearranging:

$$[Li_2(A)]_1 \exp(i\phi(Li_2(B)) - i\phi(Li_2(A))) = ([Li^*]_1 \exp(i\phi(Li^*) - i\phi(Li_2(B)))$$
$$[Li_2(X)]_0 K_3 + [Li_2(B)]_1 A_4)/(i\omega + A_3 + K_7[Ar]_0)$$

Note that two different phase shifts remain in this equation; the
phase of Li^* relative to $Li_2(B)$ and the phase of $Li_2(A)$ relative to
$Li_2(B)$. By making the following substitutions:

$$A_{K3} \equiv A_3 + K_7[Ar]_0 \; ; \; \phi(Li_2(B) - Li_2(A)) \equiv \phi_3$$
$$\phi_1 \equiv \phi(Li^*) - \phi(Li_2(B))$$
$$\phi_3 \equiv \phi(Li_2(B) - \phi(Li_2(A))$$

And rationalizing the denominator:

$$[Li_2(A)]_1 \exp(i\phi_3) = ([Li^*]_1 \exp(i\phi_1) [Li_2(X)]_0 K_3 + [Li_2(B)]_1 A_4)(i\omega + A_{K3})/$$
$$(\omega^2 + A_{K3}^2)$$

The real and imaginary parts of this expression are:

$$Re([Li_2(A)]_1 \exp(i\phi_3)) =$$
$$([Li_2(B)]A_4 + Re([Li^*]_1 \exp(i\phi_1))[Li_2(X)]_0 K_3)A_{K3} + \omega Im([Li^*]_1 \exp(i\phi_1))/$$
$$(\omega^2 + A_{K3}^2)$$

$$Im([Li_2(A)]_1 \exp(i\phi_3) = (\omega([Li_2(B)]A_4 + Re([Li^*]_1 \exp\phi_1)[Li_2(X)]_0 K_3)$$
$$+ [Li_2(X)]_0 K_3 A_{K3} Im([Li^*]_1 \exp(i\phi_1))/(\omega^2 + A_{K3}^2)$$

Note that the above expressions include the real and imaginary
expressions for Li* which can be obtained from the previous section.
Making these substitutions and applying the Euler identity results
in the following expression for ϕ_3.

$$\tan\phi_3 = \omega(A_4 + (A_{K1} + A_{K3})\Delta)/(A_{K3}A_4 + (_{K3}A_{K1} + \omega^2)\Delta)$$

To evaluate the equation above for K_2 using the measured values of
$\omega/\tan\phi$ requires the values for A_{K3}, A_4, A_{K1}, and $[Li_2(X)]_0 K_3$. A_{K3} is
assumed to be just A_3 since a typical Ar quenching rate of 10^{-15}
makes the quenching term in A_{K3} negligible. $A_3 = 5.6 \times 10^7/s$
from Appendix E, A_4 is calculated to be $10^7/s$(see Appendix E), the
value of A_{K1} is taken from the phase shift data, Table 19. The
numerical values for the different variables in the equation are
tabulated below along with the data for $\omega/\tan\phi$ for two different
temperatures:

$T(°C)$	$\omega^2 + A_{K1}^2$	$[Li_2(X)]K_3$	A_{K1}	Δ	$\omega/\tan\phi$
850	4.1×10^{12}	1.4×10^6	1.8×10^6	3.4×10^{-7}	$3.1 \pm .9 \times 10^6$
895	1.2×10^{13}	2.9×10^6	3.4×10^6	2.4×10^{-7}	$6.8 \pm .3 \times 10^6$

By using the appropriate values for $[Li]_0$ from Appendix B, K_2 is $4.2 \pm 1.5 \times 10^{-10} cm^3/s$ and $1.2 \pm .3 \times 10^{-10} cm^3/s$ at 850°C and 895°C respectively, the average being $2.7 \times 10^{-10} cm^3/s$. Variations in temperature do not account for the discrepancy between the two rate constants.

III. LiMg - Li_2(B) Phase Shift Analysis

The phase of LiMg relative to Li_2(B) was determined from the rate equation for LiMg as shown below from Figure 27:

$$d[LiMg(A)]/dt = -[LiMg(A)]([Li]K_4 + A_5 + [Ar](K_8 + K_5) + [Li_2(B)][Mg]K_1$$

Fourier analyzing , keeping terms only at the fundamental frequency, cancelling negligible terms and the $\exp(i\omega t)$, and algebraically rearranging yields:

$$(i\omega + [Li]_0 K_4 + A_5 + [Ar](K_8 + K_5)) [LiMg(A)]\exp(i\phi_5) = [Li_2(B)]_1[Mg]_0 K_1$$

Defining
$$\phi_5 \equiv \phi(Li_2(B) - LiMg(A))$$
$$A_{K5} \equiv [Li]K_4 + A_5 + [Ar](K_8 + K_5)$$

Substituting into the equation above and applying the Euler identity:

$$\omega/\tan\phi_5 = A_{K5}$$

125

Appendix G - $Li_2(B)$ Intensity vs Temperature

Using the steady state solution to the rate equation for $Li_2(B)$ from Figure 26, an expression can be developed for the temperature dependence of $Li_2(B)$ emission intensity. Taking the ratio of the steady state $Li_2(B)$ rate equation for no Mg present at two temperatures T_i and T_f yields:

$$[Li_2(B)]_i/[Li_2(B)]_f = ((A_2 + A_4 + K_2[Li]_f + [Q]K_9)/[Li_2(X)]_f)/$$
$$((A_2 + A_4 + K_2[Li]_i + [Q]K_9)/[Li_2(X)]_i)$$

If the initial temperature is chosen such that $K_2[Li]_0 \cong A_2 + A_4$ and since K_9 is $<< 10^{-11} cm^3/s$ then for 100 torr of Ar, $A_2 + A_4 >> [Ar]K_9$ thus K_9 can be ignored. Using this approximation simplifies the equation above to:

$$\gamma = [Li_2(B)]_0 [Li_2(X)]_i/[Li(B)]_i [Li_2(X)]_0 = 1 + K_2[Li]_i/A_2 + A_4$$

The values of $[Li_2(X)]_f/[Li_2(X)]_i$ were calculated from Appendix B and data points from $844^{\circ}C$ to $893.5^{\circ}C$ from Fig 32 were used with the equations shown above to determine K_2 as shown below:

126

T° (C)	γ	$K_2 (cm^3/s)$
844	1.15	4.4×10^{-10}
849	1.13	3.3×10^{-10}
856.5	1.17	4.1×10^{-10}
864	1.16	3.4×10^{-10}
874	1.23	4.0×10^{-10}
883.5	1.28	4.2×10^{-10}
893.5	1.40	5.3×10^{-10}

The value of K_2 determined from this data is $4.3 \pm 1.5 \times 10^{-10} cm^3/s$.

Appendix H - Ar Quenching of LiMg(A)

Using the data from Figure 18 in Chapter 2 an upper bound can be obtained for the sum of the rates of deactivation and dissociation of LiMg(A) by $Ar(K_8 + K_5)$. It is an upper bound since the $Li_2(B)$ was assumed to be immune to Ar quenching. The data is summarized below:

Total Pressure	Ar Pressure	Ar Density	I	I/I_o	$K_8 + K_5$
425	316	2.6×10^{18}	132	1.44	1.7×10^{-12}
344	235	1.9	152	1.26	1.4
280	171	1.4	158	1.2	1.4
204	95	7.8×10^{17}	170	1.12	1.5
162	53	4.4	185	1.03	.7
122	13	1.1	191	1	

The rate constant is determined by taking the ratio of the LiMg rate equation from Figure 28 with and without Ar present:

$$[LiMg(A)]_A/[LiMg(A)]_{NA} = (A_5 + [Li]K_4)/(A_5 + [Li]K_4 + [AR](K_8 + K_5)$$

By substituting $A_5 + [Li]K_4 = 10^7/s$ from the LiMg phase shift data from Table 21 and I/I_0 as the ratio of the LiMg intensity with the specified amount of Ar to the LiMg intensity with 13 torr of Ar (Ar effects assumed negligible) then:

$$10^7((I/I_0) - 1)/[Ar] = K_8 + K_5$$

The resulting average for the upper bound on $K_8 + K_5$ is 1.3×10^{-12}.

128

Appendix I - [Li*] to [Li$_2$(B)] Relationship

An expression was developed for the concentration of Li* in terms of Li$_2$(B) using the rate constants determined in section 2 of Chapter 3. The governing steady state equation from Figure 28 is shown below:

$$[Li^*] = [Li_2(B)][Li]K_2/([Li_2(X)]K_3 + A_1 + [Ar]K_9)$$

The results of Chapter 3 section 2.a showed that the terms $A_1 + [Ar]K_9$ in the denominator of the right hand side of the equations are negligible when compared to $[Li_2(X)]K_3$. Then for 890°C [Li] = 7.9 x 10^{16}/cm^3 and $[Li_2(X)]$ = 4.1 x 10^{15} from Appendix B, and K_2 = 3.5 x 10^{-10}cm^3/s and K_3 = 6.5 x 10^{-10}cm^3/s from Table 19, yields:

$$[Li^*] = 10.4 \ [Li_2(B)]$$

Vita

David Kurt Neumann was born on 21 September 1952 in Waukesha, Wisconsin. He graduated from high school in East Troy, Wisconsin, in 1970 and then attended the United States Air Force Academy, where he received a Bachelor of Science in Physics and a regular commission in the USAF in 1974. In August 1974 he reported to the Space and Missile Systems Organization at Los Angeles Air Force Station as a project engineer on the Advanced Space Defense Program. During the time he was stationed in Los Angeles he attended the University of Southern California, receiving a Master of Science in Electrical Engineering in 1976. In August 1977 he entered the Air Force Institute of Technology. After completing his course work in December 1978, he was assigned to the Air Force Weapons Laboratory, Kirtland AFB, New Mexico, to complete his PhD research.
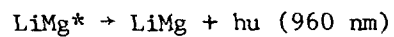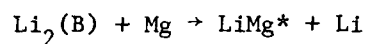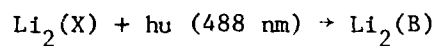
Permanent Address: P.O. Box 596

Palmer Lake, CO 80133

REPORT DOCUMENTATION PAGE		READ INSTRUCTIONS BEFORE COMPLETING FORM
1. REPORT NUMBER AFIT/DS/PH/80-3	2. GOVT ACCESSION NO.	3. RECIPIENT'S CATALOG NUMBER
4. TITLE *(and Subtitle)* Observation and Analysis of LiCa and LiMg Excimers		5. TYPE OF REPORT & PERIOD COVERED PhD Dissertation
		6. PERFORMING ORG. REPORT NUMBER
7. AUTHOR(s) DAVID K. NEUMANN Capt, USAF		8. CONTRACT OR GRANT NUMBER(s)
9. PERFORMING ORGANIZATION NAME AND ADDRESS Air Force Institute of Technology Wright Patterson AFB, Ohio 45433		10. PROGRAM ELEMENT, PROJECT, TASK AREA & WORK UNIT NUMBERS Project 33260389
11. CONTROLLING OFFICE NAME AND ADDRESS Air Force Weapons Laboratory (AFWL/ARAP) Kirtland AFB, NM 87117		12. REPORT DATE August, 1980
		13. NUMBER OF PAGES 142
14. MONITORING AGENCY NAME & ADDRESS(*if different from Controlling Office*)		15. SECURITY CLASS. *(of this report)* UNCLASSIFIED
		15a. DECLASSIFICATION DOWNGRADING SCHEDULE

16. DISTRIBUTION STATEMENT *(of this Report)*

Approved for public release; distribution unlimited.

17. DISTRIBUTION STATEMENT *(of the abstract entered in Block 20, if different from Report)*

~~~~~~~~~~~~~~~~~ AFR 190-17.   ~~~~~~~~ of Technology (ATC)
~~~~~~~~~~~~~~   ~~~~~~~~ AFB, OH 45433

18. SUPPLEMENTARY NOTES

28 JAN 1982

FREDRIC C. LYNCH, Major, USAF
Director of Public Affairs

19. KEY WORDS *(Continue on reverse side if necessary and identify by block number)*

EXCIMER   MAGNESIUM
MOLECULAR SPECTROSCOPY   CALCIUM
LITHIUM

20. ABSTRACT *(Continue on reverse side if necessary and identify by block number)*

Emission from LiCa and LiMg excimers was obtained for the first time upon pumping mixures of Li and Ca vapors and Li and Mg vapors with an Ar^+ laser. The emission spectra were analyzed spectroscopically and found to be in good agreement with a synthetic spectrum derived from ab initio calculations of the LiMg and LiCa potential energy curves. A kinetic model was developed to explain the LiMg formation process. The kinetics of production of LiMg* were analyzed by time delay measurements and efficiency measurements of the fluorescence

DD FORM 1473
1 JAN 73

Block 20

intensity.   The LiMg* emission results from the following reactions:

$$Li_2(X) + hu \ (488 \ nm) \rightarrow Li_2(B)$$

$$Li_2(B) + Mg \rightarrow LiMg* + Li$$

$$LiMg* \rightarrow LiMg + hu \ (960 \ nm)$$

The LiMg formation rate by the above reaction was determined to be 2.9 x $10^{-10} \ cm^3/sec$.   Several other rate constants were measured for the Li/Mg system which resulted in an overall specification of the kinetic model.

3-8